GCA TECHNICAL REPORT NO. 66-16-N

INVESTIGATION OF THE D AND E REGION DURING THE IQSY

L. G. SMITH P. J. McKINNON L. H. WEEKS

GCA CORPORATION
Bedford, Massachusetts

FINAL REPORT

CONTRACT NO. NASw-1141

PREPARED FOR
NATIONAL AERONAUTICS AND SPACE ADMINISTRATION
HEADQUARTERS
WASHINGTON, D. C.

MAY 1966

GCA Technical Report No. 66-16-N

INVESTIGATION OF THE D AND E REGION DURING THE IQSY

L.G. Smith
P.J. McKinnon
L.H. Weeks

FINAL REPORT

Contract No. NASw-1141

May 1966

GCA CORPORATION
GCA TECHNOLOGY DIVISION
Bedford, Massachusetts

Prepared for
NATIONAL AERONAUTICS AND SPACE ADMINISTRATION
Headquarters
Washington, D. C.

TABLE OF CONTENTS

LIST OF ILLUSTRATIONS

LIST OF ILLUSTRATIONS (Continued)

LIST OF ILLUSTRATIONS (Continued)

LIST OF ILLUSTRATIONS (Concluded)

INVESTIGATION OF THE D AND E REGION DURING THE IQSY

by

L. G. Smith
P. J. McKinnon
L. H. Weeks
GCA Corporation, GCA Technology Division
Bedford, Massachusetts

SUMMARY

This report describes an investigation of the ionosphere up to about 180 km during the second year of the International Quiet Sun Year (1964 to 1965). One series of rockets was launched on the NASA Mobile Launch Expedition in the South Pacific in a study of the latitude variation of the ionosphere. The other series of flights was made from Wallops Island in study of the seasonal variation. The last flight of this series was used to investigate the phenomenon of anomalous winter absorption.

Author

INTRODUCTION

This report describes a program of rocket measurements for the investigation of the lower ionosphere during solar minimum. It is a continuation of an earlier program of rocket measurements [1,2]* which was part of the international IQSY effort. General objectives of both programs included the evaluation of techniques for measuring electron density in the lower ionosphere and for measurements on specified days which would augment the overall synoptic IQSY effort. In addition, the present program of measurements had the following specific scientific objectives.

A series of five rockets, Nike Apaches 14.228 to 14.232, were launched from the NASA Mobile Launch Facility, USNS Croatan, in the South Pacific for the purpose of studying latitudinal variations in the ionosphere and for comparisons with northern hemisphere data. Nike Apache 14.245 was launched from Wallops Island in June at a solar zenith angle of 95 degrees. In addition to the primary experiments, an attempt was made to detect the electron temperature fluctuations resulting from heating the ionosphere by radio signals transmitted from a powerful AM broadcast station. Two later flights, Nike Apaches 14.247 and 14.248, were fired at 60 degrees zenith angle in winter. The purpose of these flights was to investigate the anomalous absorption that is occasionally observed at mid-latitudes in winter.

*Numbers in [ ] represent references.

The payload instrumentation is generally the same as in the previous program with some improvements. The GCA experiments included a nose probe for measuring electron density and electron temperature and uv photometers for measuring molecular oxygen. The University of Illinois participation included differential absorption and Faraday rotation experiments to obtain electron density and electron collision frequency. For one payload, Professor J. Sayers of the University of Birmingham (England) supplied an rf (capacity) probe and Professor A. Nagy of the University of Michigan supplied an ion trap.

Two papers based on some earlier rocket flights of this progam and results of the previous program were presented at the Second Conference on Direct Aeronomic Measurements in the Lower Ionosphere, held at the University of Illinois, 27 to 30 September 1965. L.G. Smith presented a paper on "Electron and Ion Densities above 100 km," and L.H. Weeks reviewed" Atmospheric Density Measurements by Absorption Spectroscopy." Both papers will be included in the published proceedings of the conference. A paper presented at the COSPAR Meeting in Vienna, 1966, by L.G. Smith appears as Appendix A in this report.

VEHICLE AND INSTRUMENTATION PERFORMANCE

Flight Performance Data

The performance of all ten vehicles used in this program was very good. A failure in the telemetry system of one flight and a partial failure in another resulted in some loss of data. Results of the vehicle and instrumentation performance are given in this and in the following sections of this report. Complete details of installation procedures and modification of the payloads have been placed in Appendix B.

Five vehicles were launched during March and April 1965 from the USNS Croatan during the NASA Mobile Launch expedition and five were launched at intervals between June 1965 and January 1966 from Wallops Island, Virginia. The dates and times of launch are given in Table I, which is based on telemetered data. The times of stage ignition and burnout and of impact are also given.

Excellent trajectory data for the flights launched from Wallops Island was obtained by radar skin-track. For the launches from the USNS Croatan a partial trajectory by radar skin-track is available for the first vehicle (Nike Apache 14.228) but no radar data were obtained on the remaining four vehicles of the series. Using the time-of-flight method based on baroswitches incorporated in the payloads it has been possible to obtain trajectories for all except Nike Apache 14.229 which experienced a failure of the telemetry system.

The method of computing the trajectory from the times of baroswitch actuation on ascent and descent has been described. [3] Experience with similar payloads at Wallops Island, when a comparison can be made with the trajectory obtained from radar, shows that apogee altitude can be obtained to within 1 km and apogee time to within 1 second. Apogee time and altitude as obtained from the time above the 23 km (75,000 ft) and 15.0 km (50,000 ft) reference levels are given in Tables IIa and IIb. Radar data for Nike Apaches 14.244/7 are given in Table IIc for comparison. Apogee altitudes as obtained from radar data for Nike Apaches 14.244/7 are plotted against time-of-flight above the reference altitudes in Figure 1. The line is the theoretical relation using a constant value of acceleration due to gravity of 935 cm/sec^2, as determined from earlier flights. The observed points for the 23.0 km reference level are within 1 km of apogee of the empirical relation with the exception of Nike Apache 14.245 (+1.8 km). Three of the four observed points for the 15 km reference level give errors ranging from +1.4 km to 1.6 km. The fourth point also gives a positive error (+0.2 km). A line based on 928 cm/sec^2 would provide a more accurate fit of the data points for 15 km reference level. This lower value of"effective" g is not unusual since the vehicle is under powered flight (Apache) for up to 4 seconds after actuation of the baroswitch on ascent.

The times of apogee, which are normally obtained to within 1 second, are refined to reduce the error to about 0.1 second by a comparison of the prominent features of the ascent and descent profiles of probe current and from the

Table I. Rocket Launch Data (Telemetry Records)

Nike Apache 14.228 (20 March 1965, USNS Croatan, 12°55'S, 78°00'W

Nike Ignition:	1320:09.07 UT	(T)
Nike Burnout:	1320:12.66 UT	(T + 3.59 sec.)
Apache Ignition:	1320:30.15 UT	(T + 21.08 sec.)
Impact (Loss of Signal):	1326:59.21	(T + 410.14 sec.)

Nike Apache 14.229 (23 March 1965, USNS Croatan, 12°58'S, 77°58'W)

Nike Ignition:	0931:09.09 UT	(T)
Nike Burnout:	0931:12.61 UT	(T + 3.52 sec.)
Apache Ignition:	NO DATA	
Impact (Loss of Signal):	NO DATA	

Nike Apache 14.230 (5 April 1965, USNS Croatan, 29°34'S, 75°13'W)

Nike Ignition:	1345:53.08 UT	(T)
Nike Burnout:	1345:56.53 UT	(T + 3.45 sec.)
Apache Ignition:	1346:14.77 UT	(T + 21.69 sec.)
Impact (Loss of Signal):	1352:45.33 UT	(T + 412.25 sec.)

Nike Apache 14.231 (9 April 1965, USNS Croatan, 44°15'S, 77°40'W)

Nike Ignition:	1918:15.08 UT	(T)
Nike Burnout:	1918:18.6 UT	(T + 3.52 sec.)
Apache Ignition:	1918:36.69 UT	(T + 21.61 sec.)
Impact (Loss of Signal):	1925:26.39 UT	(T + 431.31 sec.)

Nike Apache 14.232 (12 April 1965, USNS Croatan, 58°19'S, 78°00'W)

Nike Ignition:	1714:02.1 UT	(T)
Nike Burnout:	1714:05.69 UT	(T + 3.59 sec.)
Apache Ignition:	1714:24.6 UT	(T + 22.5 sec.)
Impact (Loss of Signal):	1721:07.53 UT	(T + 425.43 sec.)

Table I. (Concluded)

Nike Apache 14.244 (15 September 1965, Wallops Island, Virginia)

Nike Ignition:	2028:00.1 UT	(T)
Nike Burnout:	2028:03.64 UT	(T + 3.54 sec.)
Apache Ignition:	2028:21.63 UT	(T + 21.53 sec)
Impact (Loss of Signal):	2035:02.18 UT	(T + 422.08 sec.)

Nike Apache 14.245 (14 June 1965, Wallops Island, Virginia)

Nike Ignition:	0913:30.17 UT	(T)
Nike Burnout:	0913:33.79 UT	(T + 3.62 sec.)
Apache Ignition:	0913:52.6 UT	(T + 22.43 sec.)
Impact (Loss of Signal):	0920:21.48 UT	(T + 411.31 sec.)

Nike Apache 14.246 (17 June 1965, Wallops Island, Virginia)

Nike Ignition:	2141:00.16 UT	(T)
Nike Burnout:	2141:03.73 UT	(T + 3.57 sec.)
Apache Ignition:	2141:20.76 UT	(T + 20.6 sec.)
Impact (Loss of Signal):	2147:50.72 UT	(T + 410.56 sec.)

Nike Apache 14.247 (15 December 1965, Wallops Island, Virginia)

Nike Ignition:	1700:00.1 UT	(T)
Nike Burnout:	1700:03.63 UT	(T + 3.53 sec.)
Apache Ignition:	1700:24.18 UT	(T + 24.08 sec.)
Impact (Loss of Signal):	1707:02.86 UT	(T + 422.76 sec.)

Nike Apache 14.248 (10 January 1966, Wallops Island, Virginia)

Nike Ignition:	1714:00.1 UT	(T)
Nike Burnout:	1714:03.38 UT	(T + 3.28 sec.)
Apache Ignition:	1714:20.06 UT	(T + 19.96 sec.)
Impact (Loss of Signal):	1721:06.1 UT	(T + 426 sec.)

Table IIa. Apogee Altitude and Time Obtained from Time Above Reference Level (23.0 km)

Nike Apache	Apogee (km)	Universal Time	Time from Launch (sec)
14.228	174.0	1323:33.3	208.3
14.229	No Data Due to Loss of Telemetry		
14.230	177.5	1349:24.3	211.3
14.231	190.7	1921:53.4	218.4
14.232	Baroswitch failed to close near reference altitude		
14.244	180.6	2031:32.9	212.8
14.245	176.8	0917:01.6	211.4
14.246	175.6	2144:30.9	210.7
14.247	183.7	1703:37.4	217.3
14.248	No data due to partial loss of telemetry		

Table IIb. Apogee Altitude and Time Obtained from Time Above Reference Level (15.0 km)

Nike Apache	Apogee (km)	Universal Time	Time from Launch (sec)
14.228	173.9	1323:38.0	209.0
14.229	No Data Due to Loss of Telemetry		
14.230	176.9	1349:23.7	210.7
14.231	190.9	1921:53.8	218.8
14.232	186.9	1717:39.8	217.8
14.244	181.8	2031:34.0	213.9
14.245	176.4	0917:01.7	211.5
14.246	176.9	2144:30.9	210.7
14.247	184.5	1703:37.7	217.6
14.248	No Data Due to Partial Loss of Telemetry		

Table IIc. Apogee Altitude and Time (Radar Data)

Nike Apache	Apogee (km)	Universal Time	Time from Launch (sec)
14.228	NO DATA		
14.229	NO DATA		
14.230	NO DATA		
14.231	NO DATA		
14.232	NO DATA		
14.244	180.3	2031:34.1	214.0
14.245	175.0	0917:02.7	212.5
14.246	176.2	2144:30.5	210.4
14.247	182.9	1703:37.9	217.8
14.248*	186.2	1717:37.1	217.0

*Data obtained from radar plotboard.

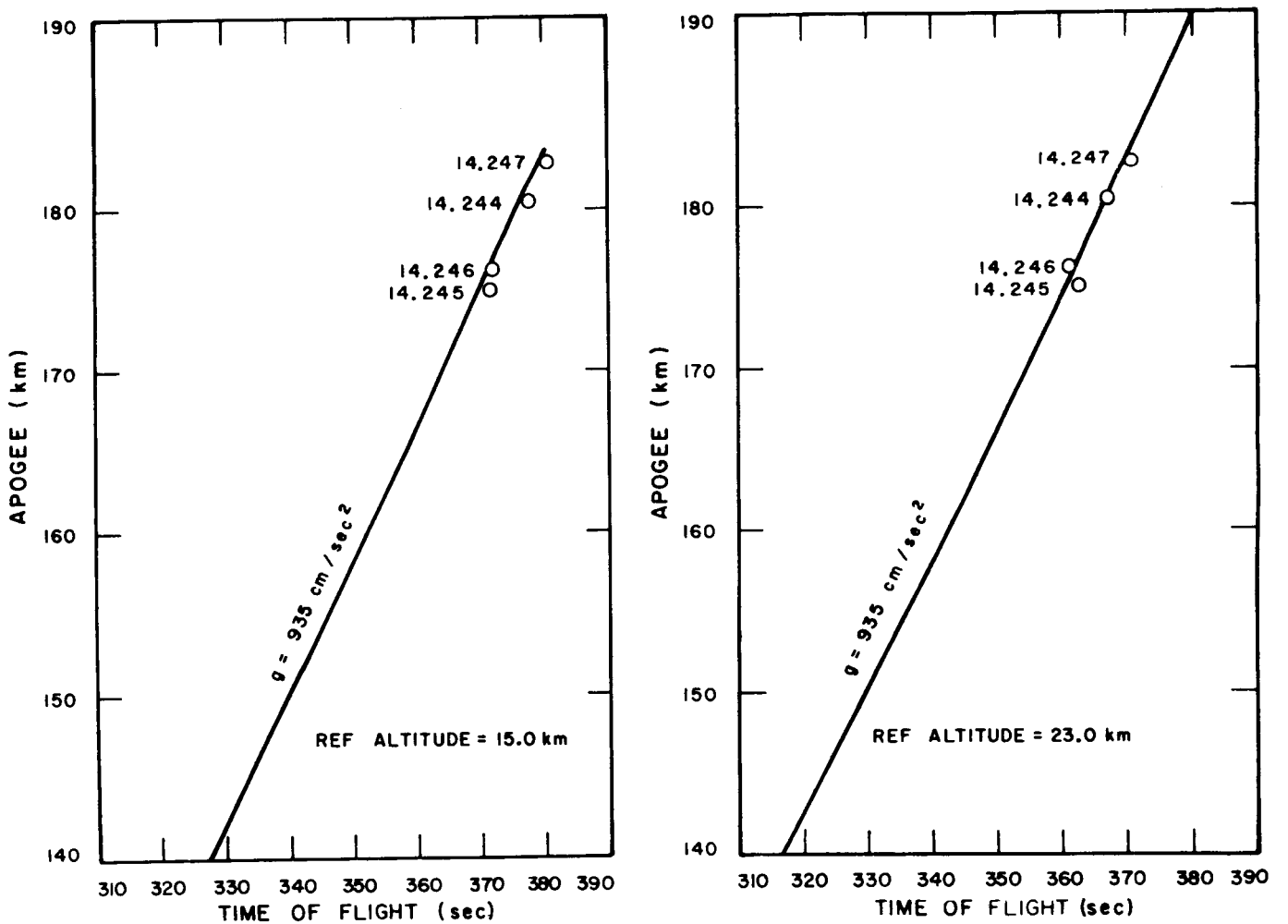

Figure 1. Apogee altitude (radar data) vs time-of-flight above reference altitudes 15 km and 23 km.

symmetry of the Lyman-α absorption profile. The values of apogee altitude and revised value of apogee time used in computing the trajectory are given in Table III.

TABLE III

APOGEE ALTITUDE AND TIME

Vehicle	Apogee Altitude	Apogee Time
14.228	173.9 km	1323:38.0 UT
14.230	176.9 km	1349:23.7 UT
14.231	190.9 km	1921:53.8 UT
14.232	186.9 km	1717:39.8 UT

The impact data obtained from radar data is listed in Table IV.

Processional motion and spin rate data at apogee obtained from solar aspect data is given in Table V. The spin rate histories from launch up to T + 40 seconds (magnetic aspect data) are shown in Figure 2. Both data indicate normal vehicle motion for all flights.

The uv detectors are positioned in the payload based on the predicted value of rocket elevation angle. Table VI lists the predicted and actual rocket elevation angle. The actual value is the average value of the precession cone as obtained from the solar aspect data. Interestingly, the difference between actual and predicted is not greater than ± 10 degrees.

Concerning the instrumentation performance of the ten payloads, with respect to the scientific objectives of the program, eight were successful, one a partial failure and one a complete failure. The instrumentation performance for each of the flights is summarized in Table VII.

The telemetry signal for Nike Apache 14.229 dropped abruptly at Nike burnout (T + 3.5 sec) and ceased at approximately T + 56 seconds after launch. No scientific data were obtained from this flight. Nike Apache 14.248 launched at Wallops Island experienced a similar drop in signal strength at Nike burnout (T + 3.3 sec). The received signal dropped about 40 dB followed by complete loss of signal due to free space loss at T + 75 sec. Upon initial inspection of the telemetry records, it appeared that no data could be obtained from the flight. Subsequently the tapes were played back on a more sophisticated data reduction system which included a phase-lock discriminator with narrow band tracking filters. Partial dc probe and uv data were extracted. Unfortunately, this method cannot improve the signal-to-noise ratio of the wide band (500 cps) propagation data sufficiently to render any useful differential absorption or

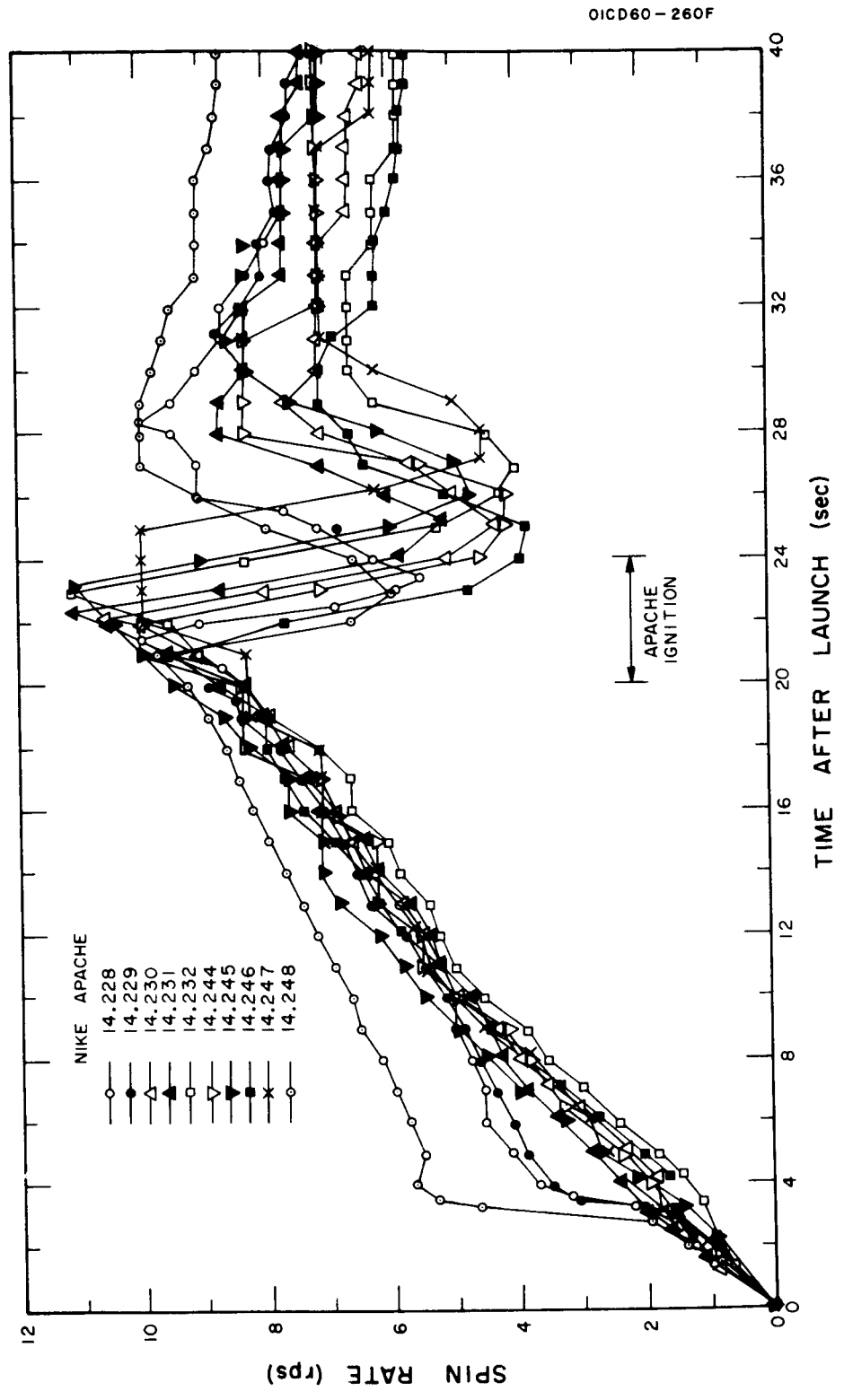

Figure 2. Spin rate histories of Nike Apaches 14.229/32 and 14.244/48.

Table IV. Impact Data (Radar)

Nike Apache	Horizontal Range (km)	Ref. Altitude Above Sea Level (km)	Azimuth (deg.)	Time from Launch (sec)
14.228	NO DATA			
14.229	NO DATA			
14.230	NO DATA			
14.231	NO DATA			
14.232	NO DATA			
14.244	161.2	7.31	96.3	412.0
14.245	135.4	1.40	99.1	415.7
14.246	144.4	1.44	91.9	413.5
14.247	180.4	6.12	91.5	417.8
14.248*	141.3	0	98.9	426.0

*Data obtained from radar plotboard

Table V. Precessional Motion and Rocket Spin (Solar Aspect Data)

Nike Apache	Period (sec)	Cone Angle (deg.)	Spin Rate at Apogee (rps)
14.228	32.0	10.0	6.73
14.229	NO DATA		
14.230*	35.0	15.0	6.06
14.231	29.0	23.5	7.14
14.232	36.0	38.0	5.59
14.244	31.0	14.5	6.60
14.245	31.0	10.0	7.02
14.246	39.0	19.5	5.43
14.247	34.0	14.0	5.99
14.248	NO DATA		

*Magnetic aspect data, doors failed to eject.

Table VI. Rocket Elevation Angle

Nike Apache	Effective Elevation		Difference
	Predicted	Actual*	
14.228	83°	87.2°	+4.2°
14.231	84	82	+2.0
14.232	84	92.1	+8.1
14.244	80	74.4	-5.6
14.245	80	90.2	+10.2
14.246	80	79.9	-0.1
14.247	80	69.7	-10.3

*Average value of precession cone as obtained from solar aspect data

TABLE VII

INSTRUMENTATION PERFORMANCE

Nike Apache 14.228

Telemetry: Good; except for last part of flight. Some interference at the ground station from the adjacent tracking radar.

DC Probe: Good; except for leakage in early part of flight.

UV Detectors: Lyman-α, good although sensitivity low; 1450Å, no data.

Aspect Sensors: Solar and magnetic both good.

Nike Apache 14.229

Telemetry: Poor; signal became weak at T+3.1 seconds and was lost at T+56 seconds. Up to this time instrumentation was working properly. No scientific data obtained.

Nike Apache 14.230

Telemetry: Good, except near end of flight.

DC Probe: Good.

UV Detectors: No data as doors failed to eject. Monitor shows that bellows fired and mechanism actuated.

Aspect Sensors: Magnetic, good; solar, no data (covered by doors).

Nike Apache 14.231

Telemetry: Good; except end of flight.

DC Probe: Good.

UV Detectors: Lyman-α and 1450Å, both good.

Aspect Sensors: Both good.

Nike Apache 14.232

Telemetry: Good.

DC Probe: Good. Initial data lost due to late removal of calibration by baroswitch.

UV Detectors: Lyman-α, good on descent although sensitivity low (late door ejection resulting from baroswitch malfunction); 1450Å, no data.

Aspect Sensors: Both good.

TABLE VII (concluded)

Nike Apache 14.244

Telemetry: Good.

DC Probe: Good.

UV Detectors: Lyman-α and 1450Å, both good.

Aspect Sensors: Both good.

Nike Apache 14.245

Telemetry: Good.

DC Probe: Good.

UV Detectors: Lyman-α and 1300Å, both good.

Aspect Sensors: Both good.

Nike Apache 14.246

Telemetry: Good.

DC Probe: Good.

UV Detectors: Lyman-α and 1300Å, both good.

Aspect Sensors: Both good.

Nike Apache 14.247

Telemetry: Good.

DC Probe: Good.

UV Detectors: Lyman-α good; 1450Å no data (door failed to eject).

Aspect Sensors: Both good.

Nike Apache 14.248

Telemetry: Poor; signal reduced 40 dB at T+3.3 sec (early Nike burnout); lost at T+75 sec.

DC Probe: Good data obtained up to 92.6 km.

UV Detectors: Lyman-α, good up to 71 km; 1450Å, no data (telemetry failure).

Aspect Sensors: Both sensors worked properly but only the narrow-bandwidth data of the magnetic aspect sensor could be extracted because of the low signal-to-noise ratio of the telemetry system.

Faraday rotation data. The success of telemetry receiving station (GSFC Station "A") at Wallops Island in tracking the signal may be attributed to the fact that the look angles (elevation and azimuth) used to direct the antennas was obtained from the tracking radars. Any attempt to use the method by which the antennas are pointed for maximum signal strength would have been totally unsuccessful.

Good data was obtained from the 1450Å ion chamber used with gas gain on Nike Apache 14.244. In the Nike Apache 14.247, the door covering the 1450Å detector did not eject. It is believed that the compression spring which prevents the door release mechanism from opening during the condition of launch environment, recoiled causing the bellows actuator to partially recompress. Under these conditions the mechanism would release only the door covering the Lyman-α ion chamber. The mechanism used in Nike Apache 14.248 was subsequently reworked and both doors were successfully ejected during the flight.

In Nike Apaches 14.244 and 14.247 no effects of voltage breakdown were noted in the uv data, an unusual modulation of the dc probe current was observed from 50 to 75 km where voltage breakdown is most likely to occur. The 600 volt power supply used with the 1450Å ion chamber is believed to be the cause of the trouble.

It is not immediately apparent how breakdown could cause a modulation with the same frequency as the spin rate. However, two characteristics support the assumption that some degree of breakdown did occur: (1) the height range over which the modulation of probe current occurred and (2) the depression of probe current during alternate half cycles of the modulation to indicate a measurement of positive ion current while in the electron current mode. Inspection of the record of dc probe current on Nike Apache 14.244 indicates similar modulation in the same height range but smaller in magnitude. This payload also included a 600 volt power supply. The modulation is not seen in earlier flights, none of which used the 600 volt power supply.

UV Instrumentation

Details of the Lyman-α ion chamber technique have been presented in an earlier report,[2]. All measurements with this instrument have been successful in this program.

The 1450Å photometer design has undergone a number of modifications. In one rocket flight (Nike Apache 14.228) and in the earlier series of flights in the 1964 program, an ion chamber consisting of 1/2-mm sapphire and 1 to 2 mm p-xylene fill gas was used. This gas-window combination provides the spectral bandpass of 1425 to 1480Å. Contrary to the results obtained by Friedman, et al., [4], an ion chamber response at the top of the atmosphere of 10^{-10}A per cm^2 of window area could not be attained. In fact, the absence of a measurable current on any of the rocket flights containing this ion chamber showed that the response at the top of the atmosphere was less than 5×10^{-12}A per cm^2 of window area.

As a result of this low sensitivity and the consequent lack of useful absorption data, barium fluoride windows were substituted for sapphire to extend the high energy wavelength limit down to 1350Å and thus increase the output current. In Nike Apache 14.231, this ion chamber gave a maximum current at the top of the atmosphere of 1.6×10^{-10}A and thus allowed a successful measurement; however, in the following flight, Nike Apache 14.232, the ion chamber did not provide a sufficiently high current output. The observed Lyman-α flux was unusually low, and it is thought that some contamination of the environment of both ion chambers prior to flight may have caused the resulting loss of efficiency.

Since the quality of the measurement had to be improved, the spectral band was again narrowed with sapphire and the efficiency increased by operating the photometer in the gas-gain mode in Nike Apache flights 14.244 and 14.247. A gain of about 18 was obtained with an applied voltage of 650V on the first flight, and with a current at the top of the atmosphere of 8×10^{-11}A a useful profile was measured. In the later flight, no signal was obtained, and it is believed that the door covering the photometer did not eject.

An ion chamber sensitive to the spectral range 1225 to 1350Å has also been used in several flights (Nike Apache 14.245 and 14.246). This spectral band is achieved by means of a 2 mm thick calcium fluoride window and 20 mm nitric oxide gas fill. Besides providing molecular oxygen data, this ion chamber permits useful corrections to be made to the Lyman-α ion chamber data. Both measurements with it have been successful.

ELECTRON DENSITY OBSERVATIONS

E and F1 Regions

The results of the probe data for the E and F1 regions obtained from the series of flights in the South Pacific are shown in Figure 3. The probe currents have been normalized to unity at 110 km (E layer) for comparison. Two cases of spordic E are noted: a layer on flight 14.228 at 115 km and an intense layer on flight 14.232 at 100 km. Further details of this intense layer are shown in Figure 4. The data points in this figure are separated by 0.01 sec in time, corresponding to 12.8 meters in altitude, and clearly illustrate the extremely large gradients in electron density at the top and bottom of the layer. Except for sporadic E, the four profiles in Figure 3 do not show significant differences below 150 km. At higher altitudes, the low latitude measurements (14.228, 14.230) indicate lower electron densities than the mid-latitude measurements. Since all four flights occurred near the same zenith angle, these results suggest a latitude effect in the F1 region.

The results from the two summer flights, Nike Apaches 14.245 ($\chi \approx 95^{\circ}$) and 14.246 ($\chi \approx 61^{\circ}$), are shown in Figures 5 and 6. The highly irregular structure for Nike Apache 14.245 in contrast to 14.246 from 95 to 120 km is characteristic of nighttime measurements.

The data from Nike Apache 14.244 in Figure 7 shows a sporadic E layer at 106 km. The maximum plasma frequency of the layer was evidently greater than 3.385 MHz (equivalent to an electron density of 1.4×10^5 cm^{-3}) since the signal of that frequency used in the CW propagation experiment did not penetrate the layer. No signal on this frequency was received at the rocket until the rocket descended through the layer at a horizontal distance of 104 km from where it had ascended through the layer. The tilt* of this layer is found to be only $0^{\circ}48.7'$. The ionosonde data shows a blanketing frequency of sporadic E of 3.2 Mc/sec, 2 minutes before launch, and this had increased to 4.0 MHz when sounding was resumed 10 minutes later.

The profile of probe current obtained during the ascent of Nike Apache 14.247 is shown in Figure 8. The electron density scale (upper edge of graph) is provisional and is subject to revision when the data from the CW propagation experiment becomes available. Two sporadic E layers are seen, the lower one at 96 km, about 4 km thick, and an upper one at 113 km, about 2 km thick. These layers are also both seen on the descent profile. Layers similar to these have been seen separately on previous profiles, but this is the first time that two distinct daytime Es layers have been seen on the same flight. The layers are close to horizontal: the tilt is only $-0^{\circ}16.0'$ for the lower layer and $-0^{\circ}32.7'$ for the upper layer. An unusual feature of the profile is the irregular nature between 104 km and the lower edge of the upper Es layer (that is, 112 km) compared with the normal smoothness of the profile from 98 to 105 km and above 114 km.

---

* Tilts are positive when the level for ascent is less than the level for descent.

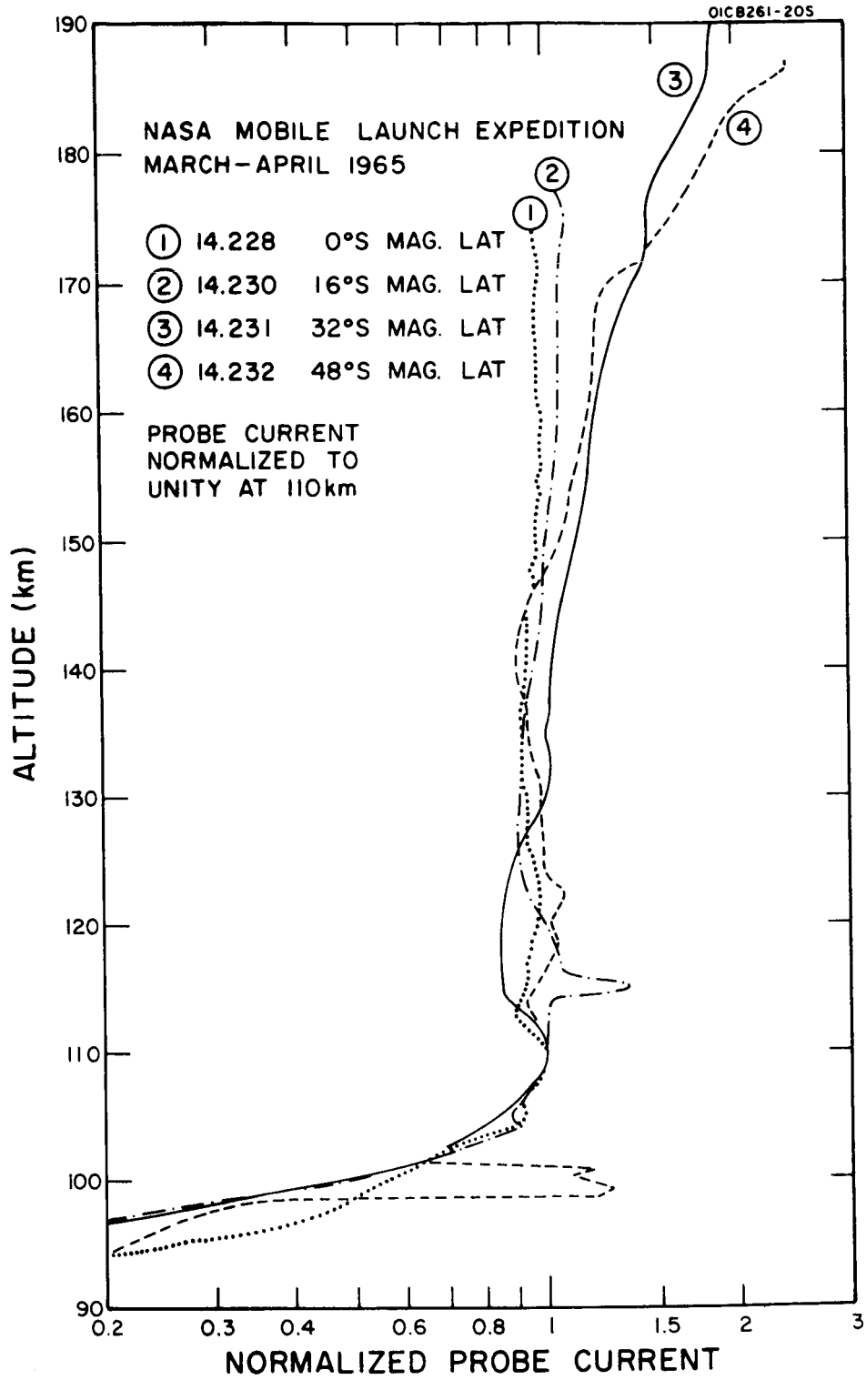

Figure 3. E and F1 region profiles normalized at 110 km.

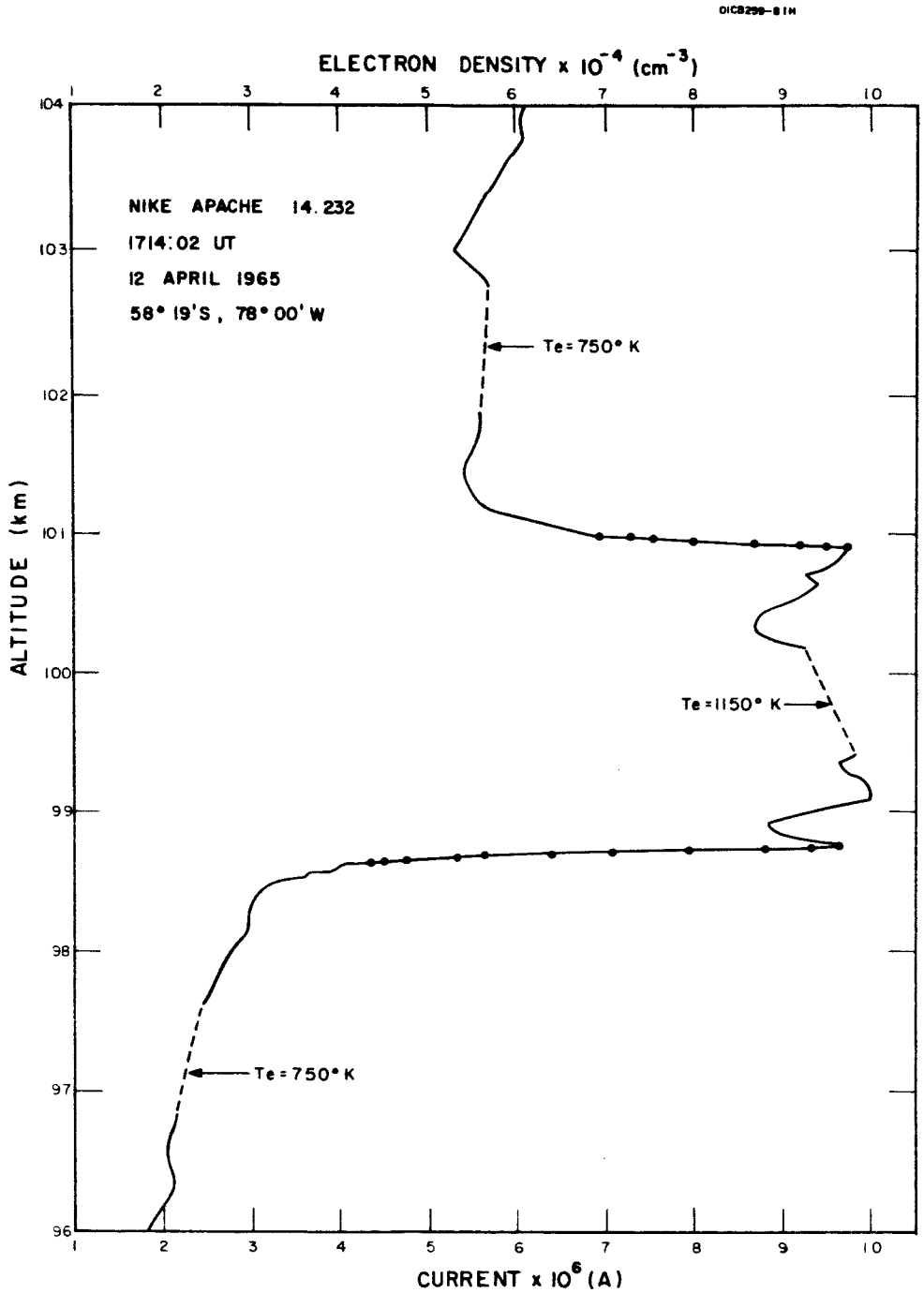

Figure 4. Daytime Es layer and electron temperatures.

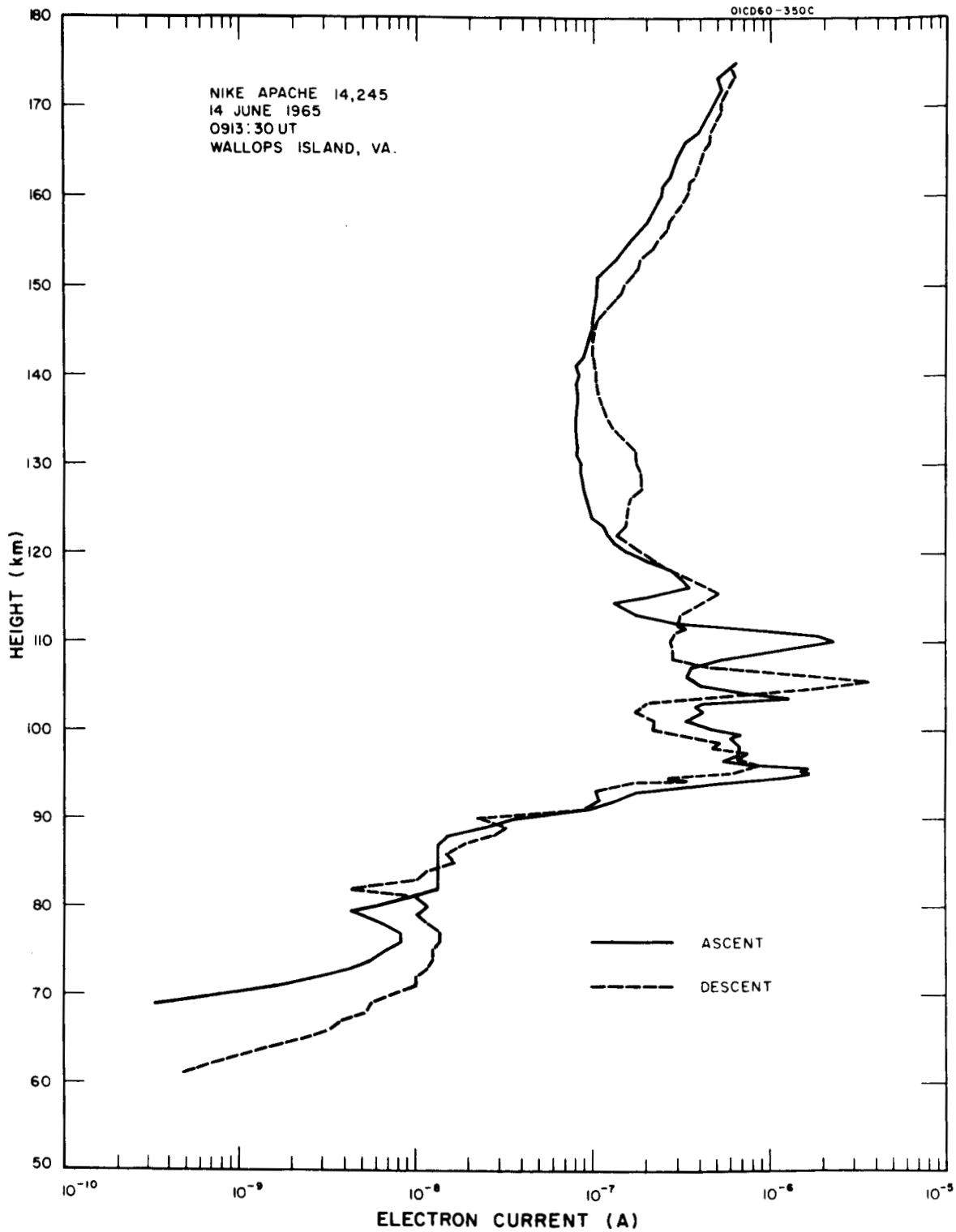

Figure 5. Summer predawn E and F1 region profile.

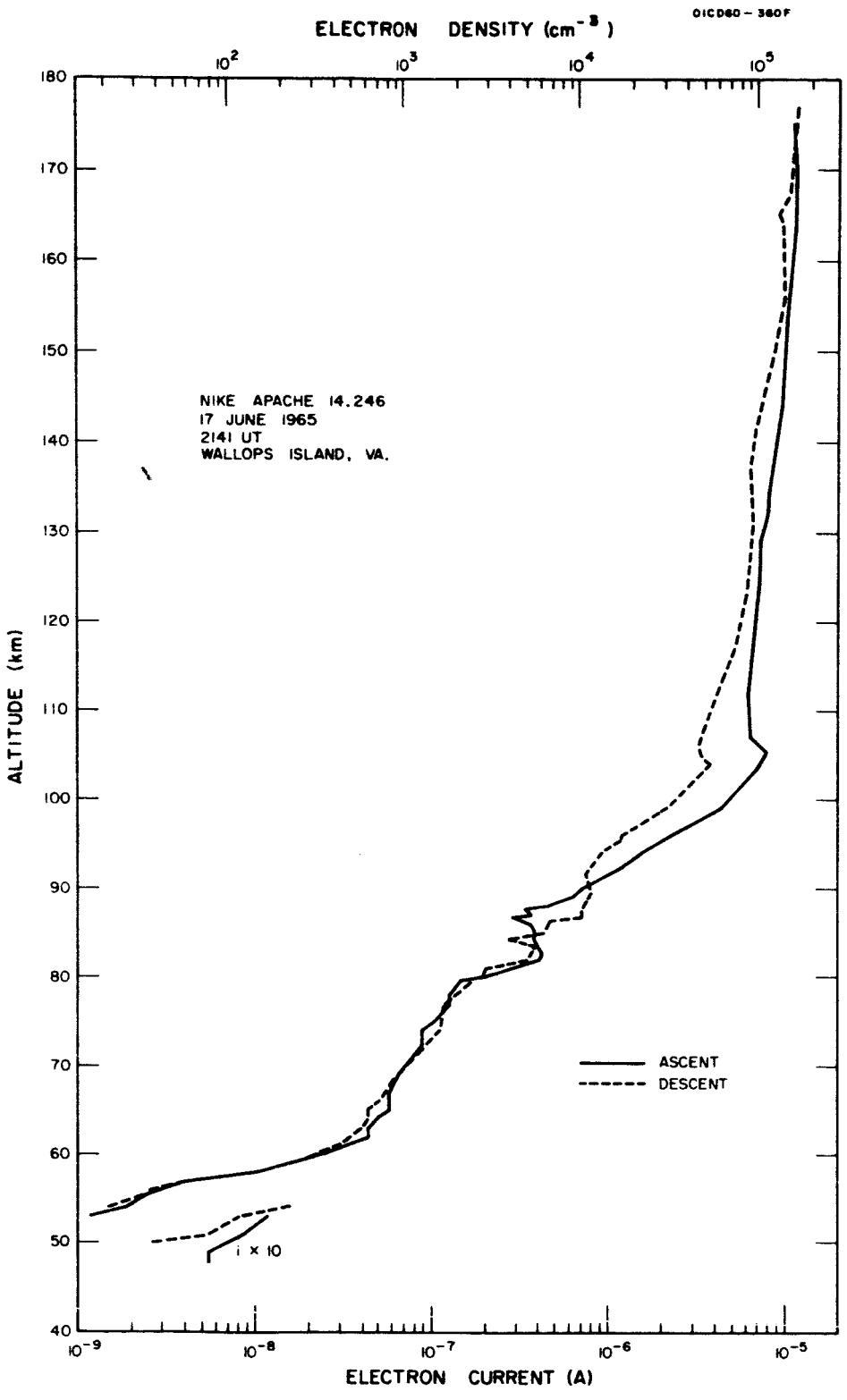

Figure 6. Summer afternoon E and F1 region profile.

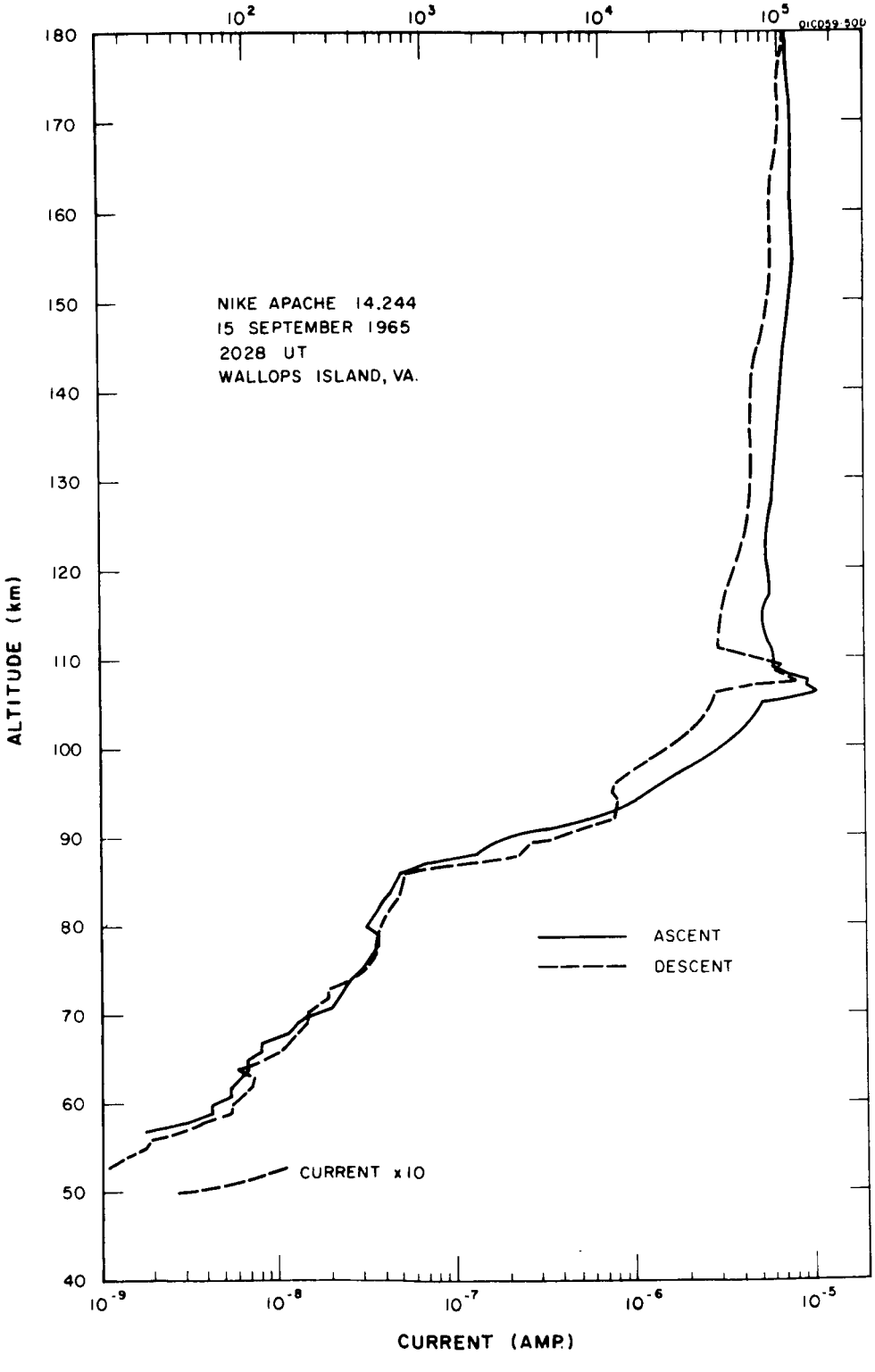

Figure 7. Fall afternoon E and F1 region profile.

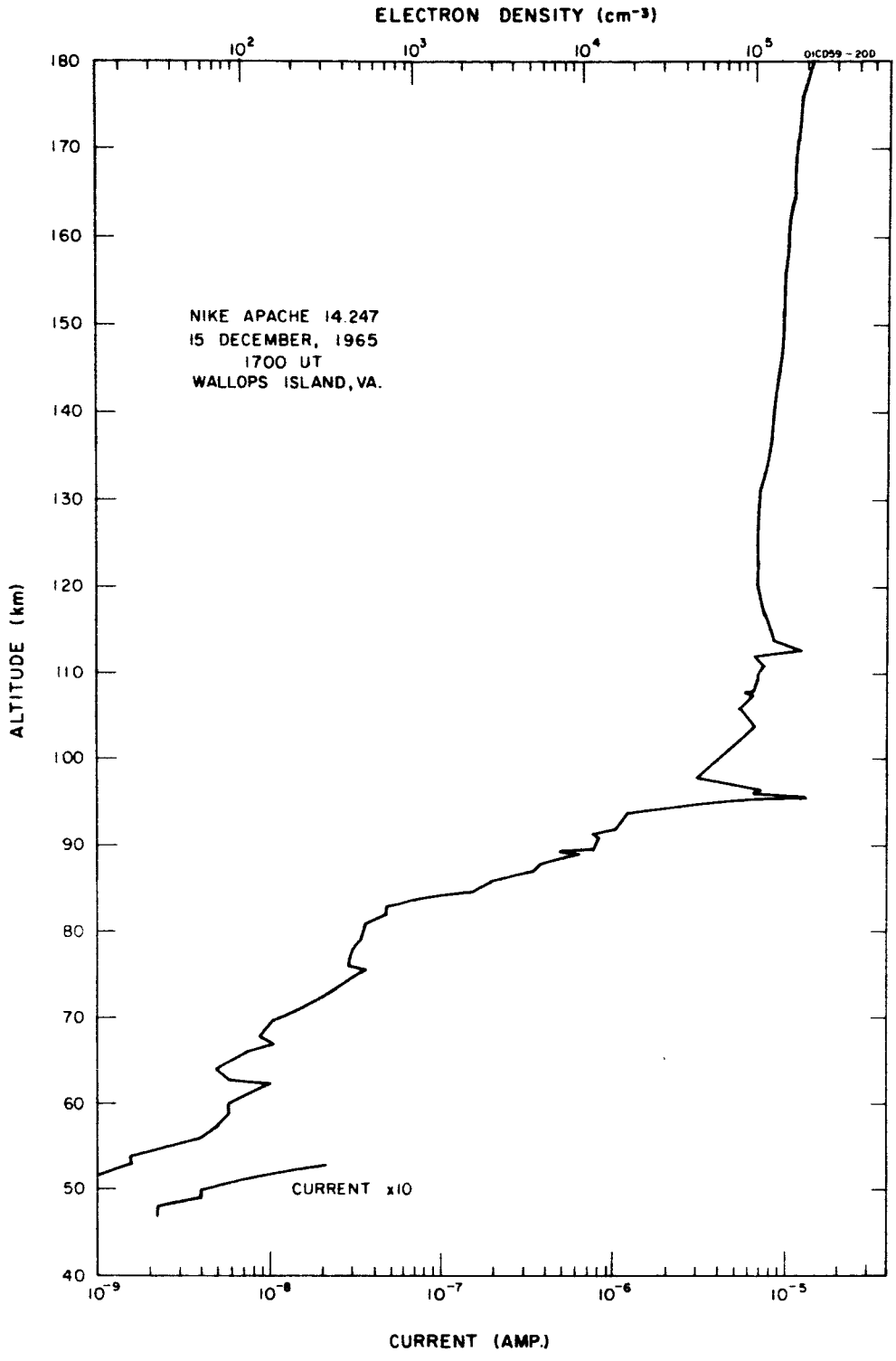

Figure 8. Winter afternoon E and F1 region profile.

D Region

In Figure 9, Nike Apache flights 14.228, 14.230, and 14.231 are shown. The variation in current from one flight to another exhibits the normal variability to be expected for the undisturbed D region. The profile for flight 14.232 at the larger zenith angle is shown separately in Figure 10. This profile indicates generally lower densities than the earlier flights but is not considered significantly different in view of the irregularity of the D region from day to day.

The D region structure observed in Nike Apache 14.245 is shown in Figure 11. At 80 km, the zenith angle is 94.77 degrees on ascent and 93.34 degrees on descent. The effect of this small difference in zenith angle is clearly seen in the development of the C layer, which extends below 79.5 km on ascent and 82.0 km on descent. The enhancement of ionization as the sun's elevation angle increases is attributed to the photodetachment of negative ions by the solar uv radiation between 1800 and 2900Å [5].

The profile of 14.247 between 50 and 95 km is shown in Figure 12, which also shows the profile from Nike Apache 14.246, launched 17 June 1966, also at $\chi \approx 60^{\circ}$. These are therefore representative of winter and summer, respectively. The two profiles are nearly identical in two height intervals: 53 km (the lowest significant data point) to 57 km and from 87 km to 94 km. Between 57 and 87 km there is a marked difference, much larger than can be attributed to experimental errors. Through most of this height range (say 60 to 83 km) the probe current is larger by a factor of about 5 in the summer profile than in the winter profile. Assuming that the probe current is proportional to electron density and that the recombination coefficient, though a function of altitude, does not change daily, it is seen that the ionization rate $q(= \alpha n^2)$ is lower in winter than in summer by a factor of 25 between 60 and 83 km. Since both profiles were obtained at nearly the same solar zenith angle, it must be concluded that the difference is not attributable to the ionizing radiation (Lyman-α), but rather to a difference in the number density of the constituent being ionized (nitric oxide), by the same factor of 25. This is probably the clearest illustration yet obtained of the importance of minor constituents of the (neutral) atmosphere in the formation of the ionospheric layers.

Figure 13 shows a comparision of two winter profiles. One is from the previous two figures (that is, Nike Apache 14.247). The other is that obtained nearly four weeks later on a day of high absorption (from Nike Apache 14.248). The probe current (electron density) on the day of high absorption is the greater above 63 km to the greatest altitude that data was obtained (93 km). The most interesting feature of the January profile is the steep gradient between 80.6 and 82.2 km and the relatively high value of electron density indicated at 82.2 km. This high electron density can be identified as the probable cause of the high absorption.

The general difference between the two profiles could possibly to interpreted as a difference in the solar radiation; however, the steep gradient is virtually impossible to interpret on the basis of solar radiation alone. It is believed that the explanation lies in the role of the minor constituents.

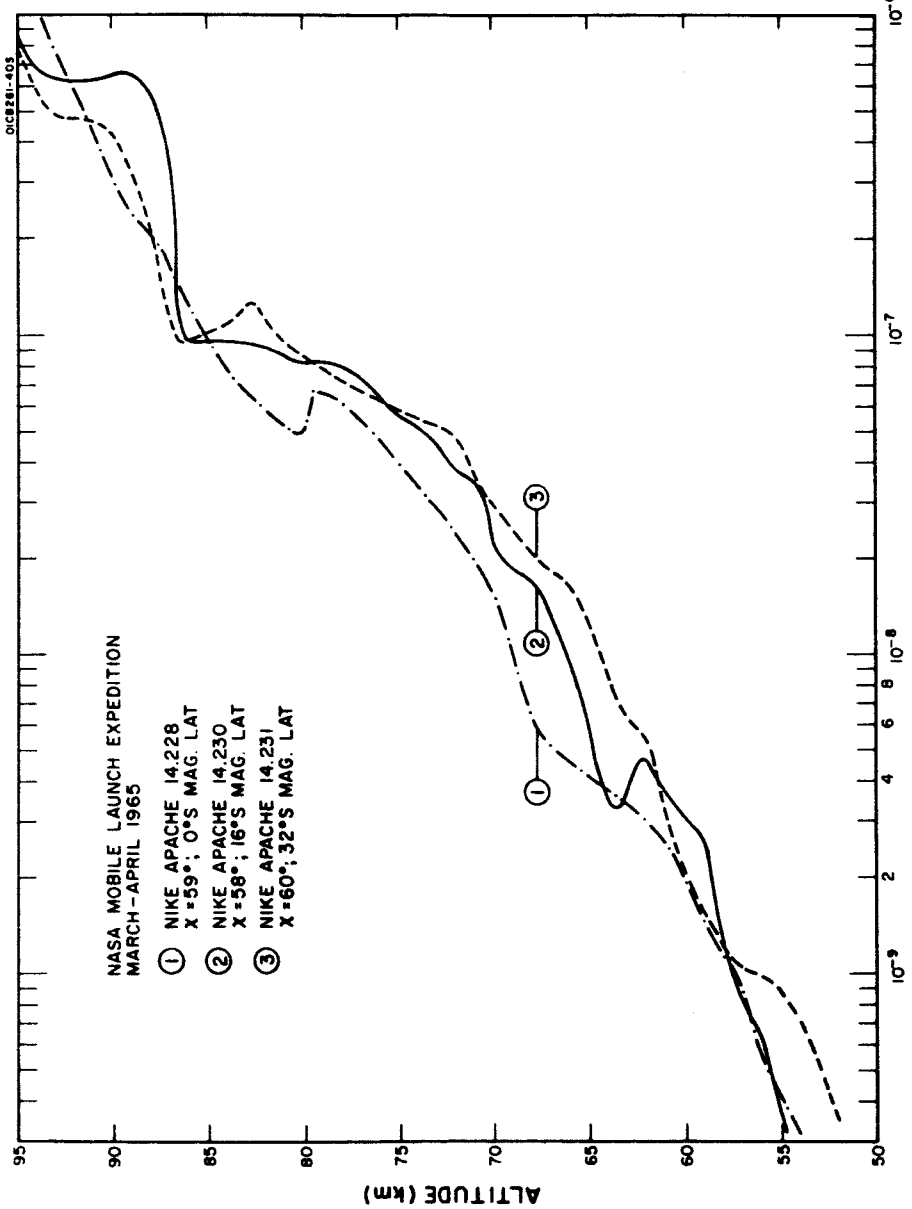

Figure 9. D region current profiles for zenith angles near 60°.

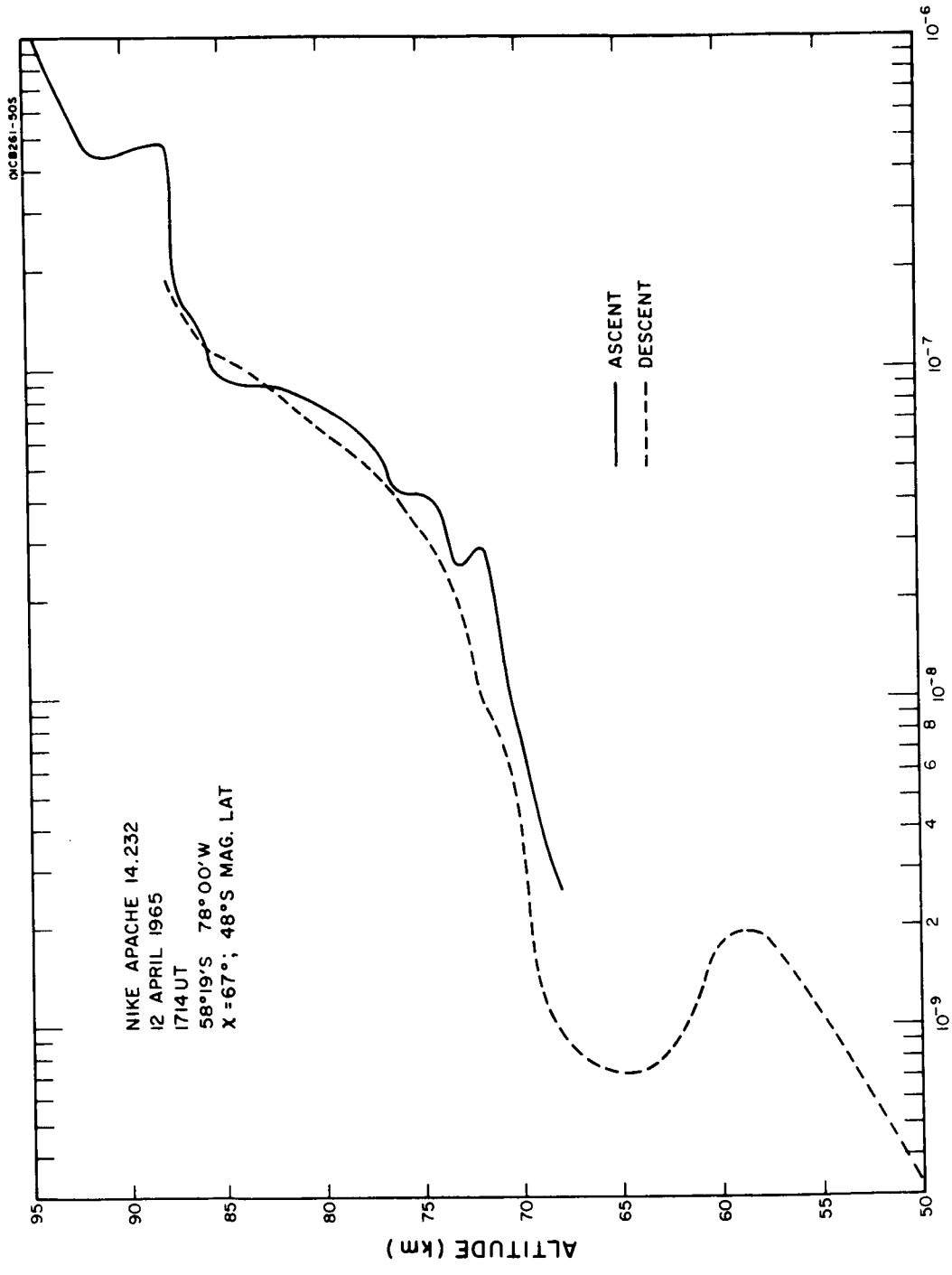

Figure 10. D region current profile for 67^{o} zenith angle.

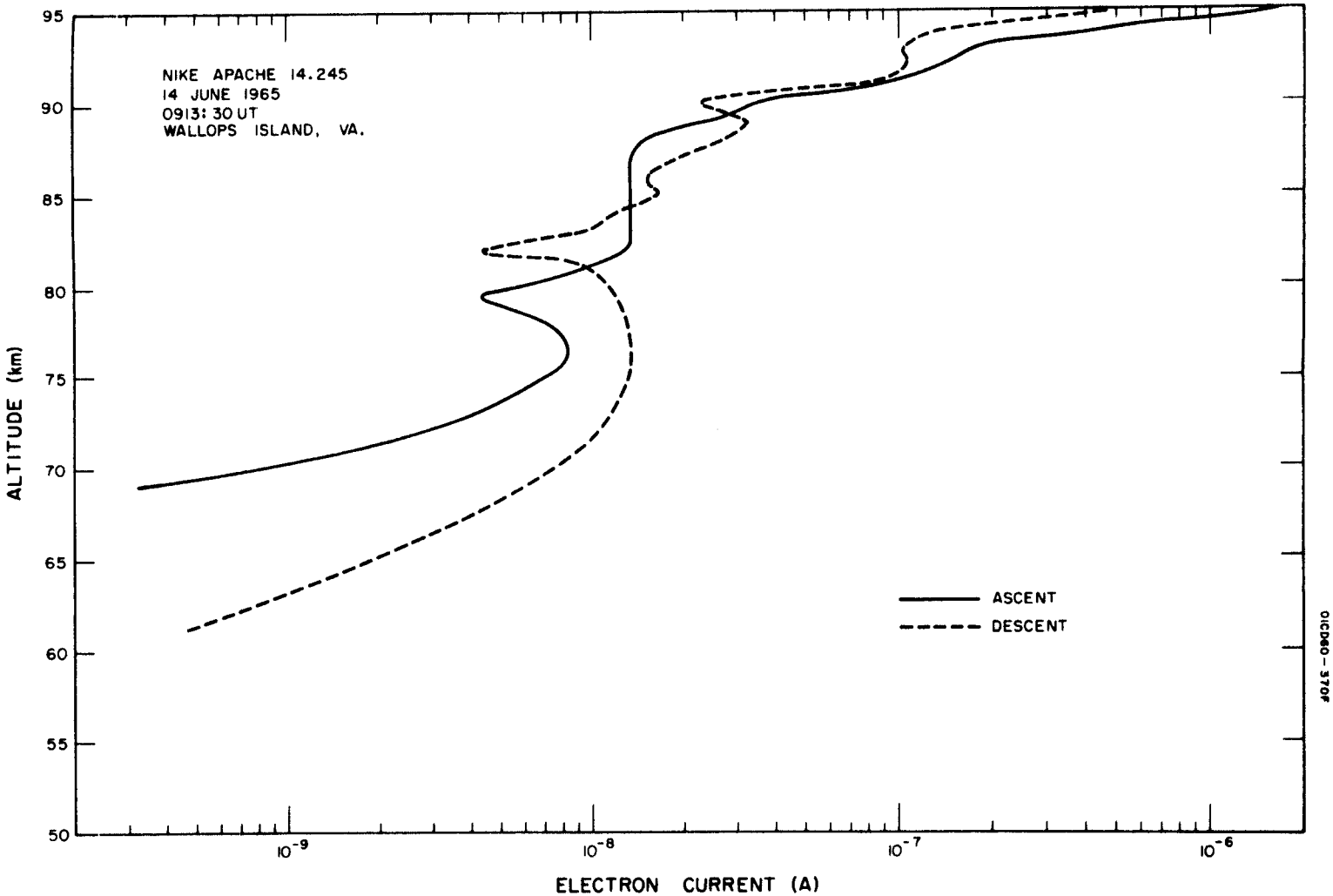

Figure 11. D region current profiles near 95° zenith angle (predawn).

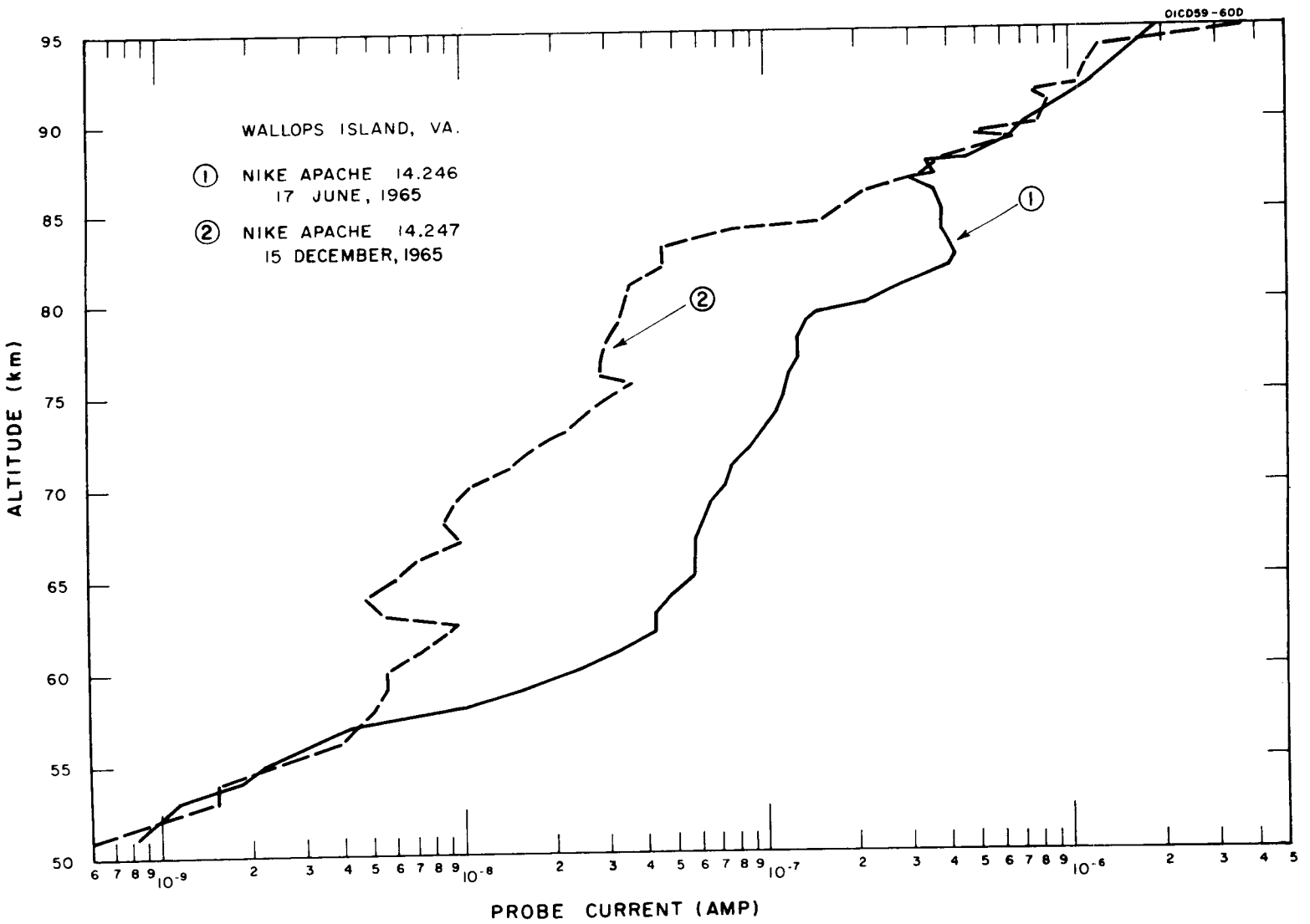

Figure 12. D region current profiles for summer and winter for zenith angles near 60^{o}.

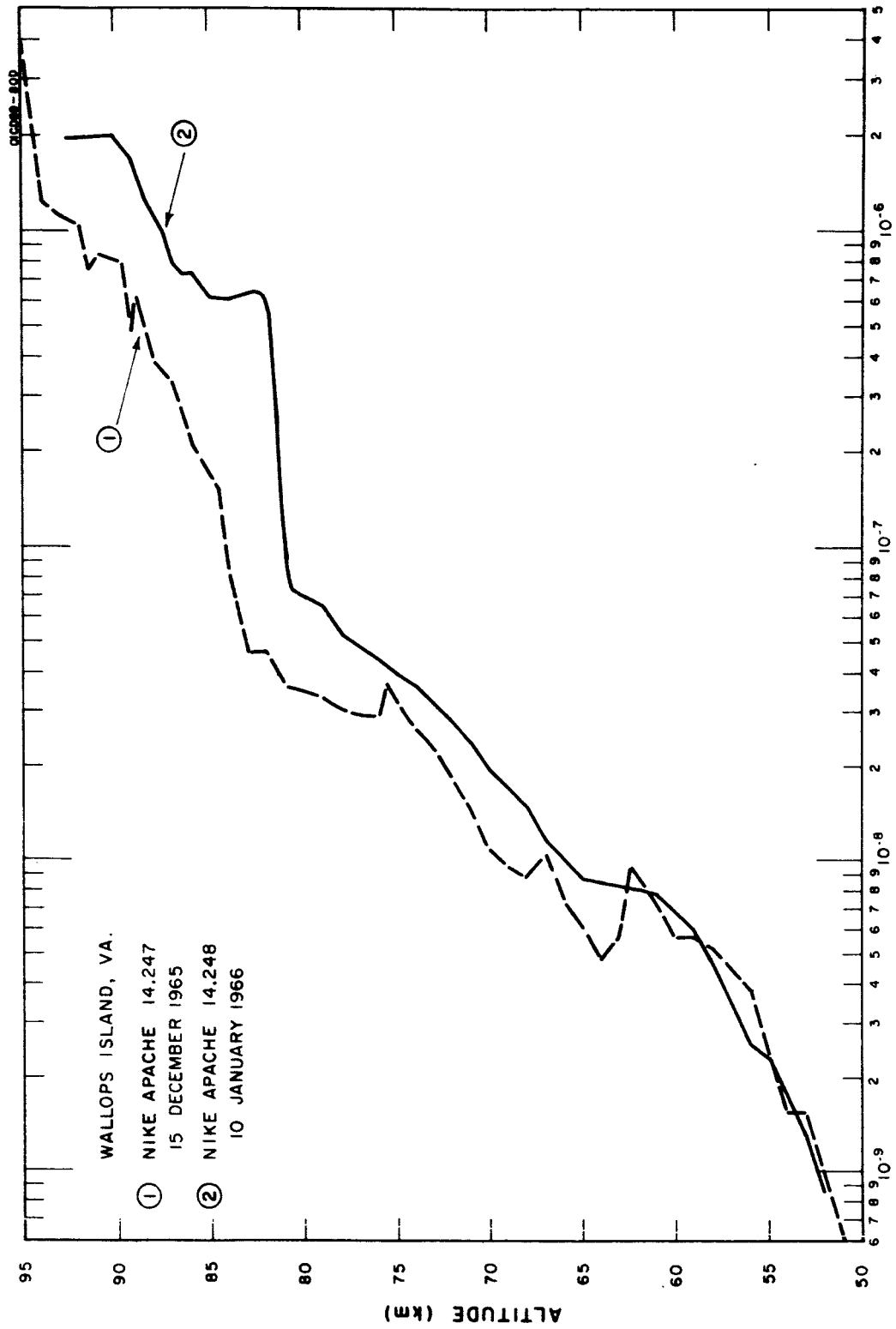

Figure 13. D region current profiles illustrating day of anomalous absorption.

ELECTRON TEMPERATURE DATA

The nose probe voltage sweep from -2.7 to +2.7 volts at intervals of two seconds gives information on electron temperature. Usable data is available only above about 100 km in the daytime flights because the electron densities at lower altitudes are not sufficiently large to permit an accurate sweep analysis. This method of analysis is valid only if the electron density does not change significantly during the half second time of the voltage sweep. Therefore, the amount of temperature data available from nighttime measurements, where large changes in electron density characteristically occur above 110 km, is even more limited.

The temperature analysis for four flights has been completed. The results for Nike Apache 14.232 are shown in Figure 14 and are illustrative of a usually large spread in the data points. The median value for the entire altitude range is 806°K, the spread is 511°K to 1184°K, and the data shows no apparent altitude trend. The error bars of ±100 degrees about the data points indicate the best accuracy possible by this method, but the accuracy of this data is estimated to be only ±200 to 300°K if it is assumed that the fluctuations shown in the figure do not represent true fluctuations. For this flight, temperatures were obtained in and adjacent to a sporadic E layer, shown in Figure 14, where the temperature sweeps are denoted by dotted lines. The temperature in the layer is somewhat above the adjacent regions, but most noteworthy is its high value of 1150°K. This is the highest value reported yet in a sporadic E layer [6].

The electron temperatures obtained for Nike Apaches 14.246, 14.244, and 14.247 are given in Figures 15, 16, and 17. Except for the data below about 110 km, where the uncertainties are very large, the experimental accuracy for 14.246 and 14.244 is about ±200°K, and for 14.247 it is estimated to range from ±100 to 150°km. Altitude structure is seen in this data, with an approximate increase of 100 degrees every 10 km. The lack of a discernible altitude structure such as this in the measurements of Nike Apache 14.232 may be due to the larger experimental errors since no geomagnetic or solar disturbances were noted then.

Little temperature data could be obtained from Nike Apache 14.245 because of the characteristically irregular nighttime electron density profile that was observed. Very high temperatures of 2124°K observed at 103 km and 1555°K at 110 km on ascent may reflect a heating effect from radio signals transmitted by station WTOP; however, insufficient electron temperature data has been obtained to arrive at an uncertainty and make any strong conclusions.

The results of all the daytime flights have been analyzed over the interval 140 to 150 km. The mean temperatures and standard deviations are given in Table VIII. No relation to the 3-hourly geomagnetic activity index a_p or the daily average activity index A_p was seen, although other data [7] have suggested a correlation. Also, no correlations with latitude or season are seen.

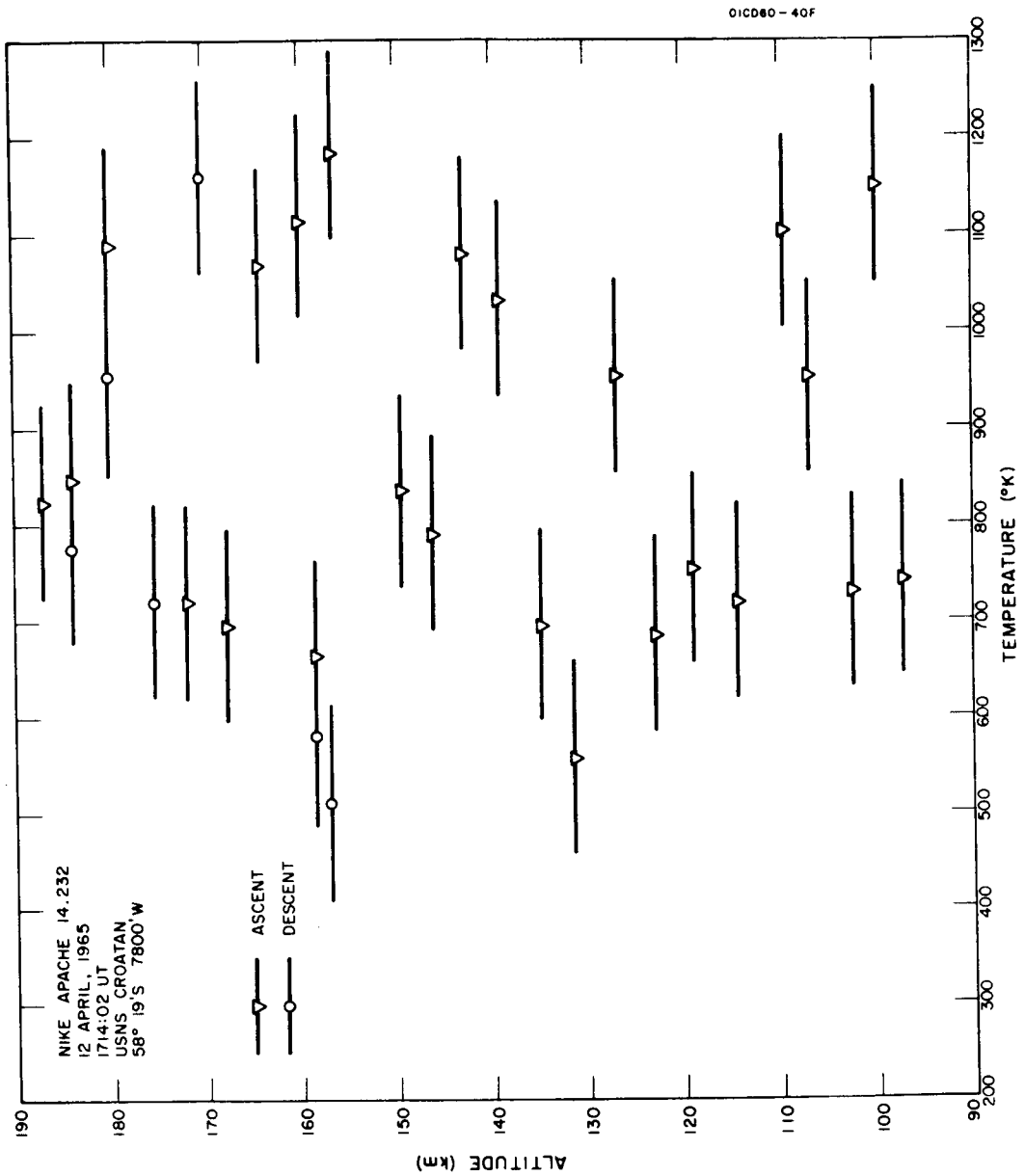

Figure 14. Electron temperatures for Nike Apache 14.232.

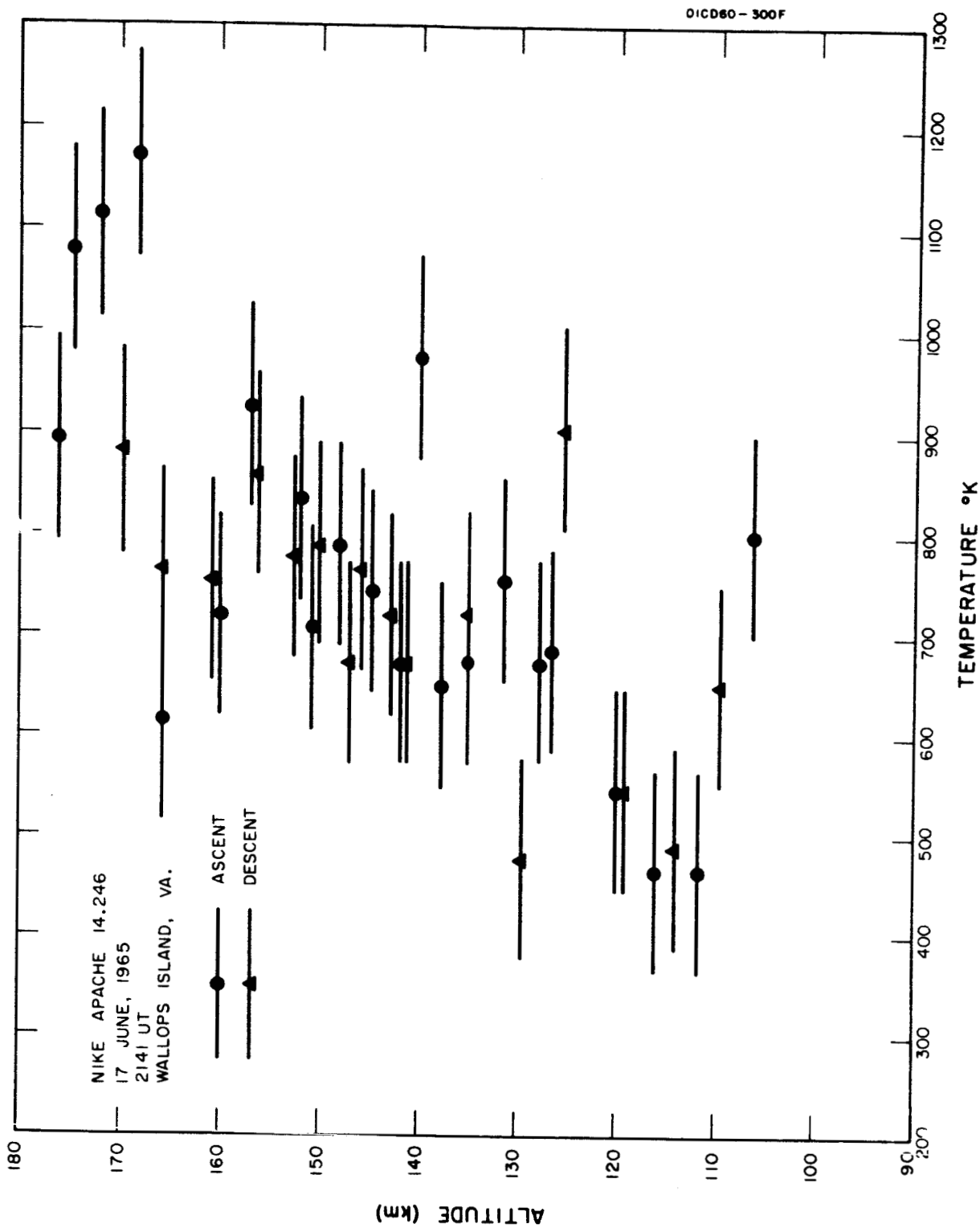

Figure 15. Electron temperatures for Nike Apache 14.246.

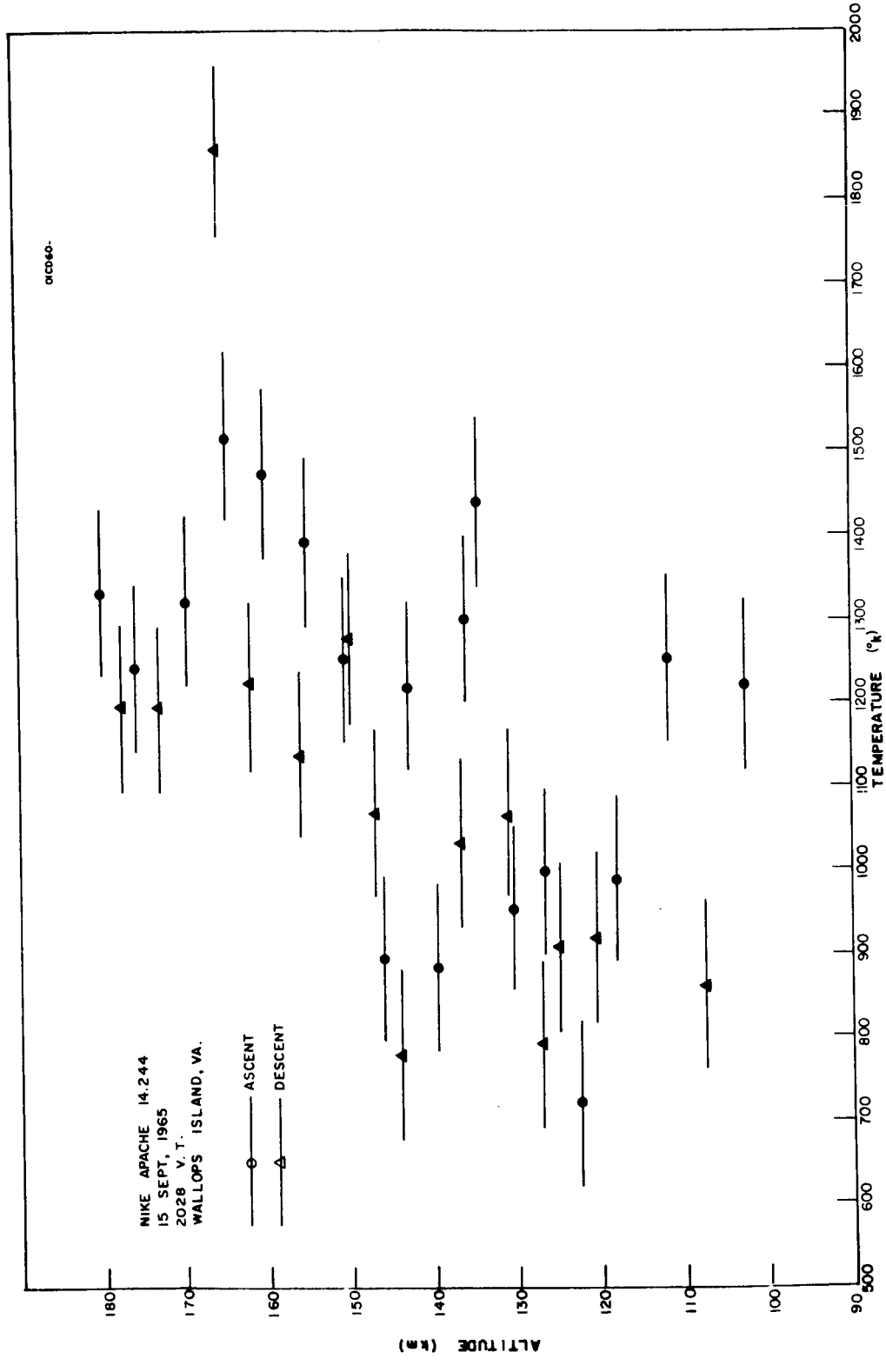

Figure 16. Electron temperatures for Nike Apache 14.244.

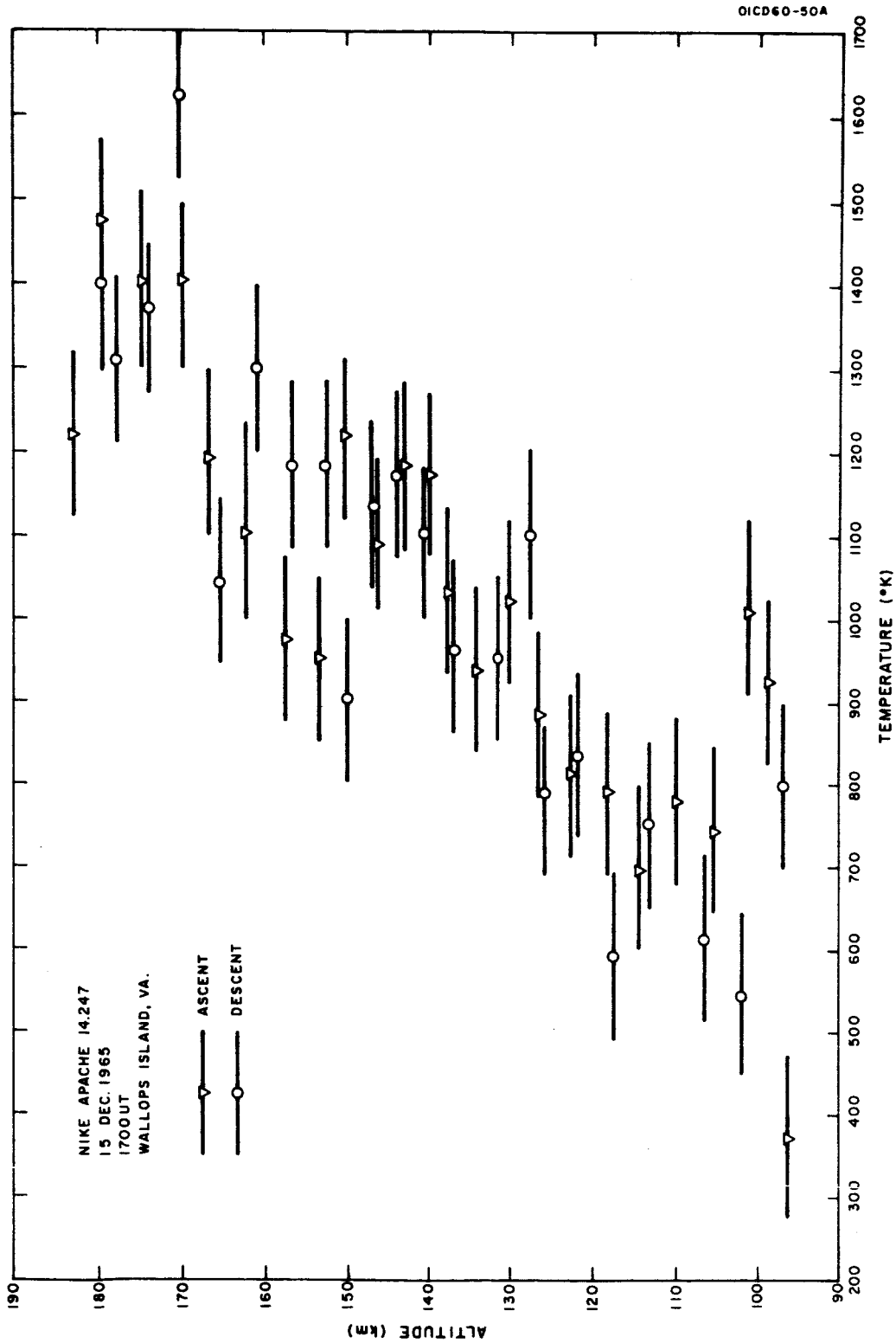

Figure 17. Electron temperatures for Nike Apache 14.247.

TABLE VIII

MEAN ELECTRON TEMPERATURES FOR ALTITUDE RANGE 140 TO 150 KM

Nike Apache Designation	Mean Electron Temperature and Standard Deviation (^{O}K)
14.228	1200 ± 99
14.230	724 ± 63
14.231	659 ± 41
14.232	901 ± 90
14.246	756 ± 32
14.244	1000 ± 65
14.247	1109 ± 37

MOLECULAR OXYGEN DENSITY OBSERVATIONS

Introduction

In six of the type A payload flights, data has been obtained which has provided information on the molecular oxygen distribution from 70 to 154 km. As in the 1964 program, measurements of the Lyman-α profile were obtained with ion chambers in this program. In addition, some measurements were obtained with other uv photometers. A summary of pertinent rocket flights and the photometers providing useful data are presented in Table IX. The photometer characteristics are summarized in Table X.

TABLE IX

FLIGHT CONDITIONS FOR THE VARIOUS UV MEASUREMENTS

Nike Apache Designation	Date	Photometer (Window-Gas)	Latitude of Rocket	Solar Zenith Angle
14.228	20 March 65	LiF - NO	13.0°S	60°
14.231	9 April 65	LiF - NO BaF_2 - p-xylene	44.2°S	59°
14.232	12 April 65	LiF - NO	58.3°S	67°
14.245	14 June 65	LiF - NO CaF_2 - NO	37.8°N+	94°
14.246	17 June 65	LiF - NO CaF_2 - NO	37.8°N	61°
14.244	15 Sept 65	LiF - NO Al_2O_3 - p-xylene	37.8°N	60°
14.247	15 Dec 65	LiF - NO	37.8°N	61°

+The measurements refer to a latitude of 39.5 to 40.3°N. See text.

TABLE X

UV PHOTOMETERS FOR MOLECULAR OXYGEN MEASUREMENTS

Spectral Range	Window	Gas	Approximate Useful Altitude Range for $\chi = 60^{o}$	Characteristics
1050-1350Å	LiF	nitric oxide	70- 94 km	Essentially monochromatic response to solar Lyman-α
1225-1350Å	CaF_2	nitric oxide	92-130 km	Radiation selectively absorbed - changing effective cross section
1350-1480Å	BaF_2	p-xylene	115-140 km	Radiation selectively absorbed - changing effective cross section
1425-1480Å	sapphire	p-xylene	115-154 km	Constant effective cross section

Absorption spectroscopy was used to achieve molecular oxygen concentrations: the flux of radiation from the sun in a given spectral band is measured as the optical path in the absorbing region is changed. From this transmission data and the appropriate cross sections, the altitude distribution of the absorber is obtained. Since molecular oxygen is a dominant absorber between 1000 and 2000Å, photometers sensitive to various spectral bands in that wavelength region are useful for making the measurements. The altitude range for the measurements is set by the optical depth, or is proportional to the effective absorption cross section of the absorbing species - in this case, molecular oxygen - in the bandpass of the photometer, and the optical depth factor determined by the solar zenith angle. The approximate altitude ranges for $\chi = 60$ degrees is given in Table X.

Method of Data Analysis

Since the Lyman-α ion chamber response is almost entirely due to the solar Lyman-α line over a range of several scale heights, the effective absorption cross section σ can be treated as a constant value. The molecular oxygen density then is computed from:

$$n[O_2] = \frac{1}{\sigma F} \frac{1}{I} \frac{dI}{dz} \text{ for } \chi \leq 90^\circ \tag{1}$$

and

$$n[O_2] = \frac{1}{\sigma F} \frac{1}{I} \frac{dI}{dh} \text{ for } \chi \geq 90^\circ \tag{2}$$

where I is the ion chamber current, z is the rocket altitude, and h is the minimum ray height. F is the optical depth factor, and for the case of negligible scale height gradient, F is given by:

$$F = \frac{101.4}{H^{1/2}} \left[1 - \text{erf} \frac{(90-\chi)}{H^{1/2}}\right] \exp\left[\frac{(90-\chi)^2}{H}\right] \text{ for } \chi \leq 90^\circ \tag{3}$$

and

$$F = \frac{101.4}{H^{1/2}} \left[1 + \text{erf} \frac{(\chi-90)}{H^{1/2}}\right] \text{ for } \chi \geq 90^\circ \tag{4}$$

where H is the scale height of the absorbing constituent. The following approximations are useful in special cases, for an error not exceeding about 10 percent:

$$F = \sec \chi \text{ for } \chi \leq 85^\circ \tag{5}$$

and

$$F = \frac{202.8}{H^{1/2}} \text{ for } \chi \geq 93^\circ \tag{6}$$

In the above formulae, it is assumed that the scale height H is a constant. This is often a good assumption in the height range 70 to 110 km, but at higher altitudes there are significant scale height gradients. It can be shown that the neglect of the scale height gradient in certain height ranges introduces insignificant errors [8].

The photometer sensitive to the bandpass 1425 to 1480Å provides information on a portion of the spectrum where the absorption cross section of molecular oxygen varies by only 15 percent. For this reason, the effective cross section for the radiation being measured may be considered constant over the useful altitude range. The computation of density is the same as if all the radiation measured were monochromatic at a wavelength having a cross section equal to the effective cross section. Formulae (1) and (2) then may be used in the data analysis. Whereas for the Lyman-α ion chamber the pertinent cross section is 10^{-20} cm^2, for this photometer the effective cross section is taken to be 14.0×10^{-18} cm^2.

The bandpasses of the 1350 to 1480Å and 1225 to 1350Å ion chambers are large enough to require more elaborate calculations. The required quantities are the incident solar flux $\mathcal{Q}_o$, the molecular oxygen obsorption cross section σ, and the ion chamber quantum efficiency β, all as a function of wavelength λ over the bandpass $\Delta\lambda$ of the instrument. By integration, the ion chamber current I can be computed as a function of the columnar density of $n_T(O_2)$ between the ion chamber and the sun according to

$$\frac{I(n_T)}{I_o} = \frac{\int_{\Delta\lambda} \beta(\lambda)\ \mathcal{Q}_o(\lambda)\ \exp\ (-\sigma\ n_T)\ d\lambda}{\int_{\Delta\lambda} \beta(\lambda)\ \mathcal{Q}_o(\lambda)\ d\lambda} \tag{7}$$

where I_o is the ion chamber current when exposed to the unattenuated solar radiation. Note that only relative values of β and $\mathcal{Q}_o$ are required in the computation. When $I_o(\lambda)$, $\sigma(\lambda)$, and $\beta(\lambda)$ are known, a calibration curve (I/I_o vs n_T) can be computed. From this calibration curve and the flight data, the quantity n_T is obtained. Finally $n[O_2]$ is obtained as a function of height from

$$n[O_2] = \frac{1}{F}\ \frac{dn_T(z)}{dz} \quad \text{for } \chi \leq 90^o \tag{8}$$

and

$$n[O_2] = \frac{1}{F}\ \frac{dn_T(h)}{dh} \quad \text{for } \chi \geq 90^o \tag{9}$$

As wavelength calibrations have not been made for these ion chambers, information on $\beta(\lambda)$ is based on other published data. The incident solar flux $\mathcal{Q}_o(\lambda)$

is taken from Schultz and Holland [9] which is believed to be a reasonably good approximation to the actual conditions in flight. The cross sections are probably the most accurately known quantities and are taken from Watanabe, et al. [10,11]. The calibration curves are given in Figure 18.

The aspect corrections for the various photometers are obtained empirically during flight from the rocket precessional motion. Near rocket apogee the solar flux may be assumed constant and the variation in ion chamber current considered to be entirely caused by change in aspect angle. The ratio of the current at an aspect angle α to that at normal incidence ($\alpha = 0^o$) is plotted against angle to give the calibration curve.

Computation of Zenith Angle and Minimum Ray Height

The solar zenith angle can be computed for any given point in the rocket trajectory from the radar data. The information which determines this angle is the latitude and longitude of the sub-rocket point (that is, the point where the line from the rocket to the earth's center crosses the earth's surface) and the Universal Time. Data from "The American Ephemeris and Nautical Almanac" (or its equivalent) of the appropriate year, is also required.

The formulae used in the zenith angle computation are:

$$h = \text{local sidereal time} - \alpha, \text{ and} \tag{10}$$

$$\cos \chi = \sin \varphi \sin \delta + \cos \varphi \cos \delta \cos h, \tag{11}$$

where h is the hour angle, α is the right ascension, φ is the latitude of sub-rocket point, and δ is the declination.

The minimum ray height, used when the zenith angle is greater than 90^o, is given by the following expression

$$h = (R + x) \cos (\chi - 90) - R' \tag{12}$$

and the distance from the rocket to the point of minimum ray height

$$s = (R+z) \sin (\chi-90) \tag{13}$$

Figure 19 illustrates the geometry when $\chi > 90^o$. The difference in the latitude of the sub-rocket point A and the latitude of the position on the earth's surface directly below the point defining the minimum ray height B requires that the computation include a correction for the variation in the earth's radius with latitude. This is taken into account in the calculations by using Hayford's spheroid as the model for the earth. At midlatitudes, this amounts to approximately 3.5 km in 10^o latitude change. The change in the minimum ray height between A and B will be the same (but opposite sign) as this change in R and is usually not negligible. This effect is taken into account by Formula (12). Details of the computer program used in the analysis are given in Appendix C.

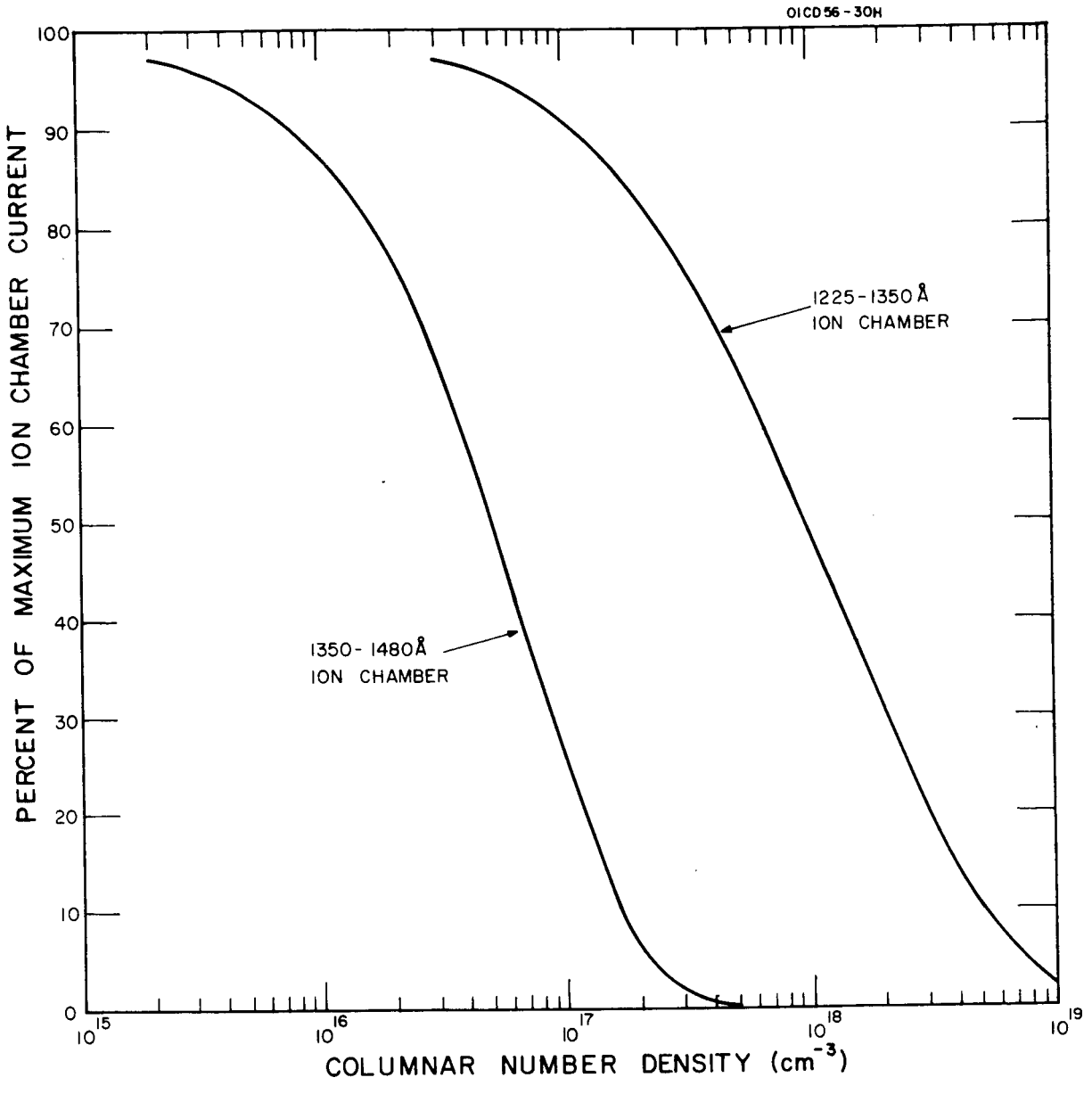

Figure 18. Calibration curves for 1225-1350Å and 1350-1480Å ion chambers.

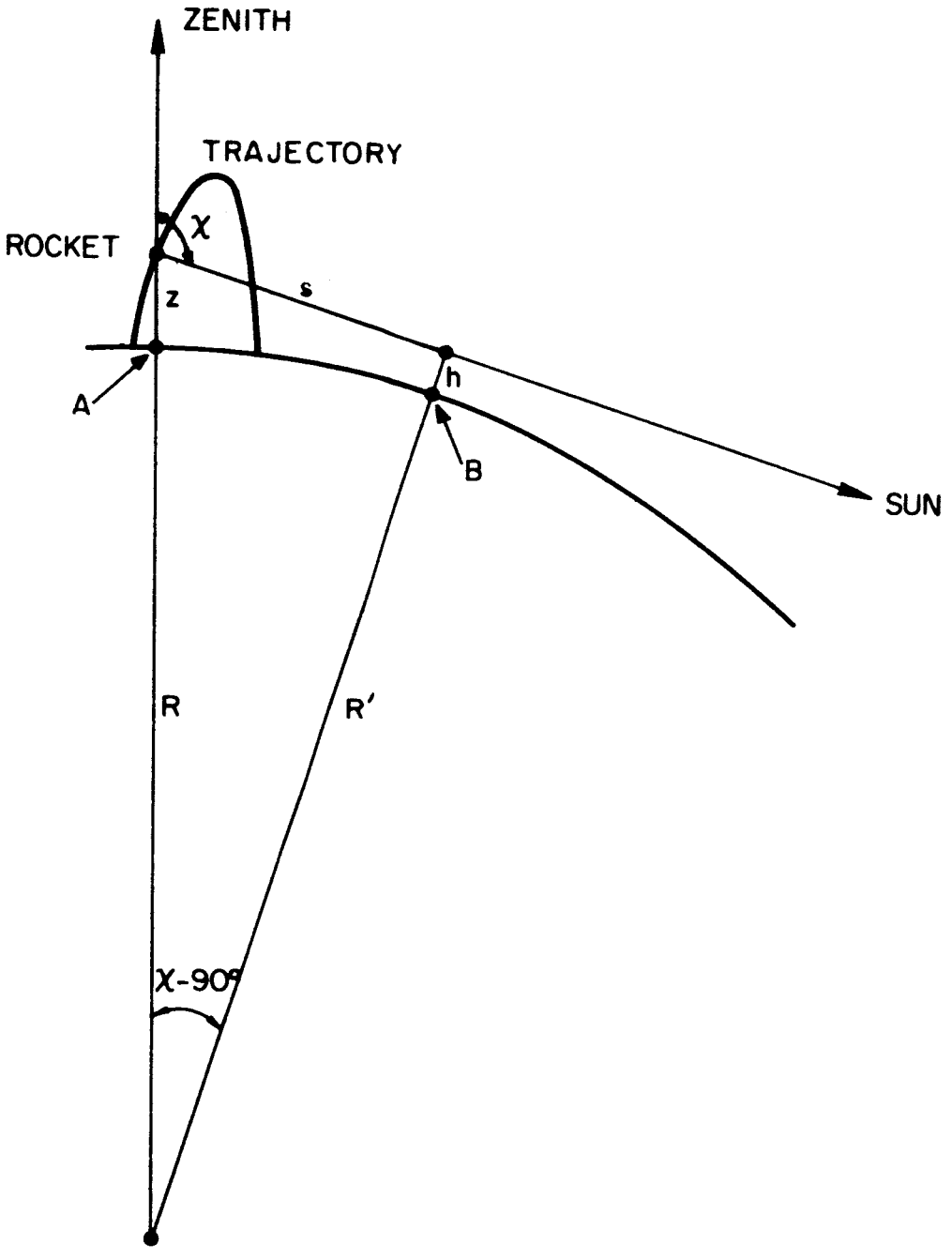

Figure 19. Geometry for uv measurements when $\chi > 90^{o}$.

Results

Lyman-α Measurements - Three rockets fired from the NASA Mobile Launch Facility (USNS Croatan) in the South Pacific provided molecular oxygen densities from Lyman-α measurements and are presented in Figure 20. On Nike Apache 14.228 flight, there was some difficulty with the data interpretation as meaningful results were obtained on only a portion of the ascent and descent trajectory. These data are not connected with a smooth curve as are the more reliable data from Nike Apache flights 14.231 and 14.232. For comparison, the smooth curve representing the results of an earlier measurement, Nike Apache 14.146 (summer, Wallops Island, $\chi = 85^{o}$) is also plotted. The smoothed curves for Nike Apaches 14.146 and 14.231 are accurate to within 5 percent, except near the upper and lower portions of the profiles where the errors approach 10 percent. The estimated accuracy of the smoothed curve for Nike Apache 14.232 is 5 percent less. If significant day-to-day variabilities may be ruled out, these data suggest a latitudinal effect with increasing densities at higher latitudes above 86 km. Above 79 km, the average scale height was 6.0 km for 14.231 and 8.8 km for 14.232.

Nike Apache flights 14.245 and 14.246 were flown at sunrise from Wallops Island in the summer two days apart. Since the solar zenith angle for Nike Apache 14.245 was 95^{o}, the densities are referred to a position above the earth where the measured solar radiation is nearest the earth, in this case at 40.3^{o}N, 4.7'W instead of the sub-rocket point at 37.8^{o}N, 5.0'W. For Nike Apache 14.246, the solar zenith angle was 85^{o} so that the data refers to conditions at 37.8^{o}N, 5.0'W (sub-rocket point) and is obtained at somewhat lower altitudes than for the former flight. The computed densities are given in Figure 21 and the smoothed curves are estimated to be accurate to 5 percent except near the ends of the profiles where the errors approach 10 percent. It is seen that the densities are less for Nike Apache 14.245 in the overlap region (91 to 96 km) by about 30 percent in density or by an altitude shift of 2 km.

It is not thought that this difference reflects day-to-day variabilities or atmospheric deviations between the two locations. Very similar results were obtained with Nike Apaches 14.145 ($\chi = 95^{o}$) and 14.146 ($\chi = 84^{o}$) flown on 15 July 1964 near sunrise. In that series, the reduction at $\chi = 95^{o}$ relative to $\chi = 85^{o}$ was also about 30 percent from 91 to 96 km, increasing to about 38 percent at 106 km. This shows that the difference between the densities obtained at $\chi < 90^{o}$ and $\chi > 90^{o}$ probably do not result from random errors related to accuracy of the data or rocket position. It is assumed in the analysis that the sun may be treated as a point source, and for the conditions of the measurement this is found to be a good assumption. The change in earth curvature is taken into account using Hayford's spheroid as the model. The source of a systematic error in the analysis that could account for this difference is not known.

It is believed that the difference between twilight and daytime results reflects a diurnal density variation at these altitudes. Our observations of a reduction of 28 to 38 percent from 89 to 106 km in density at twilight relative to daytime are in accord with data by Greenhow and Hall [12]. Based on meteor observations, they found larger densities in daytime with a diurnal

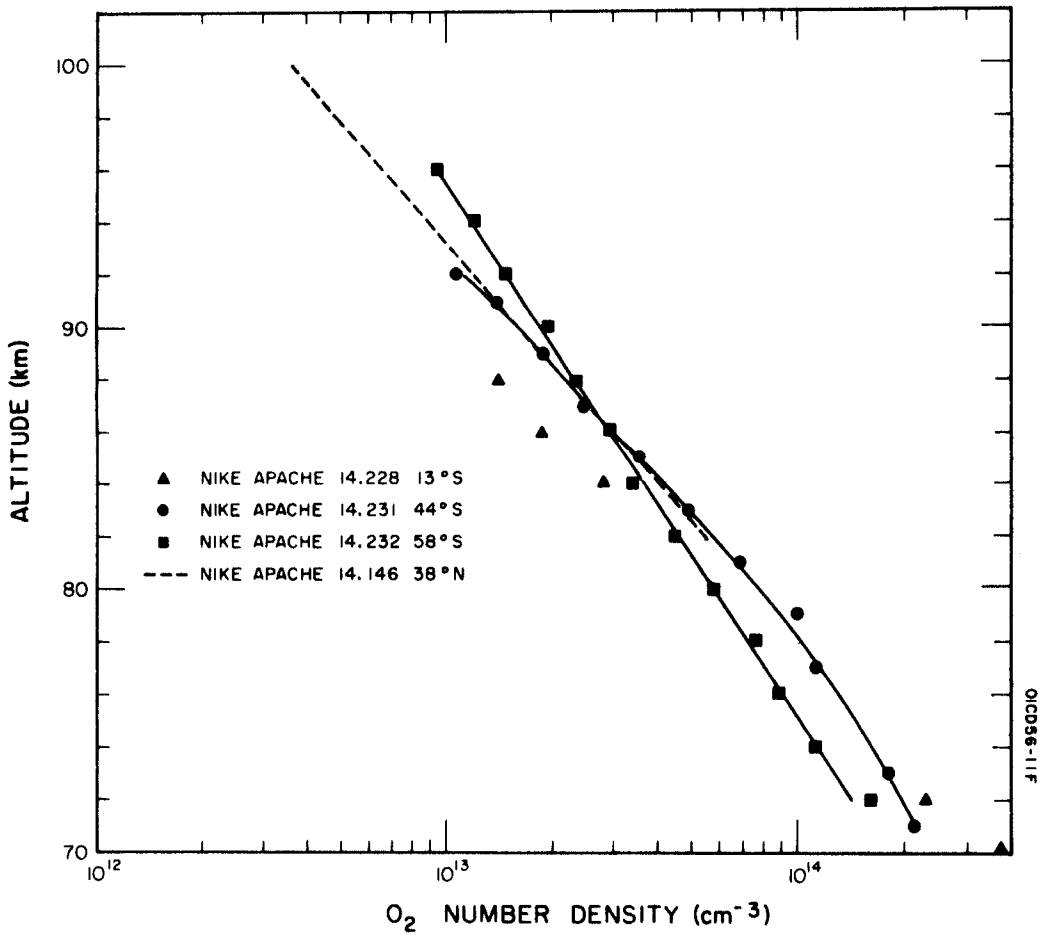

Figure 20. Molecular oxygen densities obtained from Lyman-α measurements in the South Pacific in Fall.

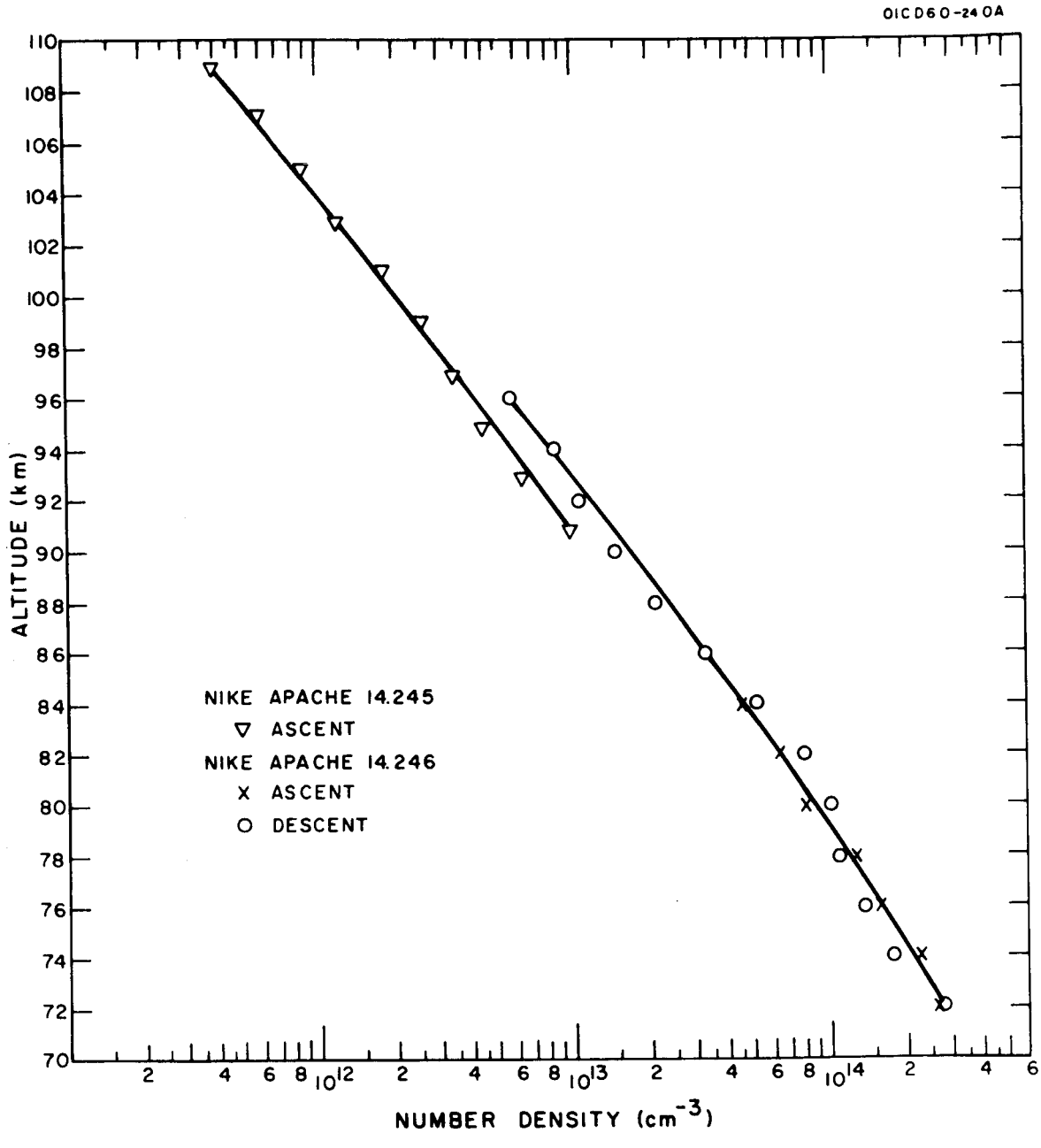

Figure 21. Molecular oxygen densities in summer from Lyman-α measurements at dawn and in the afternoon.

range of about 30 percent of the mean density at 96 km and a slightly increasing range with height from 85 to 105 km. Quiroz [13] has suggested that the daily maximum exceeds the nighttime minimum by a factor of 1.25 or 1.30. Much more data on diurnal variations is needed for this altitude range.

Molecular oxygen data in the fall from Nike Apache 14.244 are shown in Figure 22, and winter measurements from Nike Apache 14.247 are shown in Figure 23. Data from the descent trajectories are restricted to the higher portions of the profiles because of the unfavorable aspect angles at lower altitudes as the rocket tips over. In both of these profiles the accuracy of the smoothed curves is estimated to range from 5 percent to up to 10 percent near the end points. Data points are computed at every 1 km interval for the fall profile to show greater structural detail.

In the density profiles discussed above, Figures 20 to 23, the estimated errors actually represent the accuracy in the quantity $n\sigma$, as the cross section used may be in error by up to 25 percent. However, since this uncertainty is systematic and affects all the measurements equally, it has no bearing on the conclusions drawn from comparisons between various measurements.

The smoothed profiles representing the Lyman-α data obtained from the daytime Wallops Island flights, Nike Apaches 14.146/246/244/247, are plotted in Figure 24. All these measurements were made in the afternoon at zenith angles near 60°, with the exception of Nike Apache 14.146 (morning, $\chi \approx 84^{\circ}$). The two summer flights, about one year apart, indicate differences that may be due to day-to-day fluctuations or possibly diurnal effects. The differences between summer (14.246) and fall (14.244) in 1965 are most apparent below 81 km where the fall data shows lower densities. The cross-over region for the two profiles occurs at 85 km. Similar results were obtained by this technique in spring and summer measurements at Fort Churchill in 1957 and 1958 by Kupperian, et al. [14]. In those measurements, the summer data were also greater at lower altitudes, but the cross-over point occurred at 93 km instead of 85 km. The differences were also greater at lower altitudes, approaching a factor of two. The winter profile (14.247) shows densities significantly lower than the other seasons above about 78 km. From 80 to 88 km the winter densities are 25 to 30 percent less than the summer densities given by 14.246, in approximate agreement with the model of Cole and Kantor [15]. At lower altitudes, however, the winter densities are greater.

Other UV Measurements - Ion chambers sensitive to the spectral band 1225 to 1350Å were flown in Nike Apaches 14.245 and 14.246. Since the effective cross section for this band of radiation changes with altitude, the calibration curve of Figure 18 is used in the analysis. This curve is only approximate so the derived densities are not obtained with as high accuracy as those from the Lyman-α ion chamber. Accordingly, for Nike Apache 14.245, this molecular oxygen density profile was adjusted to fit the results of the Lyman-α measurement at lower altitudes. The adjustment was made in the constant value used for the optical depth factor, and the results are plotted in Figure 25. The data match shown in the figure is not completely adequate because of the small difference in the slopes of the two profiles at 111 km; however, in this region the accuracy

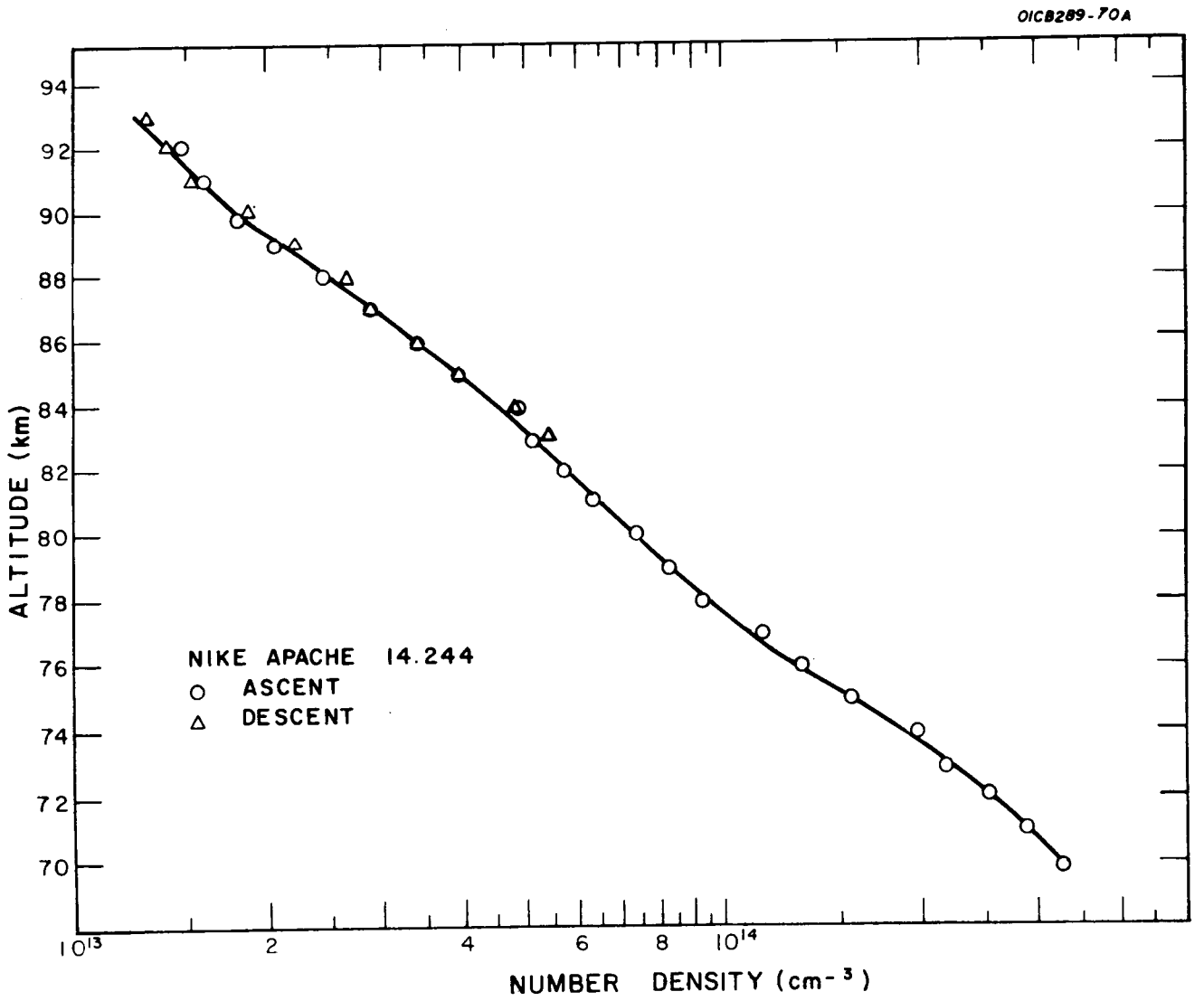

Figure 22. Molecular oxygen densities in Fall from Lyman-α measurements.

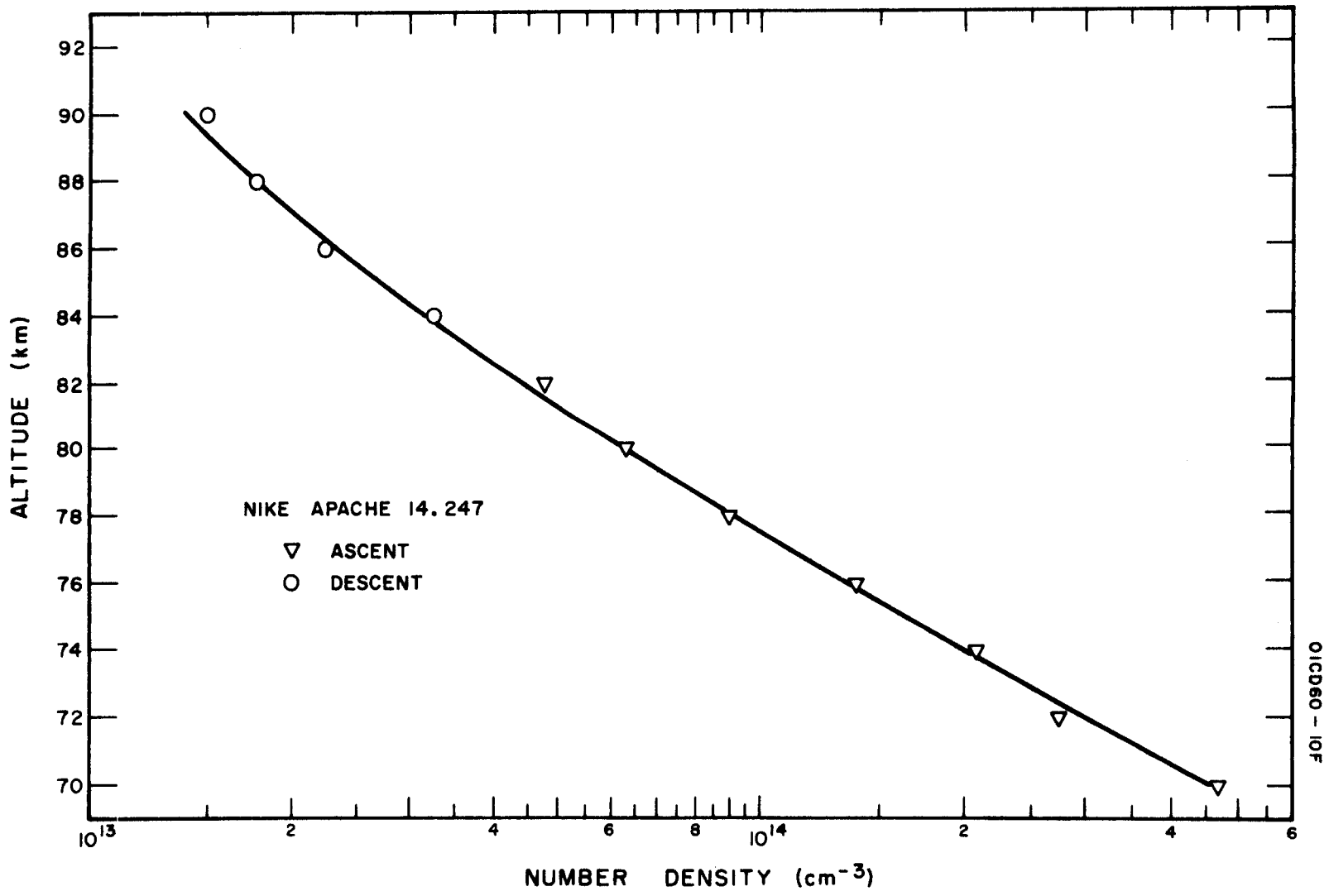

Figure 23. Molecular oxygen densities in Winter from Lyman-α measurements.

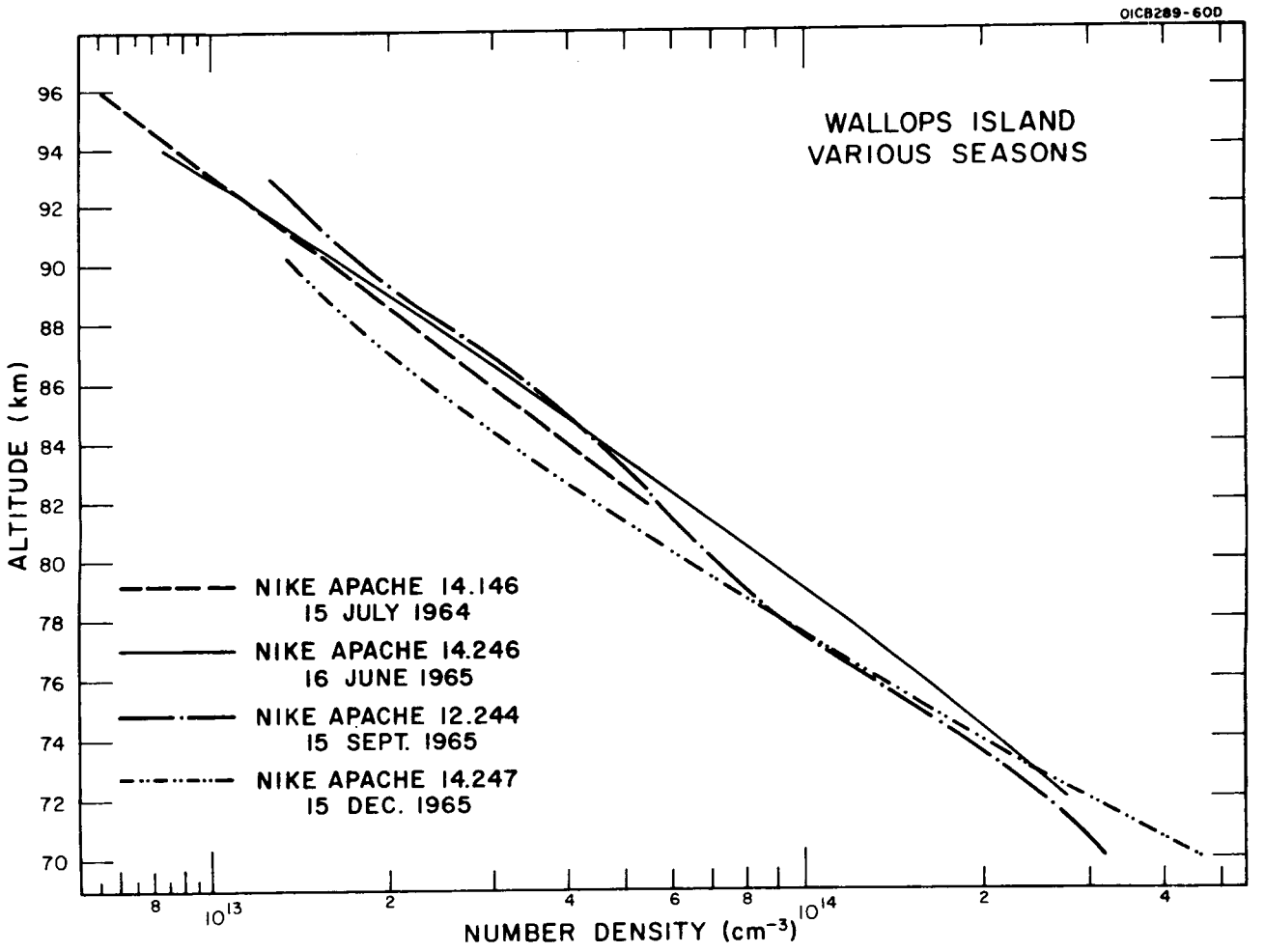

Figure 24. Molecular oxygen densities above Wallops Island from Lyman-α measurements at various seasons.

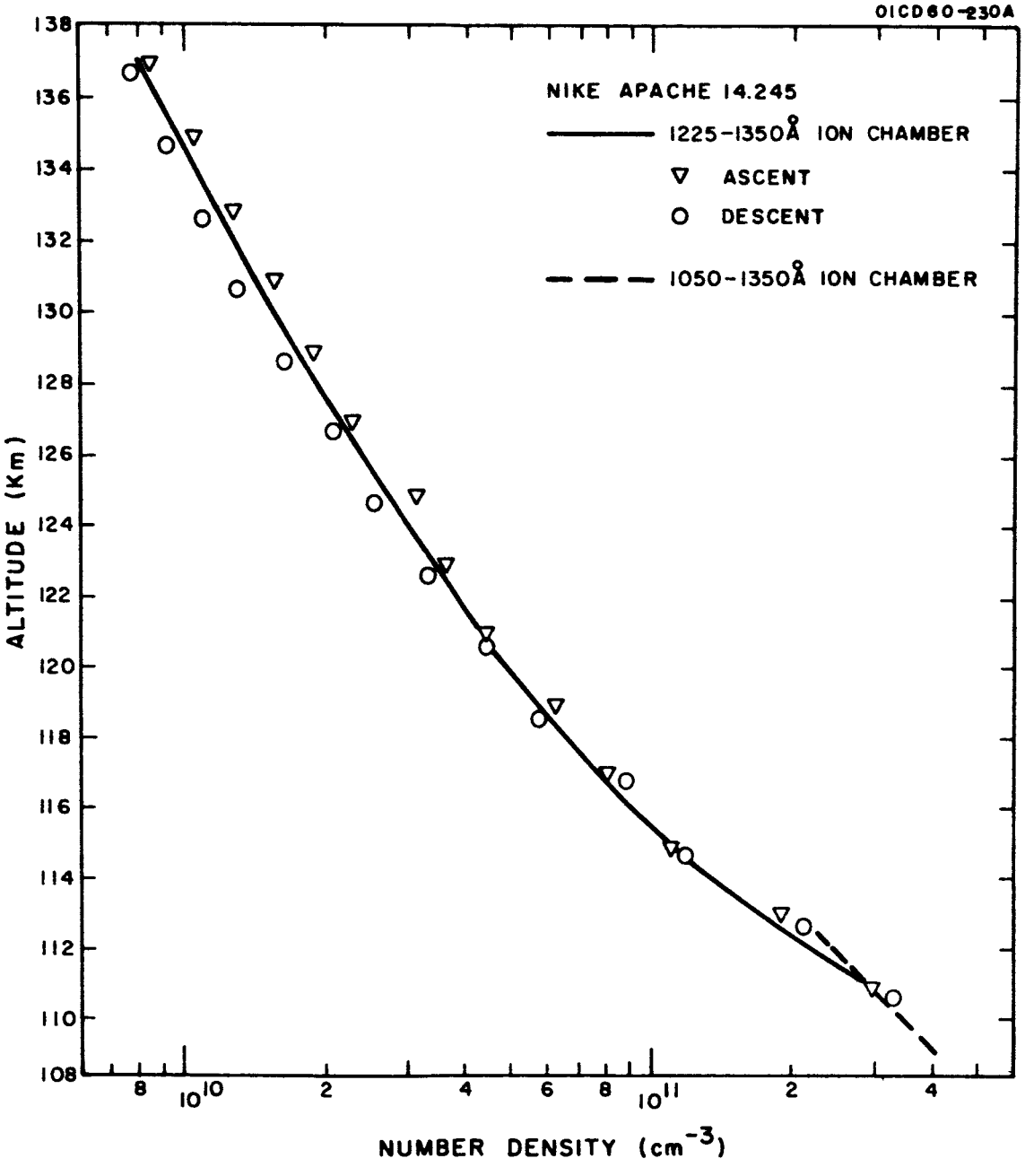

Figure 25. Molecular oxygen densities from 1300Å ion chamber measurements on Nike Apache 14.245.

in the slope (or scale height) is not high for the higher altitude profile. The results for Nike Apache 14.246 are shown in Figure 26, which also shows the Lyman-α profile. The ascent data fits well with the Lyman-α measurements and no adjustment was required as in the previous flight. The smoothed descent data is illustrated by the dashed curve in the figure, and since it does not match the Lyman-α results at the lower altitudes, it is not considered reliable.

Data from the 1225 to 1350Å ion chambers are also used to correct the Lyman-α ion chamber data. The bandpass of 1050 to 1350Å for this ion chamber introduces some error in the estimated Lyman-α attenuation profile, beginning at about 1-1/2 to 2 scale heights above and below unit optical depth for Lyman-α. The specific band 1225 to 1350Å is absorbed more strongly than Lyman-α and therefore causes an ion chamber current increase at altitudes above any change in the Lyman-α profile. These corrections have been made in the results for these flights; however, the data is not extended to altitudes requiring a correction of more than 10 percent. Neglecting this correction in the other flights has not resulted in significant errors in the results or affected the conclusions presented here. The analysis of the 1225 to 1350Å ion chamber data has shown that this measurement has more limited usefulness because of the reduced accuracy in the final density values.

On Nike Apache flight 14.231, a BaF_2 window - p-xylene gas ion chamber provided molecular oxygen data from 116 to 140 km. Here again the effective cross section changes with altitude so the calculated densities in Figure 27 are based on the appropriate calibration curve of Figure 18. The difference between the ascent and descent data results from about a 20 percent difference in current levels. The smooth curve through the average data is taken to be the best estimate of the molecular oxygen profile and has an uncertainty of about 20 percent.

The molecular oxygen densities obtained in Nike Apache flight 14.244 with the 1425 to 1480Å photometer have provided the most accurate supplementary data to the Lyman-α ion chamber data. The results are plotted in Figure 28, where the dotted curve denotes the results from the ascent trajectory where it differs appreciably from descent. This calculated rise in density above 128 km on ascent is believed to be associated with effects other than the ambient density, such as sensitivity changes of the photometer or possibly a rocket outgassing effect. Both effects are expected to be less significant during descent. The ascent data above 128 km is considered unreliable and is therefore discarded in the molecular oxygen profile designated by the solid line. The estimated accuracy of this profile is 10 percent.

Figure 29 shows the results from Nike Apache 14.231 and 14.244 and some other high altitude photometer measurements of molecular oxygen. All the data, except for flight 14.231, refer to photometers with the bandpass 1425 to 1480Å. Excellent agreement between the Nike Apache 14.244 profile and the 1953 data of Friedman [4] is obtained for the range 114 to 130 km.

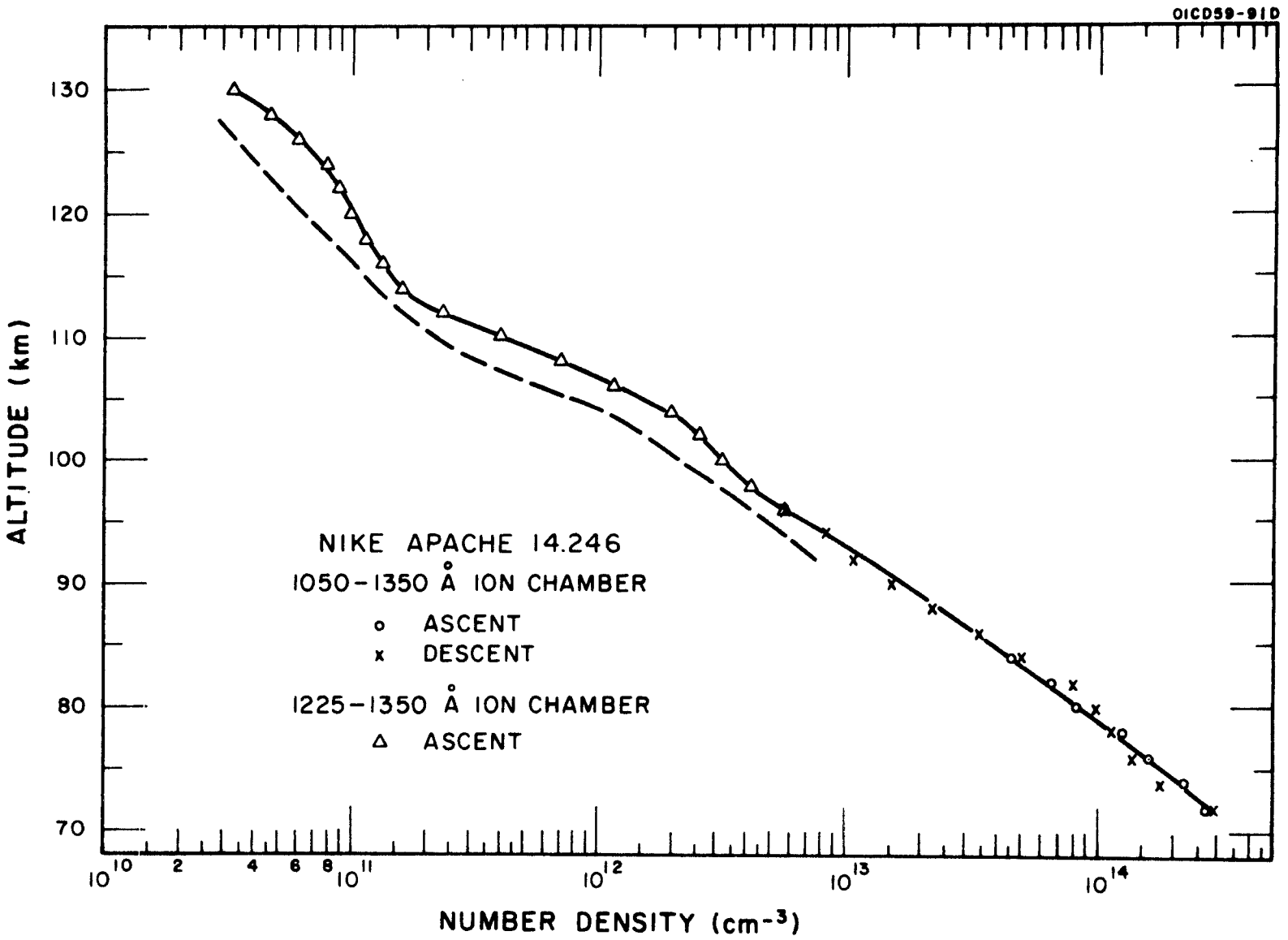

Figure 26. Molecular oxygen densities from 1300Å and Lyman-α ion chamber measurements on Nike Apache 14.246 (The dashed curve represents descent data for the 1300Å ion chamber and is considered less reliable than the ascent data.)

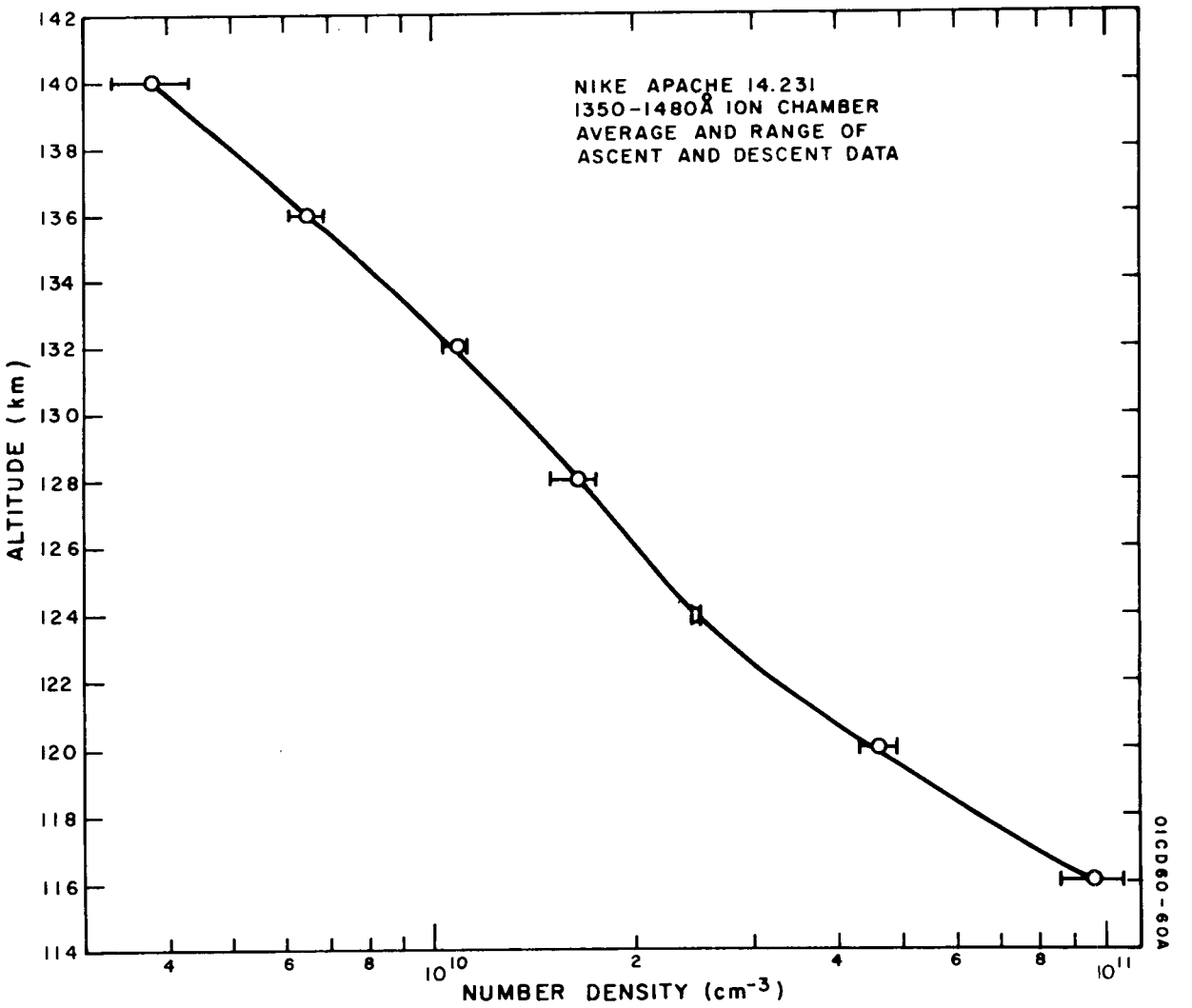

Figure 27. Molecular oxygen densities from 1450Å ion chamber measurements on Nike Apache 14.231.

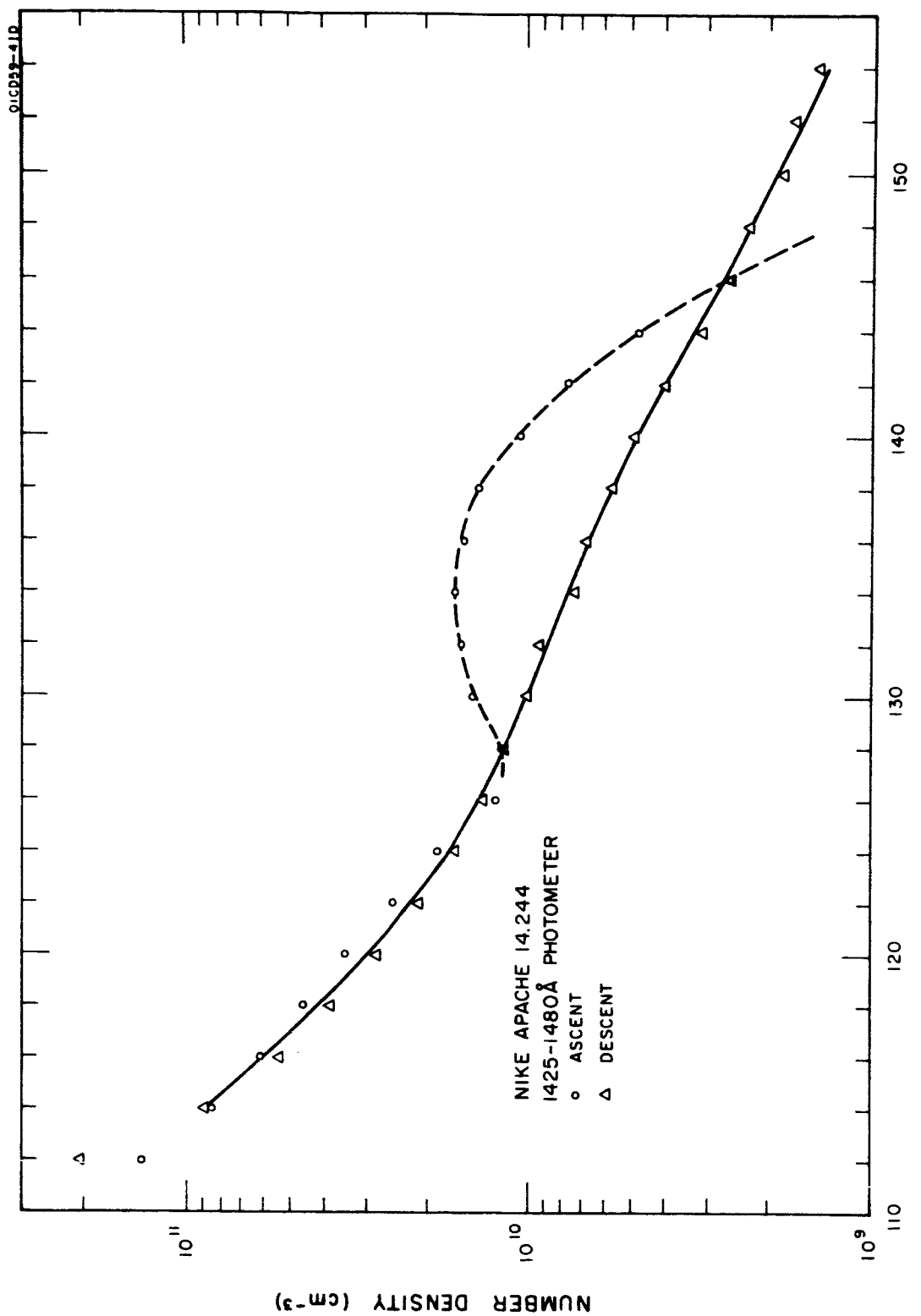

Figure 28. Molecular oxygen densities from 1450Å photometer measurements on Nike Apache 14.244 (The dashed curve representing ascent data above 125 km is not considered to be indicative of the actual density).

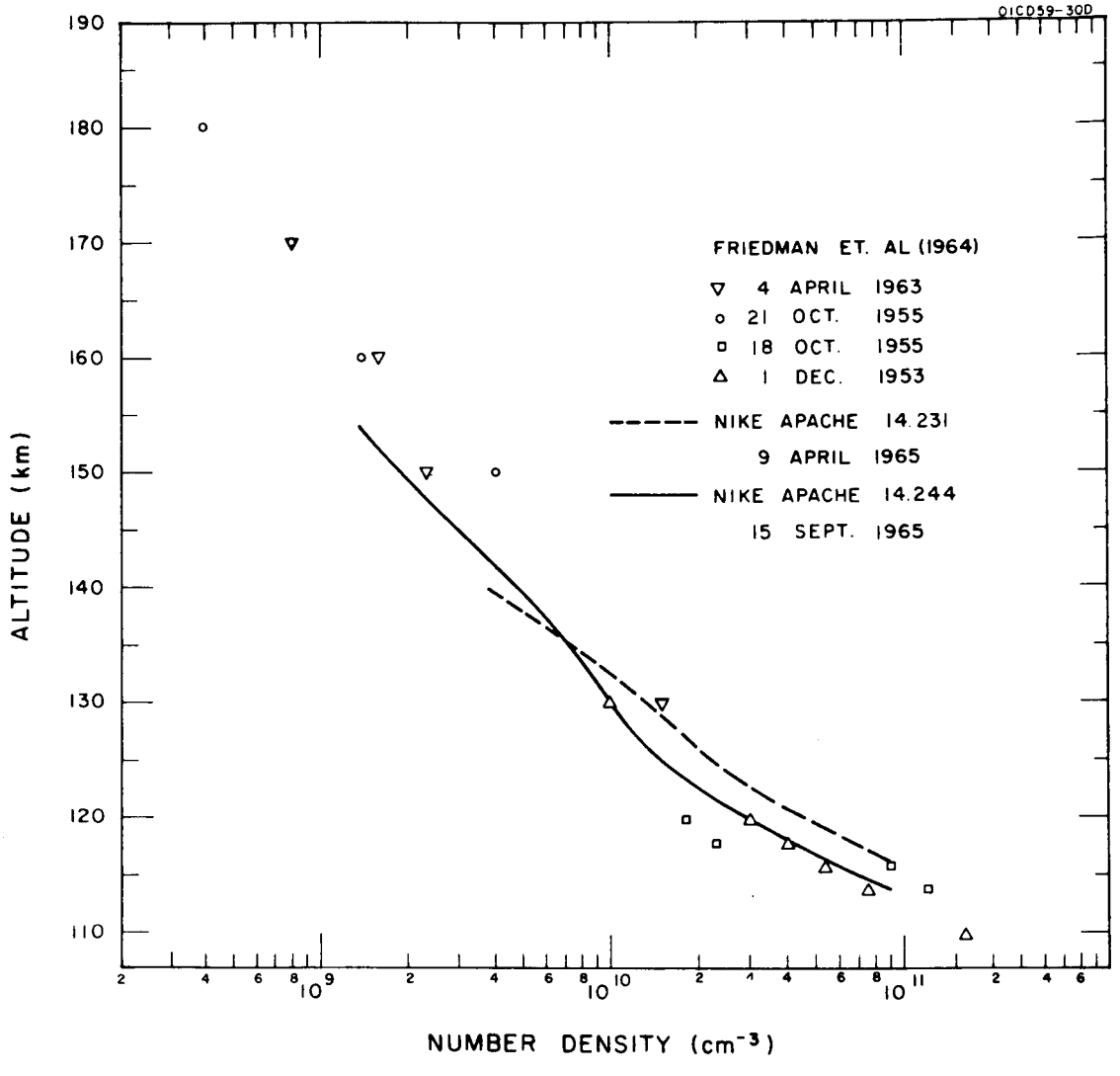

Figure 29. Molecular oxygen densities obtained from 1450Å photometers.

REFERENCES

1. Smith, L. G., Weeks, L. H., and McKinnon, P. J.: "Investigation of the D and E Regions of the Ionosphere During the International Quiet Sun Year," GCA Corporation, Technical Report No. 65-21-N (1965), NASA CR-391 (1966).

2. Smith, L. G., and Weeks, L. H.: "Molecular Oxygen Densities from Rocket Measurements of Lyman-α Absorption Profiles," GCA Corporation, Technical Report No. 65-10-N (1965), NASA CR-392 (1966).

3. Smith, L. G.: "A Simple Method of Trajectory Determination for Sounding Rockets," NASA Contract No. NASw-489, GCA Corporation, Technical Report No. 63-9-N (1963).

4. Friedman, H., Chubb, T. A., and Siomkajlo, J. M.: A Manual on Molecular Oxygen Determination for the IQSY, IQSY Instruction Manual No. 9, p. 95, (November 1964), IQSY Secretariat, 6 Cornwall Terrace, London NW 1.

5. Bowhill, S. A., and Smith, L. G.: Rocket Observations of the Lowest Ionosphere at Sunrise and Sunset, Space Research VI, North Holland (1965).

6. Smith, L. G., "Rocket Observations of Sporadic E and Related Features of the E Region," Radio Science 1, No. 2, 178-196 (1966).

7. Spencer, N. W., et al., "Electron and Molecular Nitrogen Temperature in the Thermosphere," J. Geophys. Res. 70, 2665-2698 (1965).

8. Thomas, L., Venables, F. H., and Williams, K. M.: "Measurements of Solar X-Ray Fluxes by the U. S. Naval Research Laboratory Satellite 1964-01-D," Plant. Space Sci. 13, 807-822 (1965).

9. Schultz, E. D. and Holland, A. C., "The Solar Flux Incident at the Top of the Atmospheres of Earth and Neighboring Planets for the Spectral Region 50Å to 3000Å," GCA Corporation, Technical Report No. 62-14-N (1962).

10. Watanabe, K., Zelikoff, M., and Inn, E. C. Y.: AFCRC-TR-53-23, Geophys. Res. Paper No. 21 (1963).

11. Watanabe, K., and Marmo, F. F., J. Chem. Phys. 25, 965 (1956).

12. Greenhow, J. S. and Hall, J. E., "Diurnal Variations of Density and Scale Height in the Upper Atmosphere," J. Atmos. Terr. Phys. 18, 203-214 (1960).

13. Quiroz, R. S., private communication.

14. Kupperian, J. E., Jr., Byram, E. T., and Friedman, H.; "Molecular Oxygen Densities in the Mesosphere at Fort Churchill," J. Atmos. Terr. Phys. 16, 174-178 (1959).

15. Cole, A. E., and Kantor, A. J., "Air Force Interim Supplemental Atmospheres to 90 Kilometers," Air Force Surveys in Geophysics No. 153, AFCRL-TR-63-936 (Dec. 1963).

APPENDIX A

THE E-REGION AT SUNRISE: IONIZATION BY LYMAN-α*

INTRODUCTION

The sequential illumination of the ionosphere at sunrise by the different regions of the solar spectrum provides a valuable method of determining the role of these separate wavelengths in the formation of the ionospheric layers. In an earlier paper, Bowhill and Smith [A-1] applied this method to the process of photodetachment in the D region. In the present paper, it is applied to the initial ionization of the upper E region. It will be shown that the first significant ionization is caused by Lyman-α radiation and that values of nitric oxide concentration are obtained in the altitude range 130 to 150 km in good agreement with theoretical values computed by Barth. [A-2]

OBSERVATIONS

The analysis is based mainly on the data from a single rocket flight: Nike Apache 14.145 launched at Wallops Island on the morning of 15 July 1964 at a solar zenith angle of 96^{o}. This rocket was part of a sequence of three; the other two in the sequence were launched at zenith angles of 108^{o} and 85^{o}.

The electron density profile in the E region obtained from the first of the series is shown in Figure A-1. The trajectory of the rocket was completely within the earth's shadow. The profile was obtained from a dc probe using the insulated nose tip of the rocket as the electrode. [A-3] The factor of proportionality between probe current (measured at +2.7 volt) and electron density has been established by comparison with a CW propagation experiment carried on the same rocket [A-4]. This payload, but not the subsequent rockets of the series, was also instrumented with an RF probe of the capacitance type, which confirms the very low electron density indicated by the dc probe in the upper part of the trajectory. The profile shows Sporadic E layers at 95 and 119 km, and a possible additional layer at 113.5 km, seen only on the descent profile.

The next profile obtained from the rocket launched 1 hour 20 minutes later is shown in Figure A-2. Some change in height of the Sporadic E layers can be noted, the upper layer is now at 114 km and the lower layer at 93 km. A relatively large increase in electron density has occurred above 120 km. There has also been an increase in electron density in the flight the ascent and descent data had generally been in agreement, this

---

*A version of this Appendix was presented by L. G. Smith at the COSPAR Meeting, Vienna, May 1966.

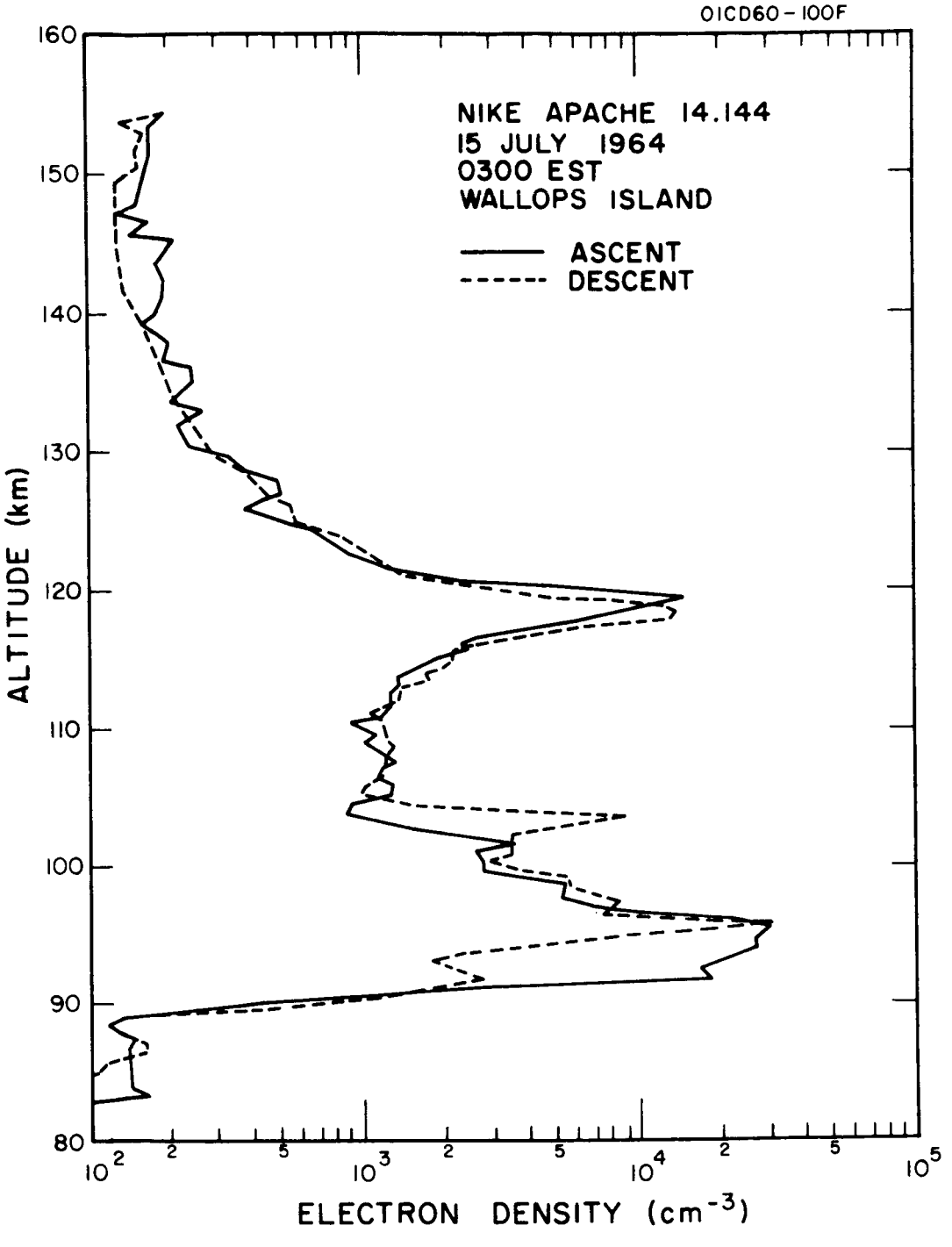

Figure A-1. Electron density profile, Nike Apache 14.144.

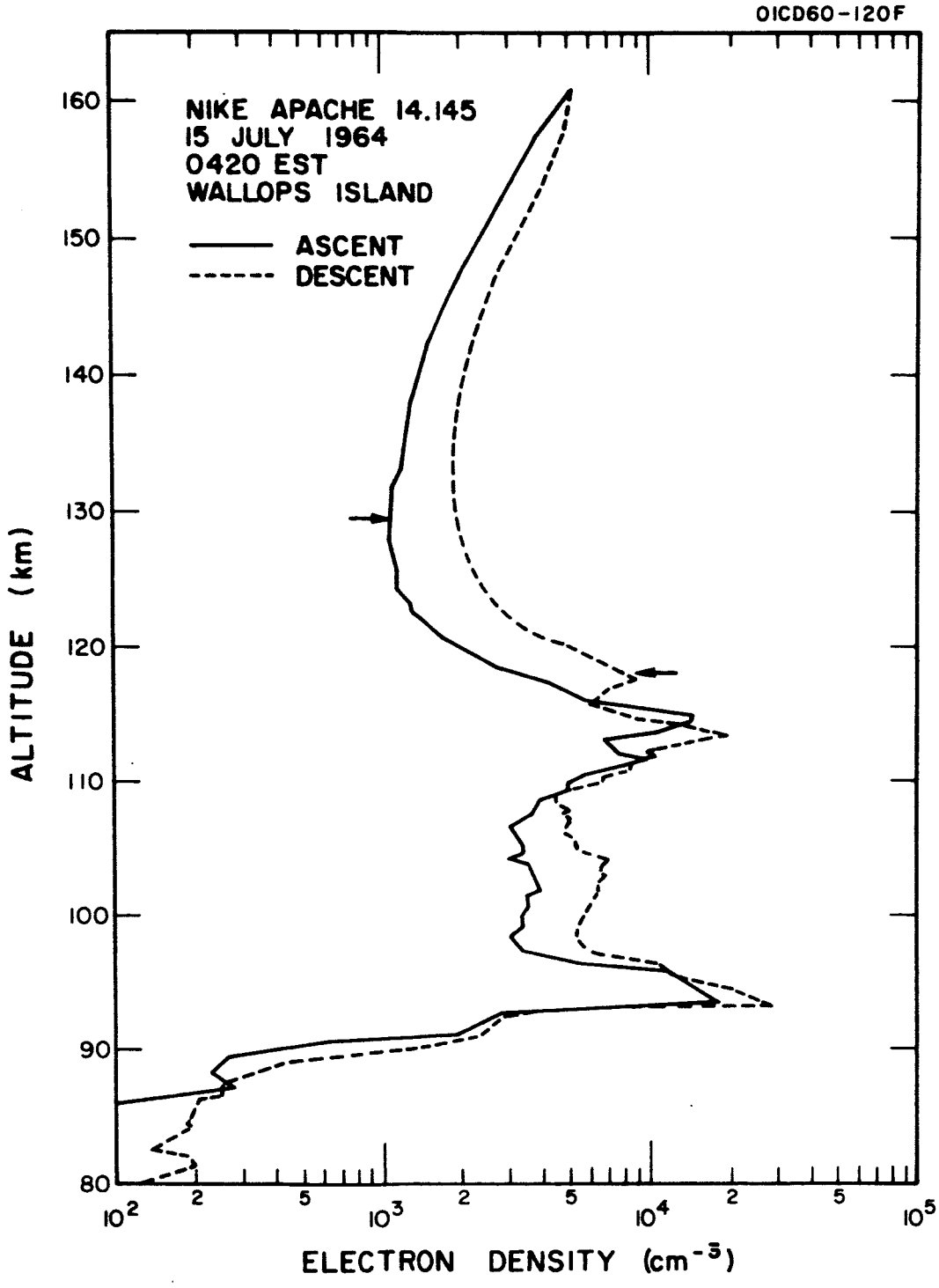

Figure A-2. Electron density profile, Nike Apache 14.145. Arrows point to unit optical depth for Lyman-α.

flight shows, except for the Es layers, a significantly greater electron density in the descent profile than in the ascent profile.

This payload carried a narrow-band ion chamber sensitive to Lyman-α radiation. The points on the profiles at which unit optical depth was observed (i.e., a flux equal to 37 percent of the incident flux) are indicated by small arrows, at 129.5 km on ascent and at 118 km on descent.

A calculation, to be given later, shows that the solar radiation which forms the daytime E layer is not affecting the region below 150 km at this time. Thus, in addition to Lyman-α the only radiation illuminating the region consists of wavelengths greater than about 1800Å and visible parts of the solar spectrum. These are not capable of directly ionizing any known constituent of the upper E region, although they may be acting as a source of electrons by ionization or by photodetachment in the region below 120 km.

LYMAN-α RADIATION

The observed Lyman-α absorption profile shown in Figure A-3 is expressed in terms of the minimum ray height, i.e., the distance of closest approach of the ray to the earth's surface. The molecular oxygen density profile may be obtained from these data and has been given elsewhere. [A-5] Conversely, a similar absorption profile can be computed for a model atmosphere as will be done later in connection with discussion of E-layer radiation. The incident energy flux of Lyman-α was observed on this flight to be 3.3 erg cm^{-2} sec^{-1}, corresponding to a photon flux of 2.0×10^{11} cm^{-2} sec^{-1}.

The Lyman-α flux, as a percentage of incident flux, is calculated for altitudes between 125 and 160 km, as a function of zenith angle using the relation:

(Minimum Ray Height) = (Rocket Altitude) - (Earth Shadow Height)

The results of this calculation are shown in Figure A-4 for zenith angles between 99° and 93°. The calculation is stopped at X=93°, as it is no longer possible to assume, as has been implied in the formula, that the rocket is above the absorbing layer of the atmosphere. At the time of the rocket flight the solar zenith angle was changing at the rate of 1 degree in 354 seconds. The graph also indicates unit optical depth (37 percent) and an effective onset (55 percent) for Lyman-α radiation, which will be explained later.

Neglecting loss processes, the electron density produced by ionization by Lyman-α will be proportional to the integrated flux of Lyman-α, the constant of proportionality giving the concentration of the constituent being ionized.

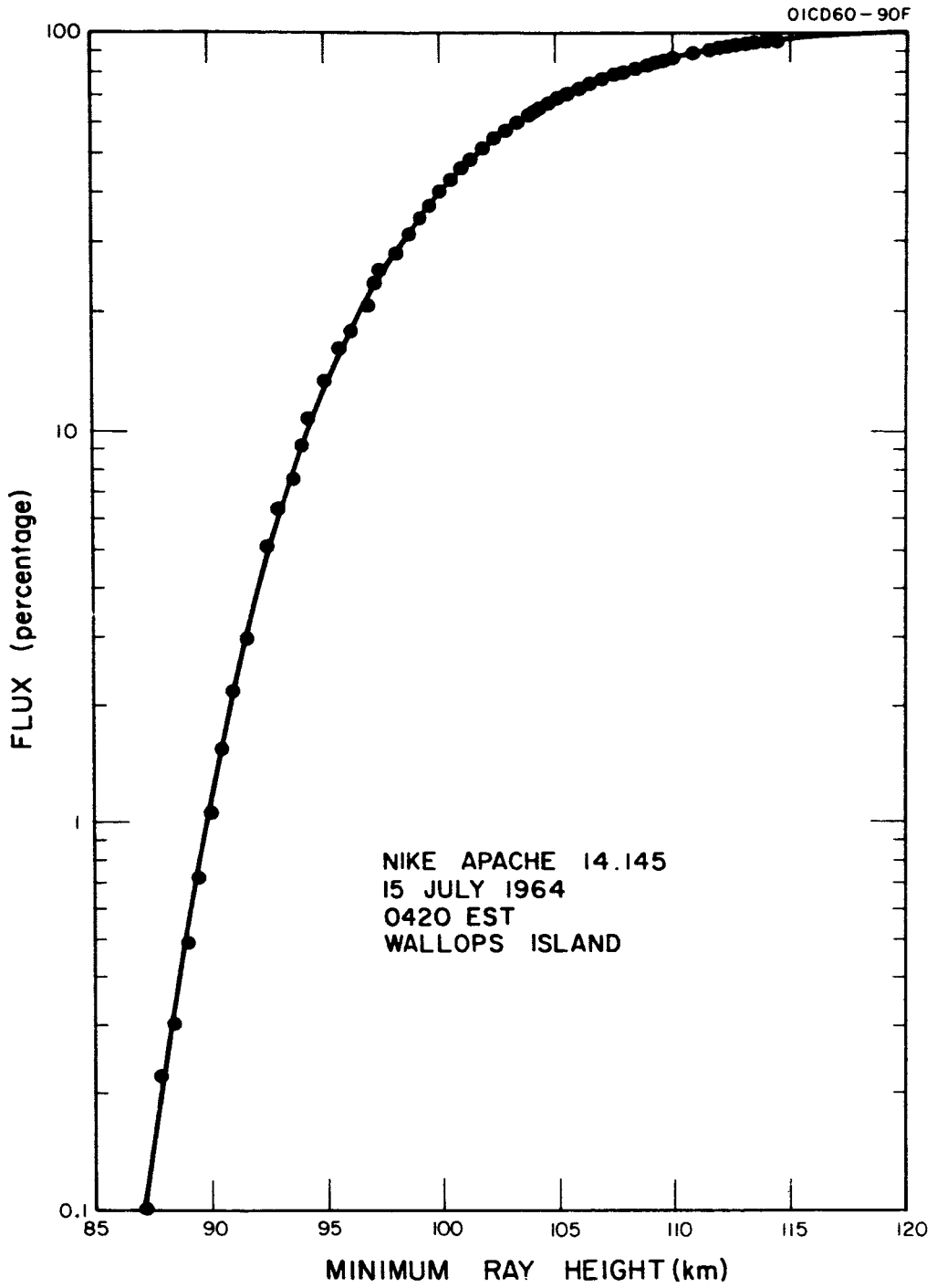

Figure A-3. Observed Lyman-α absorption profile.

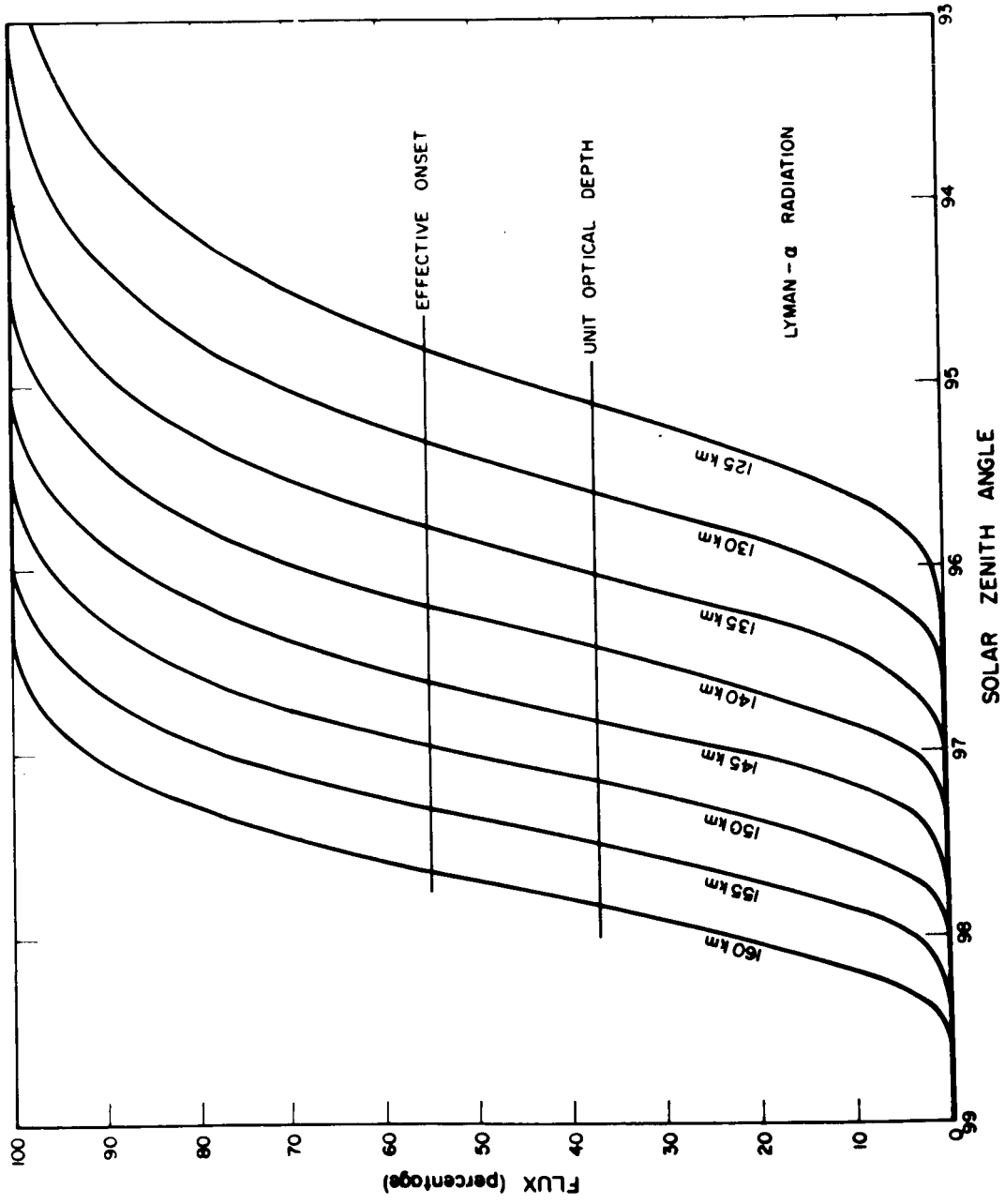

Figure A-4. Lyman-α flux vs zenith angle for altitudes between 125 and 160 km.

The integrated flux obtained from the flux curves is shown in Figure A-5. The unit of integrated flux is equal to the unattenuated Lyman-α flux acting for a change of zenith angle of 1×10^{-3} degrees. The trajectory of Nike Apache 14.145 is indicated by the dashed line on the graph. The solar zenith angles computed for the actual position of the rocket are given in Table A-1.

Table A-1: Solar Zenith Angle at Rocket, Nike Apache 14.145

Altitude	Ascent	Descent
120 km	95.56°	94.35°
125	95.52	94.39
130	95.48	94.43
135	95.44	94.48
140	95.39	94.53
145	95.33	94.59
150	95.27	94.65
155	95.19	94.73
160	95.05	94.88
161 (Apogee)	94.96	94.96

The observed electron density is plotted against integrated Lyman-α flux in Figure A-6. On this plot, at a given altitude, the points should lie on a straight line from an initial (background) value of electron density. Conversely, lines joining the pairs of values (ascent and descent) at a given altitude when extrapolated back to zero integrated flux indicate an initial value of electron density which should have been observed on a flight prior to Lyman-α illuminating the region. Except for the data at 150 km and above, the values obtained by this extrapolation are larger than were actually observed in the preceding flight (Nike Apache 14.144) and shown in Figure A-1. In view of the obvious change in altitude and shape of

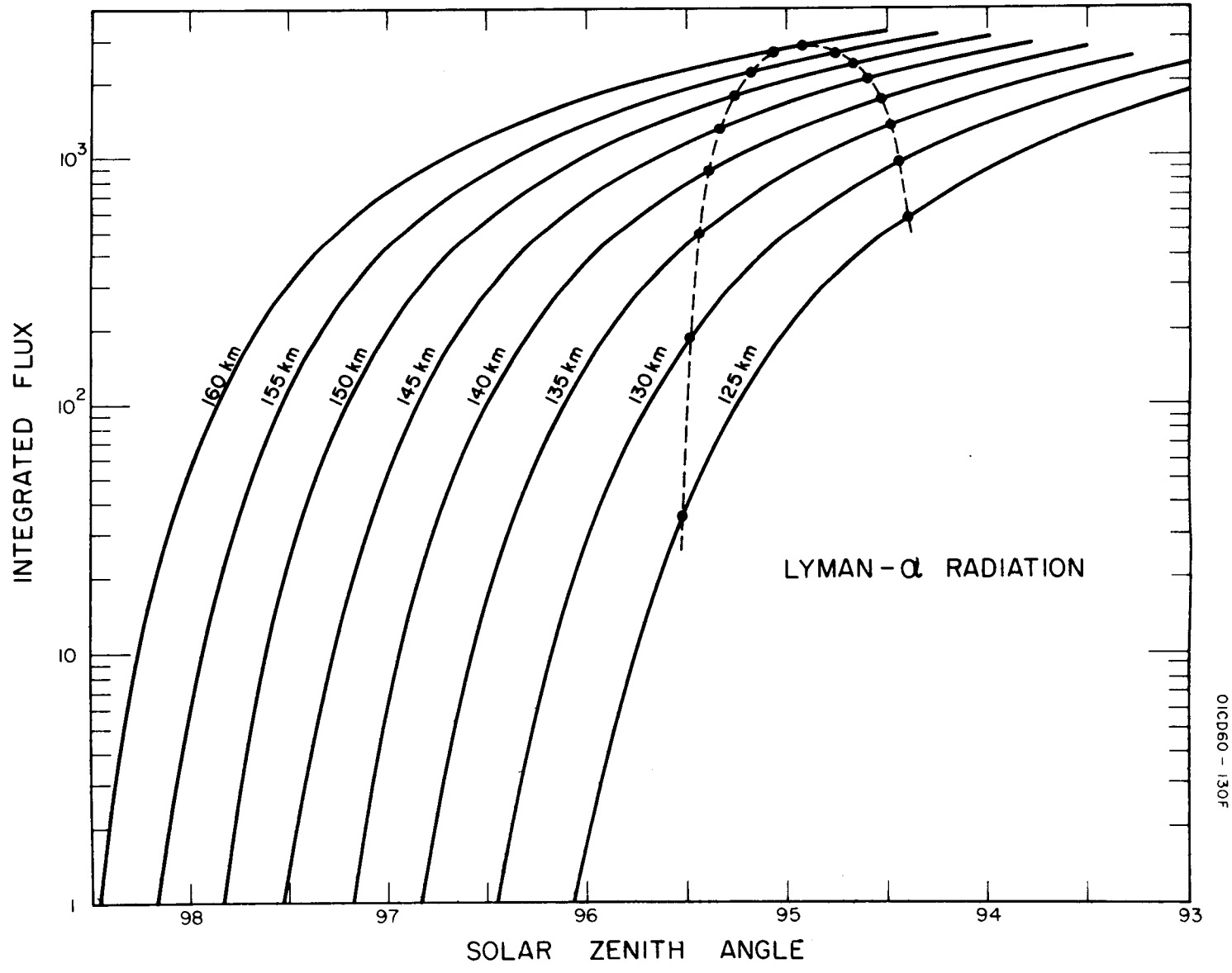

Figure A-5. Integrated Lyman-α flux. The dashed line indicated the trajectory of Nike Apache 14.145.

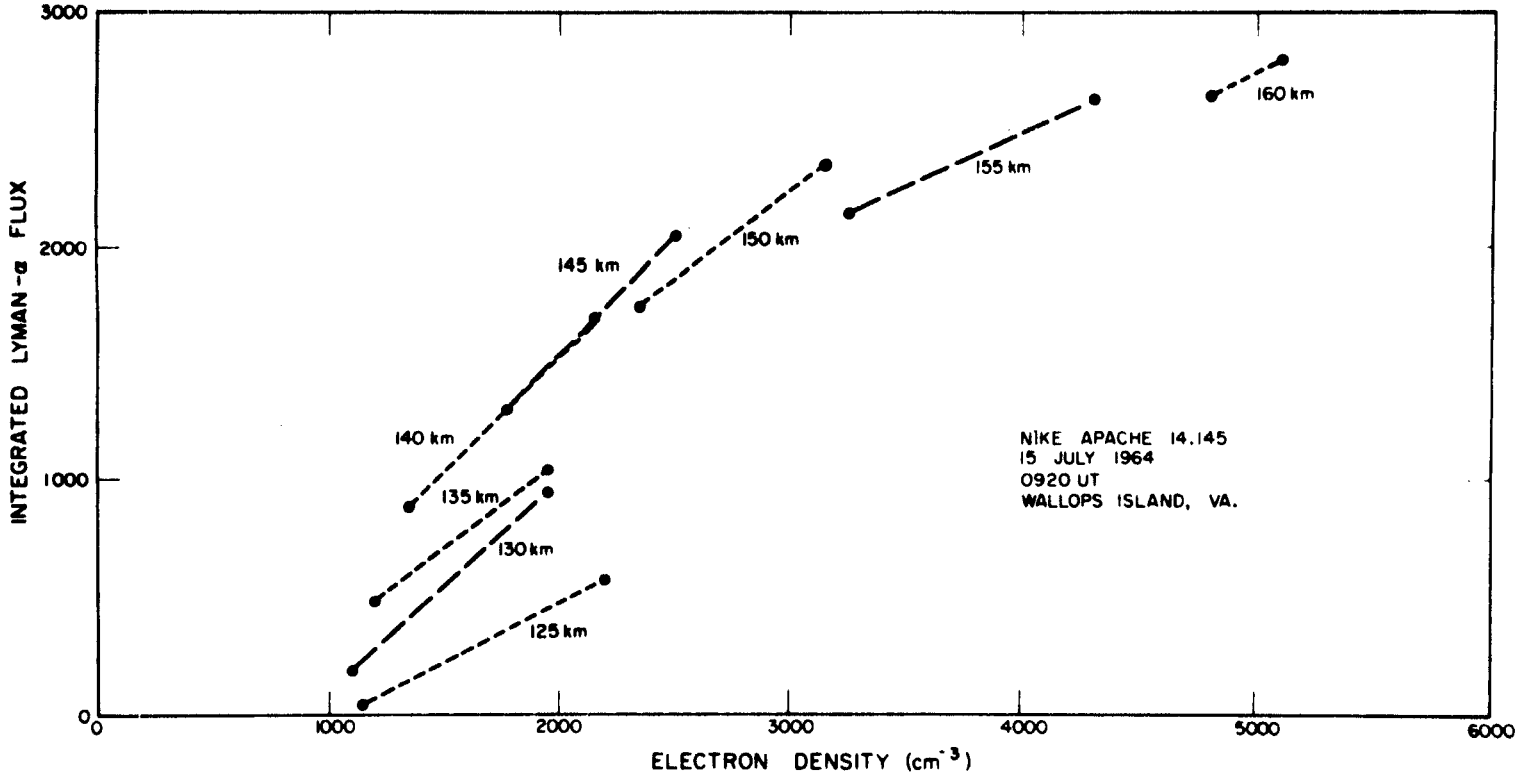

Figure A-6. Electron density vs integrated Lyman-α flux.

the upper Sporadic E layer, it is assumed that the background values had increased between the two rocket flights. It is also thought that a difference in background values at the 125 km level makes that data unreliable; the horizontal separation of the penetration of the upper Es layer was about 100 km.

NITRIC OXIDE

Assuming that nitric oxide is the most likely constituent at these altitudes that can be ionized by Lyman-α, the concentration may be deduced. The ionization cross section of nitric oxide is taken to be 2.0×10^{-18} cm^2. Values given in Figure A-7 show that the concentration of nitric oxide is $(8 \pm 1) \times 10^6$ cm^{-3} from 130 to 150 km. Higher values, not shown in the figure, are indicated at 155 and 160 km, but it will be shown later that these are probably due to contamination by E-layer radiation. The figure also includes theoretical values computed by Barth [A-2]. The observed values are seen to be in good agreement. Experimental values by Barth[A-6] are also shown. These are obtained from observations of the day airglow.

This concentration gives an ionization rate of 3.2 cm^{-3} sec^{-1} for unattenuated Lyman-α radiation. Electron density profiles have been computed using this value for zenith angles from 98° to 94°. These are shown in Figure A-8. The profile from Nike Apache 14.144 is used as the initial value of electron density, loss by recombination is assumed negligible, and ionization by E-layer radiation is not included.

E-LAYER RADIATION

Following the illumination of region Lyman-α comes the radiation which ultimately forms the daytime E layer. This comprises X-rays between 10 and 100Å and uv between about 900 and 1600Å. The spectral composition and absorption cross sections for these radiation are not known well enough to justify an exact calculation. Accordingly, model has been taken so as to give unit optical depth at 105 km, corresponding to the peak of the E-layer at $\chi = 0°$. This is equivalent to taking an effect absorption cross of 3.1×10^{-19} cm^{-2} with respect to the total density given in the U.S. Standard Atmosphere 1962[A-7].

Using this value of cross section and total columnar densities derived from the U.S. Standard Atmosphere 1962 given in Figure A-9, an absorption profile has been computed, in terms of minimum ray height, for complete traversal of the atmosphere. This is shown in Figure A-10. Note that unit optical depth for this E-layer radiation occurs at a minimum ray height of 159 km. The model is valid only below this altitude of unit optical depth.

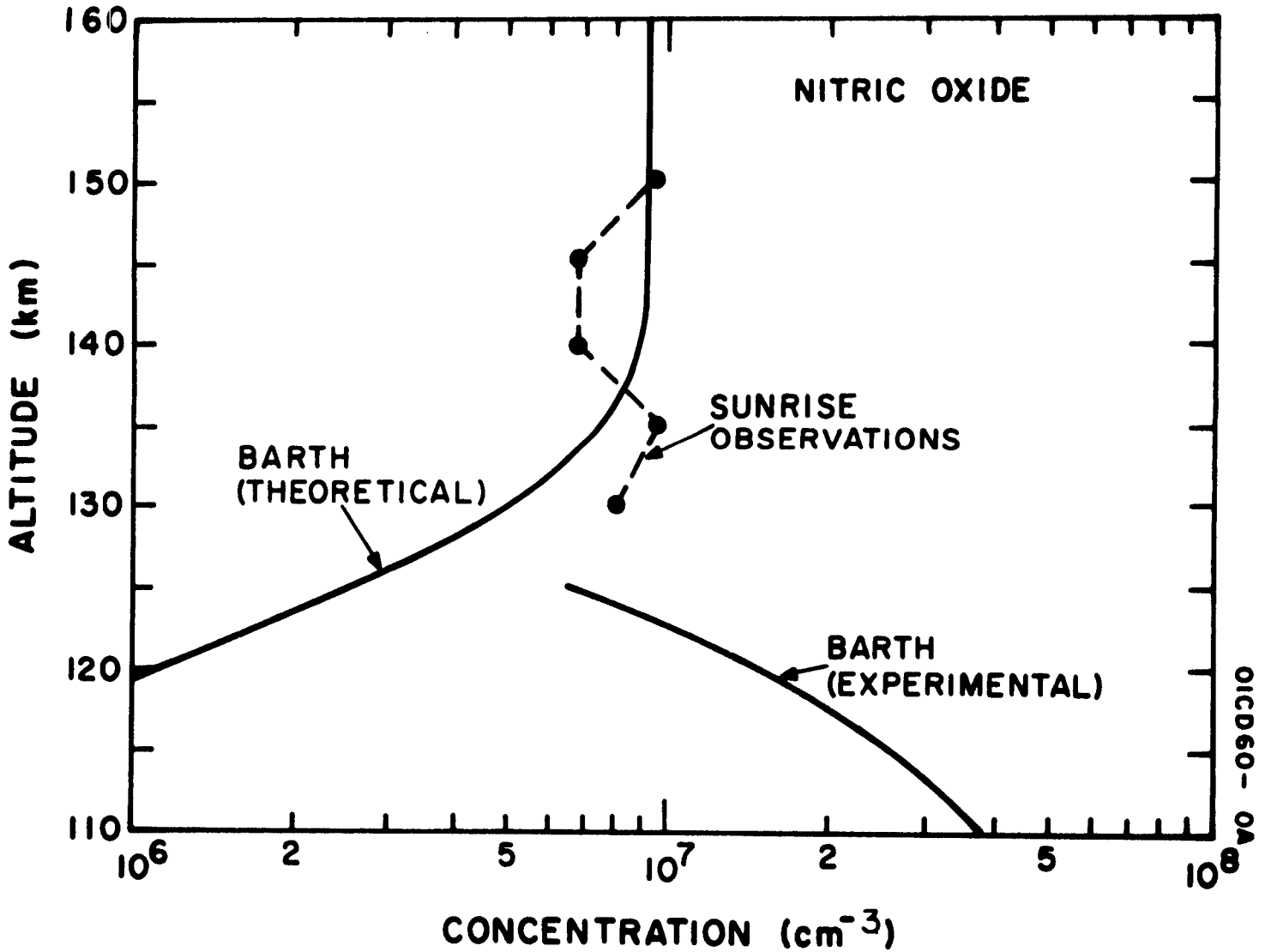

Figure A-7. Nitric oxide concentration.

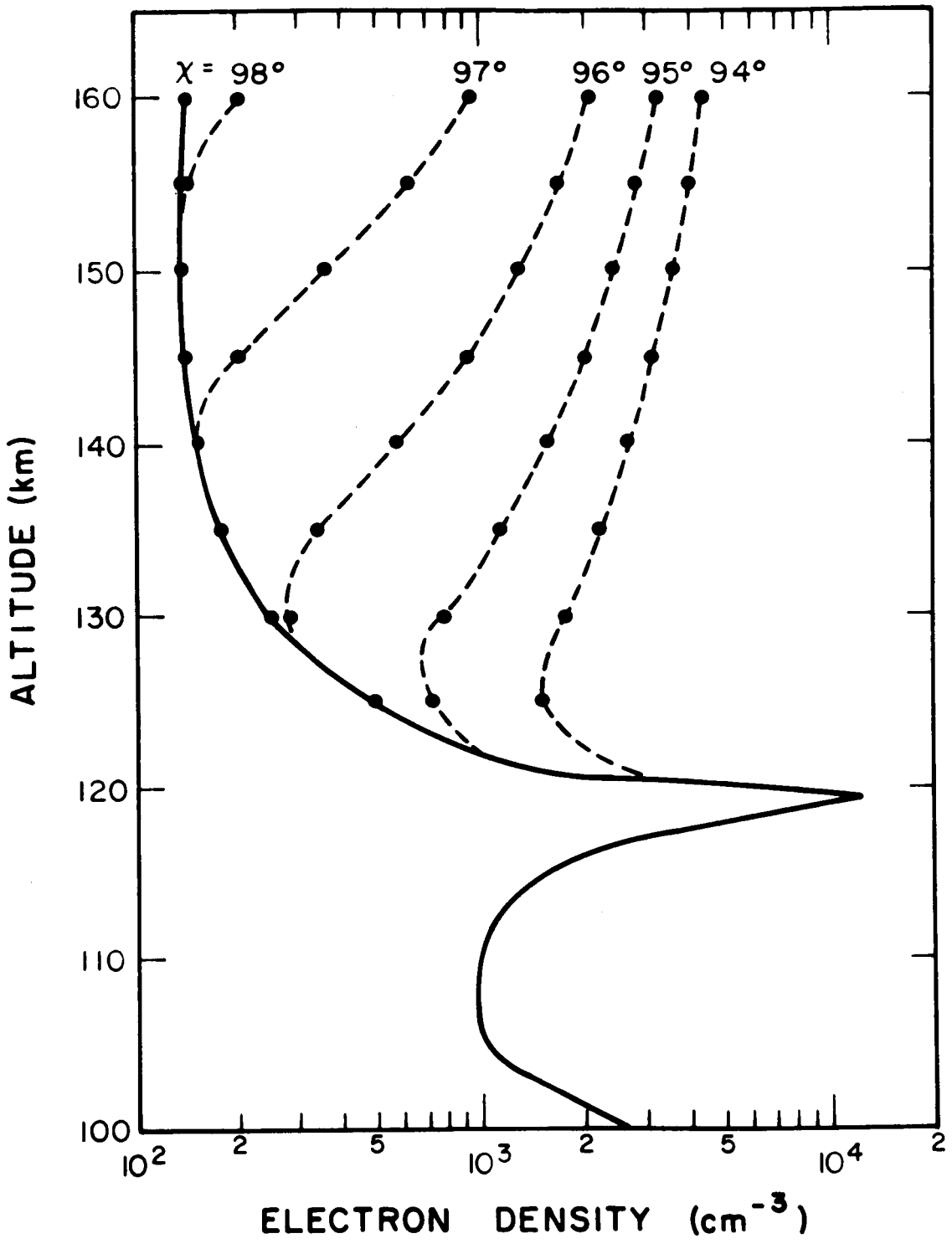

Figure A-8. Computed electron density profiles. The initial electron density profile is that of Nike Apache 14.144.

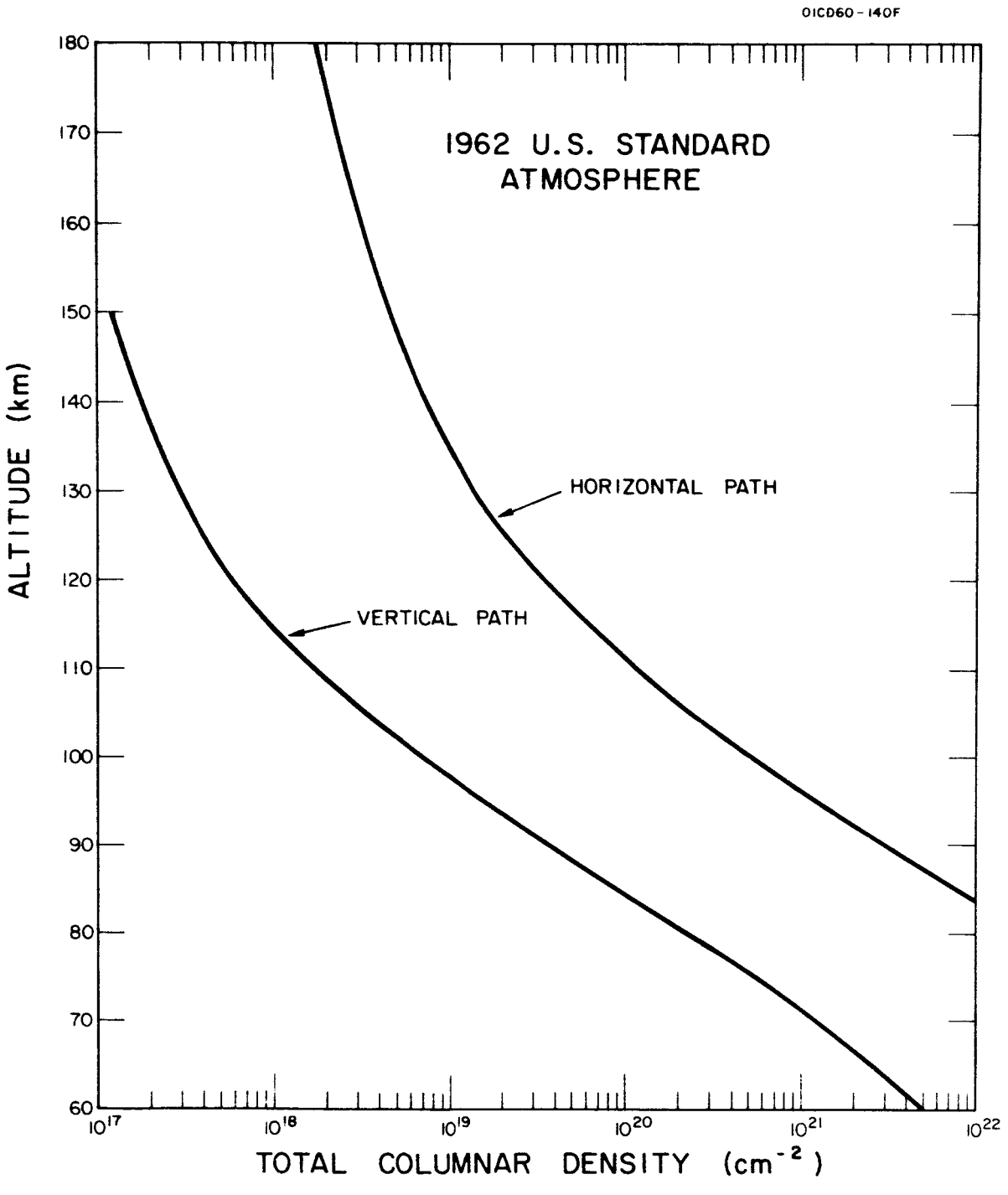

Figure A-9. Columnar density for vertical and horizontal path. For the horizontal path altitude is the minimum ray height.

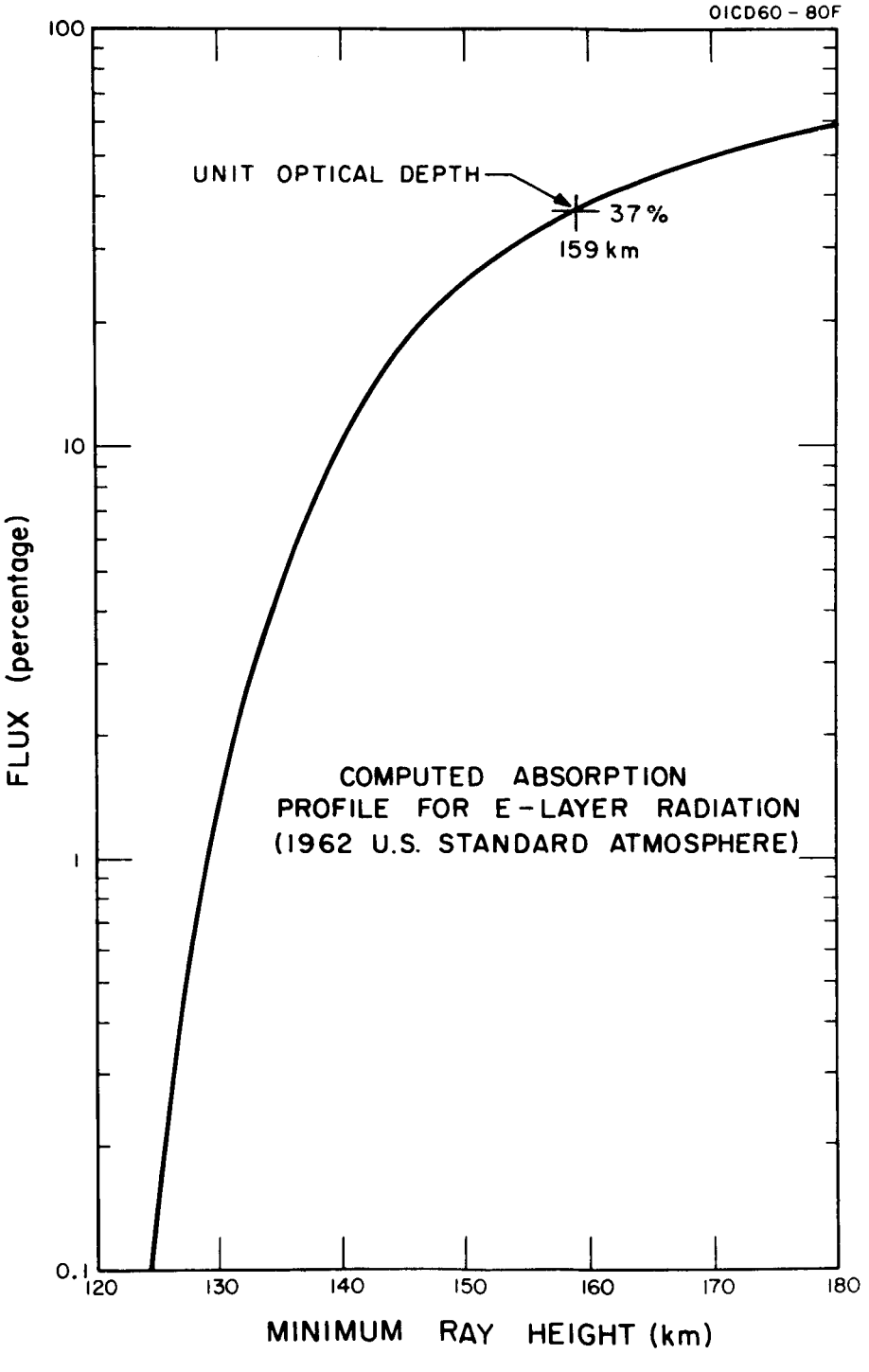

Figure A-10. Computed absorption profile for E-layer radiation.

The next step is computation of the ionization rate as a function of altitude and zenith angle. The ionization rate at the peak of the E layer for $X=0^{\circ}$ is about 10^{3} cm^{-3} sec^{-3}, so that at this altitude the unattenuated flux would produce an ionization rate some three times larger: a value of 3×10^{3} cm^{-3} sec^{-1} is assumed in subsequent calculations. At greater altitudes, the ionization rate for unattenuated fluz is reduced in proportion to the density. The values of ionization rate are obtained from U.S. Standard Atmosphere 1962 as a function of altitude and are as follows:

Table A-2: Assumed Ionization Rate Due to Unattenuated E-Layer Radiation

Altitude, km	125	130	135	140	145	150	155	160
Ionization rate, cm^{-3} sec^{-1}	187	112	73.2	50.9	36.9	27.8	22.0	17.7

Combining these values of ionization rate for unattenuated flux with the calculated absorption profile of Figure A-10, the ionization rate is obtained as a function of altitude and zenith angle. This is given in Figure A-11. The dashed line indicates the trajectory of Nike Apache 14.145. It is seen that only above 150 km is there any possibility that E-layer radiation has contributed to the total electron density of the region at the time of the rocket observations.

This is further confirmed by a computation for an altitude of 160 km illustrated in Figure A-12, which shows (a) the effect of Lyman-α radiation alone, loss process neglected; (b) E-layer radiation alone, loss process neglected, (c) the total effect of Lyman-α and E-Layer radiation, loss process neglected, and (d) both radiations with a loss process represented by $\alpha = 1 \times 10^{-7}$ cm^{-3} sec^{-1}. It will be noted that for $X < 95^{\circ}$ the ionization by Lyman-α is the dominant radiation. It is also seen that loss by recombination is not particularly significant at these low electron densities.

This figure also illustrates the effective onset of the Lyman-α ionization. Extrapolation of the linear part of the electron density curve intersects the point of zero electron density at a zenith angle which is found to correspond with a flux of 55 percent of the incident flux. This percentage is found to be same for the range of altitudes considered (125 to 160 km). This effective onset point provides a very sensitive confirmation that Lyman-α is responsible for the initial ionization of the upper E region.

Finally, Figure A-13 shows the effective onset of ionization by Lyman-α radiation (as defined above, corresponding to 55 percent of incident flux) and of E-layer radiation, which is given for a computed ionization rate of 1.0 cm^{-3} sec^{-1}. The interval in zenith angle between these two curves show the useful period during which the increase in electron density can be used to obtain nitric oxide densities.

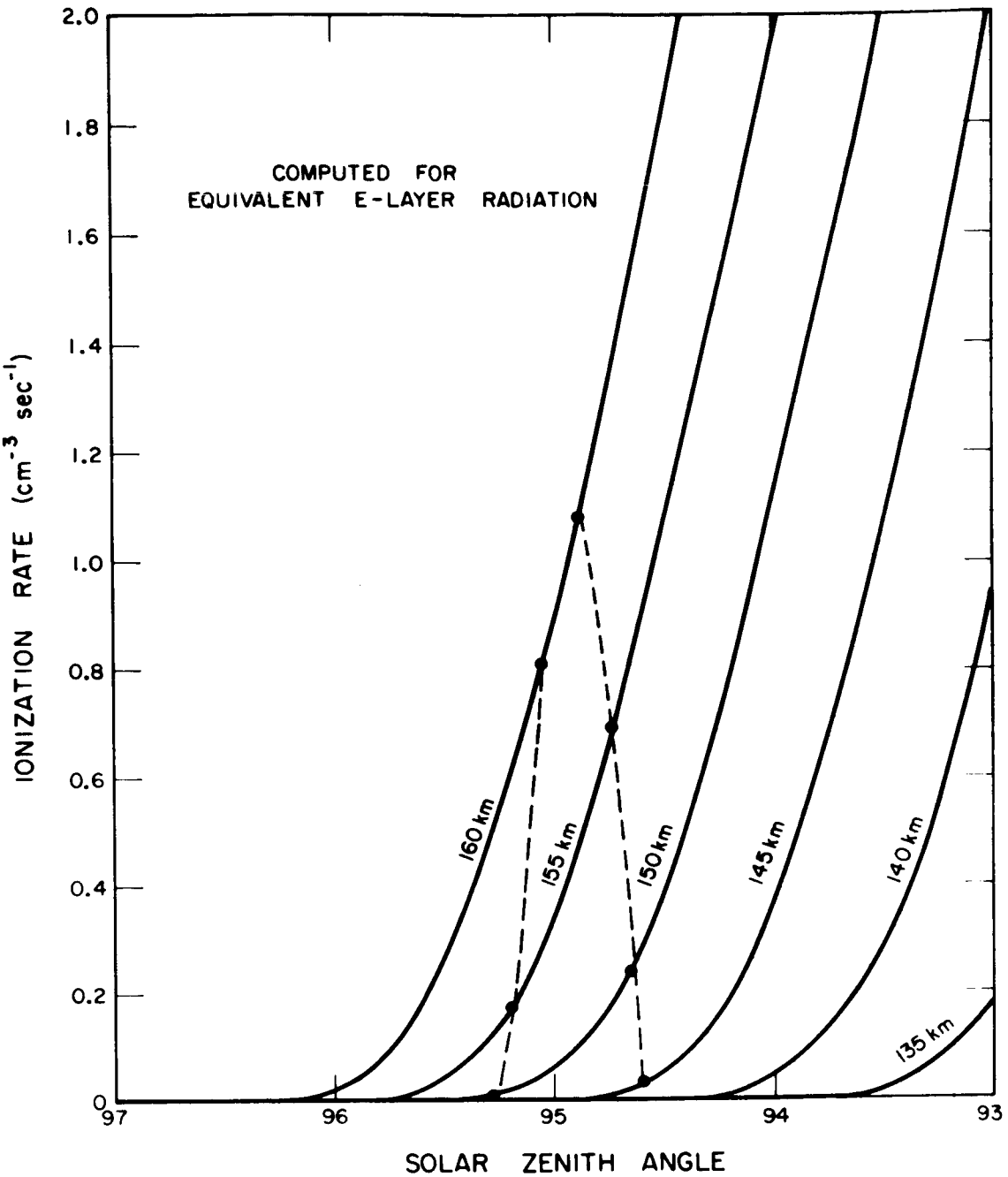

Figure A-11. Computed ionization rate for E-layer radiation.

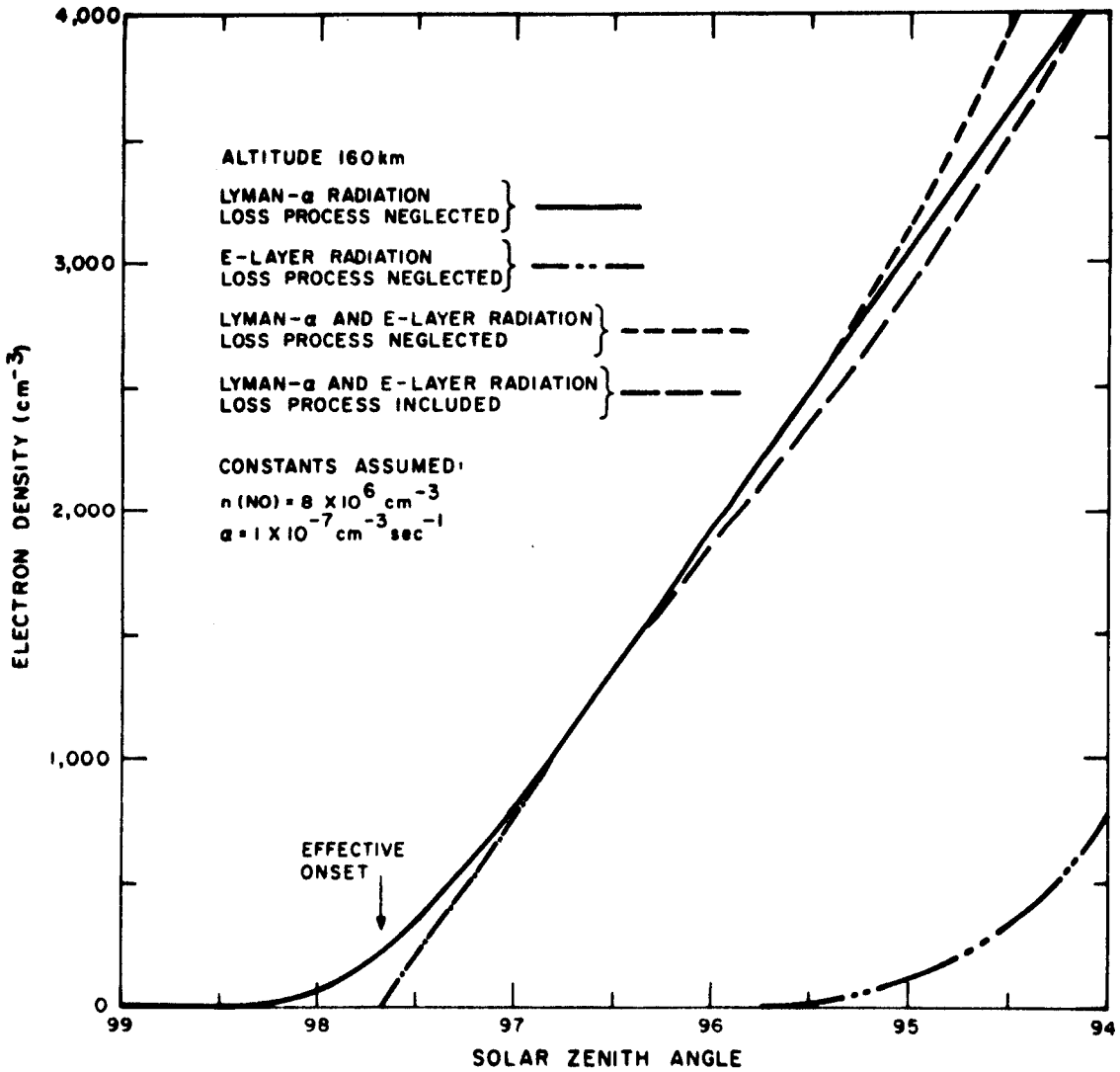

Figure A-12. Combined effect of ionization by Lyman-α and E-layer radiation and loss by recombination.

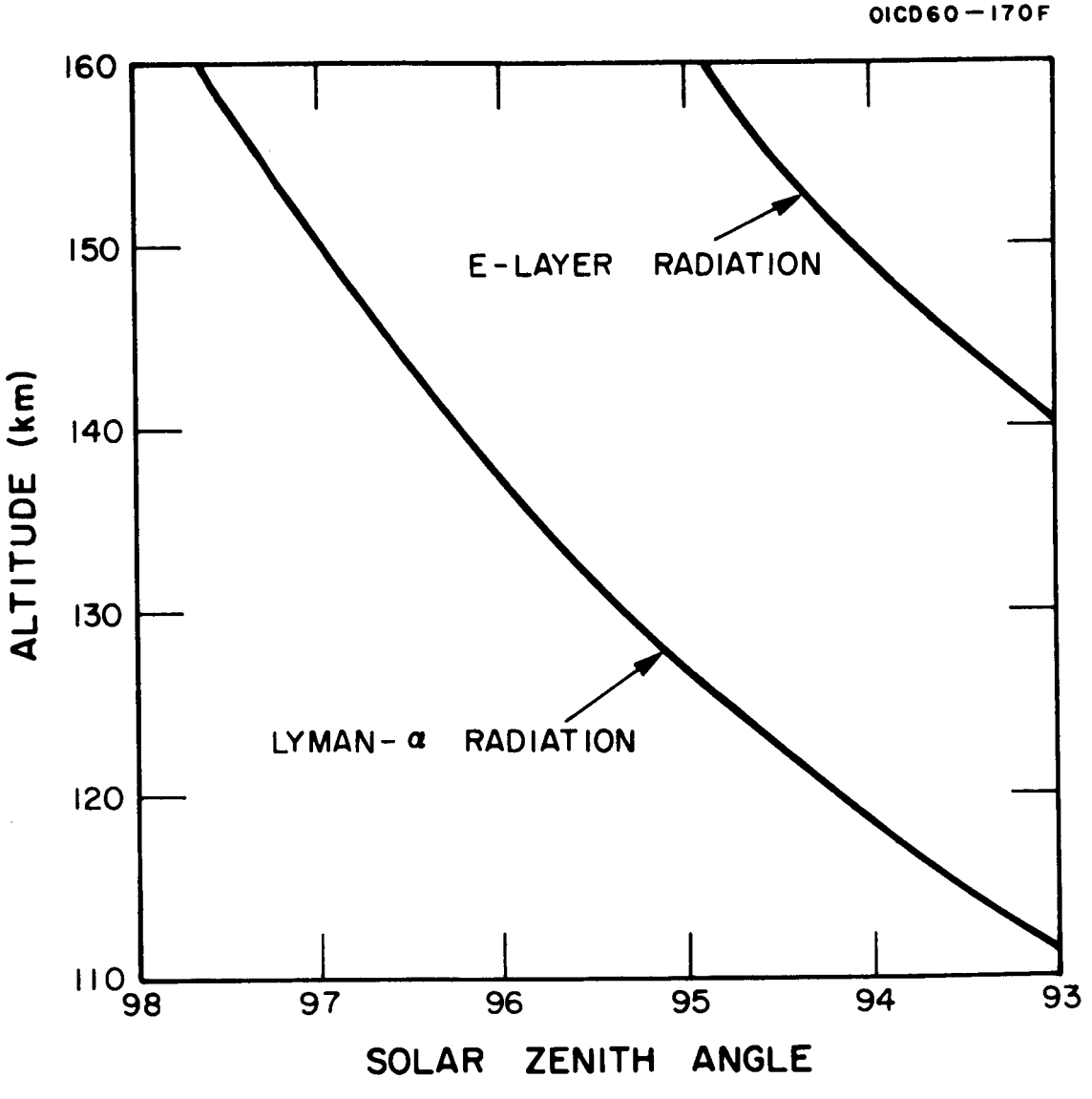

Figure A-13. Zenith angle for onset of ionization by Lyman-α and by E-layer radiation.

IONOSPHERIC WINDS

The analysis presented here ignores the possible effects of horizontal transport of ionization by the ionospheric winds. The velocity of the terminator (the line on the earth's surface separating day and night) is about 350 m/sec at the latitude of Wallops Island. Components of the wind in the east-west direction having velocities of this order could seriously affect the conclusions of the analysis.

Fortunately, information on the magnitude and direction of the wind at this time was obtained by the vapor trail technique laid down by a rocket launched 14 minutes before Nike Apache 14.145 [A-8]. It shows that the wind throughout the region had an east-west component of about 130 m/sec, the direction transport being toward the west. This velocity is not small enough to be dismissed as negligible but is not likely to significantly affect the conclusions relating to the concentration of nitric oxide in the upper E region.

CONCLUSION

It appears feasible to determine the concentration of nitric oxide up to 160 km, and perhaps higher, by selecting appropriate launch times for the rocket flights although each rocket flight (using Nike Apache) can give data only over a height interval of no more than 30 km.

There is an alternative approach, not using sounding rockets, which offers the possibility of more systematic investigation of the nitric oxide concentration of the upper E region. Normal radio sounding of the ionosphere from the ground cannot give any information in the region of the valley above sporadic E layers. However, it has recently been demonstrated by LeLonde [A-9] that the technique of incoherent backscatter can be used to obtain electron density profiles of the E region at sunrise. The technique requires the use of a powerful radar with a large antenna, such as the instrument at the Araceibo Observatory in Puerto Rico, where values of electron density as low as 100 cm^{-3} have been observed before sunrise. The instrument is somewhat limited in height and time resolution compared with the roclet observation but could probably obtain the required sequence of electron density profiles. A rocket flight would be desirable to establish the absorption profile for Lyman-α radiation. It is also desirable that ionospheric winds be observed by the vapor trail technique so that their effect can be properly included.

The ionization of nitric oxide by solar Lyman-α radiation determines the initial, pre-sunrise, increase of electron density in the upper E region. The source of ionization becomes negligible some 3 degrees of

zenith angle after its onset, when radiation which will form the daytime E layer starts to illuminate the region. During the day, Lyman-α ionization of nitric oxide contributes less than 1 percent of the total ionization rate and is quite negligible.

One interesting aspect of the analysis which is worthy of further investigation is the question of approach to equilibrium: at what zenith angle does the ionization at a given altitude reach equilibrium between production and loss rates? It will be noted that the initial ionization by Lyman-α brings the electron density up to a level of several thousand, cm^{-3}, before the E-layer radiation becomes effective. It appears that equilibrium will be attained by the time the electron density reaches about 10^4 cm^{-3}, which occurs about the time of ground sunrise. Thus, it is tentatively concluded that the region above the Sporadic E layers is in equilibrium at ground sunrise.

APPENDIX A

REFERENCES

A-1. Bowhill, S.A. and Smith, L.G.: Rocket Observations of the Lowest Ionosphere at Sunrise and Sunset. Space Research VI, 1966.

A-2. Barth, C.A.: Nitrogen and Oxygen Atomic Reactions in the Chemosphere. Chemical Reactions in the Lower and Upper Atmosphere, Stanford Research Institute, Wiley & Sons, New York, 1961, pp. 303 - 326.

A-3. Smith, L.G.: Langmuir Probes for Measurements in the Ionosphere. NASA Contract No. NASw-1141, GCA Corporation Technical Report No. 65-25-N, 1965.

A-4. Bowhill, S.A. : Private Communication, 1966.

A-5. Smith, L.G. and Weeks, L.H.: Molecular Oxygen Densities from Rocket Measurements of Lyman-α Absorption Profiles. GCA Corporation Technical Report No. 65-10-N, 1965. NASA CR-392, 1966.

A-6. Barth, C.A.: Rocket Measurements of Nitirc Oxide in the Upper Atmosphere, Presented at COSPAR meeting, 1964.

A-7. United States Standard Atmosphere, 1962. National Aeronautics and Space Administration, U.S. Air Force, and U.S. Weather Bureau, Government Printing Office, Washington, D.C., 1962.

A-8. Bedinger, J.F. and Knaflich, H.B.: Observed Characteristics of Ionospheric Winds. Radio Science, Vol. 1 (New Series) No. 2, February 1966.

A-9. LaLonde, L.M.: E Region Effective Recombination Rates from Incoherent Scatter Measurements at Araceibo, Presented at URSI Meeting, April 1966.

APPENDIX B

PAYLOAD INSTRUMENTATION

Three scientific experiments -- DC probe, CW propagation, and two narrow-band uv detectors -- were installed in the ten payloads instrumented during this program. One payload (Nike Apache 14.229) carried a spherical ion trap and an RF probe in place of the uv detectors and solar aspect sensor. The major engineering support instrumentation included magnetic and solar aspect sensors, baroswitches (50,000 and 75,000 ft), telemetry, electronic timer, power supplies, and control unit. Since design and development details of the scientific and support instrumentation have been discussed previously [B-1 , B-2]*, only the details of the modifications will be presented in this report.

Type A and Type B payloads shown in Figures B-1 and B-2, contain the installations listed in Table B-1. The system diagrams of the Type A and B payloads are shown in Figures B-3 and B-4.

Payload Control

The control console, the payload control deck, and the electrical interface is shown in Figure B-5. The umbilical cable containing 22 No. 16 wires is attached to the payload through a Deutsch (DS00-27S) 27-pin flyaway connector located in the tub section. This connector replaces the explosive disconnect used formerly and permits control of all payload functions up to the instant of launch. Power transfer is now accomplished through a latching relay located on the control deck instead of the motor-driven, cam-actuated transfer switch previously used. Although the transfer switch was extremely reliable and did not return to the "external power" position as a result of payload vibration and "g" loading during the launch phase, it was very cumbersome. As may be noted in the circuit of Figure B-5, if the latching relay now used should unlatch during the launch phase, power would be applied to relatch it through the 75,000 ft baroswitch and diode, CR4, when the 50,000 ft baroswitch closes on ascent.

DC Probe

The nose tip electrode was plated with Rhodium so that a clean metal surface could be ensured and photoemission reduced.

A design change has been incorporated into the nose tip electrode assembly. As the sensitivity of the dc probe has been increased, electrical leakage across the insulator has become more important. Two causes of leakage -- humidity and heat -- can be distinguished. This latter problem has been aggravated by the reduction in mass of the nose electrode (when the configuration was changed

* Numbers in [ ] represent references.

TABLE B-1

TYPE A AND B PAYLOAD INSTRUMENTATION

I. SCIENTIFIC INSTRUMENTATION

(A) DC Probe

1. Nose Electrode and Connector
2. Probe Sweep Circuit and Electrometer, GCA Model XLP-110

(B) CW Propagation

1. Receiver, Spacecraft, Inc. Model IR-434
2. Ferrite Loop Antenna
3. Non-metallic Cylindrical Housing

(C) UV Detectors (Type A only)

1. Lyman-α (1216Å) Ion Chamber
2. 1450Å photometer or 1300Å ion chamber (In some flights the ion chamber mode of operation was used, in others gas gain was used.)
3. Power Supply, 650 volts, TEC Model 7002 (gas gain only)
4. Electrometer

(D) Spherical Ion Trap (Type B only)

(E) RF Probe (Type B only)

II. ENGINEERING SUPPORT INSTRUMENTATION

(A) Solar Aspect Sensor, GCA Model XAS-102 (Type A only)

(B) Magnetic aspect sensor, Schonstedt Model RAM-3

(C) Baroswitches, CHI Model 6617-A, modified, 50,000 ft and 75,000 ft

(D) Main Battery Power, +28.5 volt, Yardney Type HR-05

(E) Bias Battery - 14.8 volt, Mallory

(F) Electronic Timer

(G) Dual-Door Release Mechanism

(H) Control Deck

(I) Sub-Carrier Oscillator, Vector Model TS-41

(J) Mixer Amplifier, Vector Model TA-48

(K) Transmitter, 1/4 watt, Vector Model TRPT-250

(L) Transmitter Antenna, Four Element Turnstile

(M) NASA Type I Aluminum Payload Housing, Modified, with 11° Nose Cone

(N) Boom Extension Mechanism (Type B only)

DIF

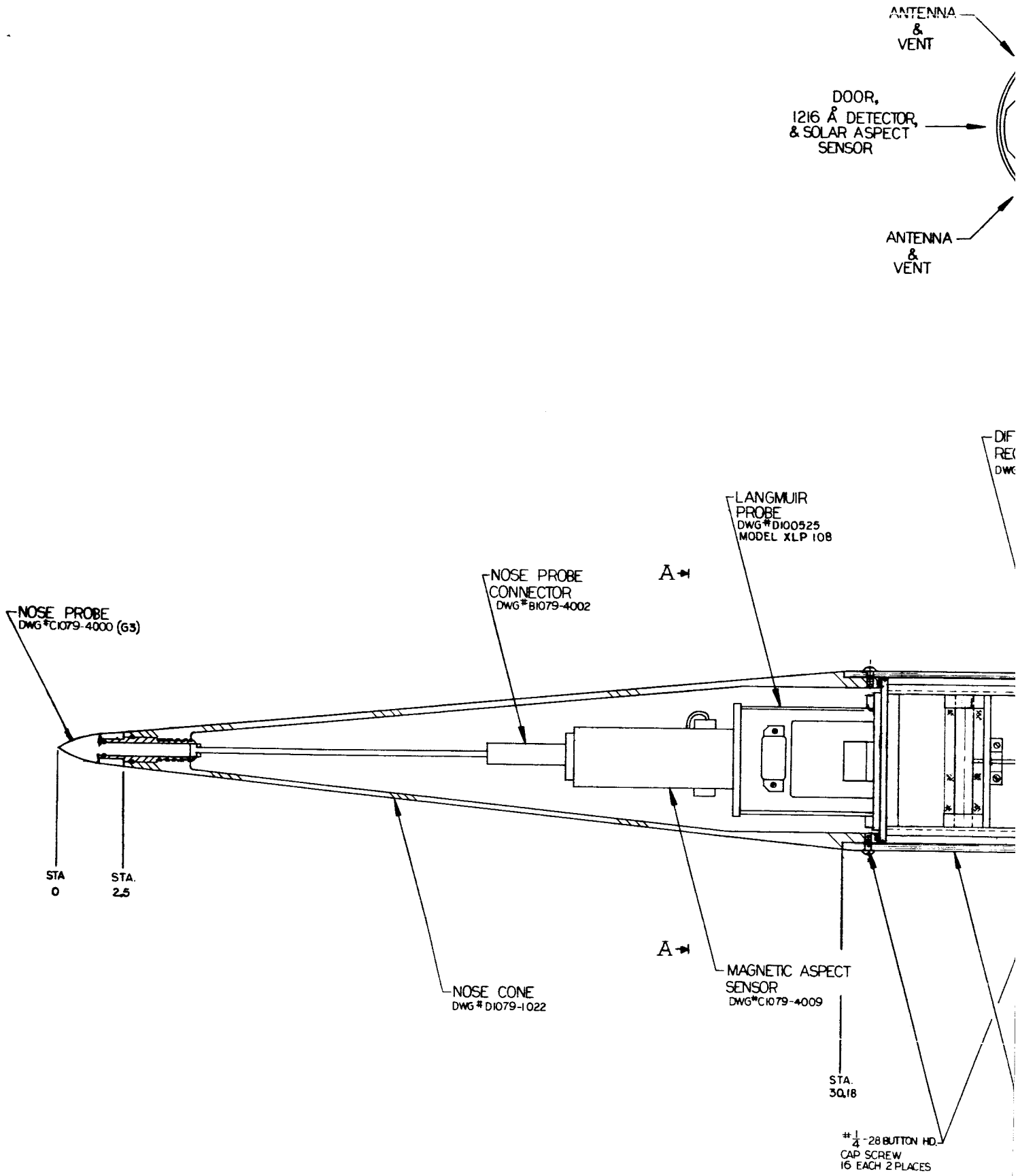
ANTENNA & VENT
DOOR, 1216 Å DETECTOR, & SOLAR ASPECT SENSOR
ANTENNA & VENT
DIF REC DWG
LANGMUIR PROBE DWG # D100525 MODEL XLP 108
NOSE PROBE CONNECTOR DWG # B1079-4002
A
NOSE PROBE DWG # C1079-4000 (G3)
STA 0
STA. 2.5
A
NOSE CONE DWG # D1079-1022
MAGNETIC ASPECT SENSOR DWG # C1079-4009
STA. 30.18
1/4 - 28 BUTTON HD. CAP SCREW 16 EACH 2 PLACES

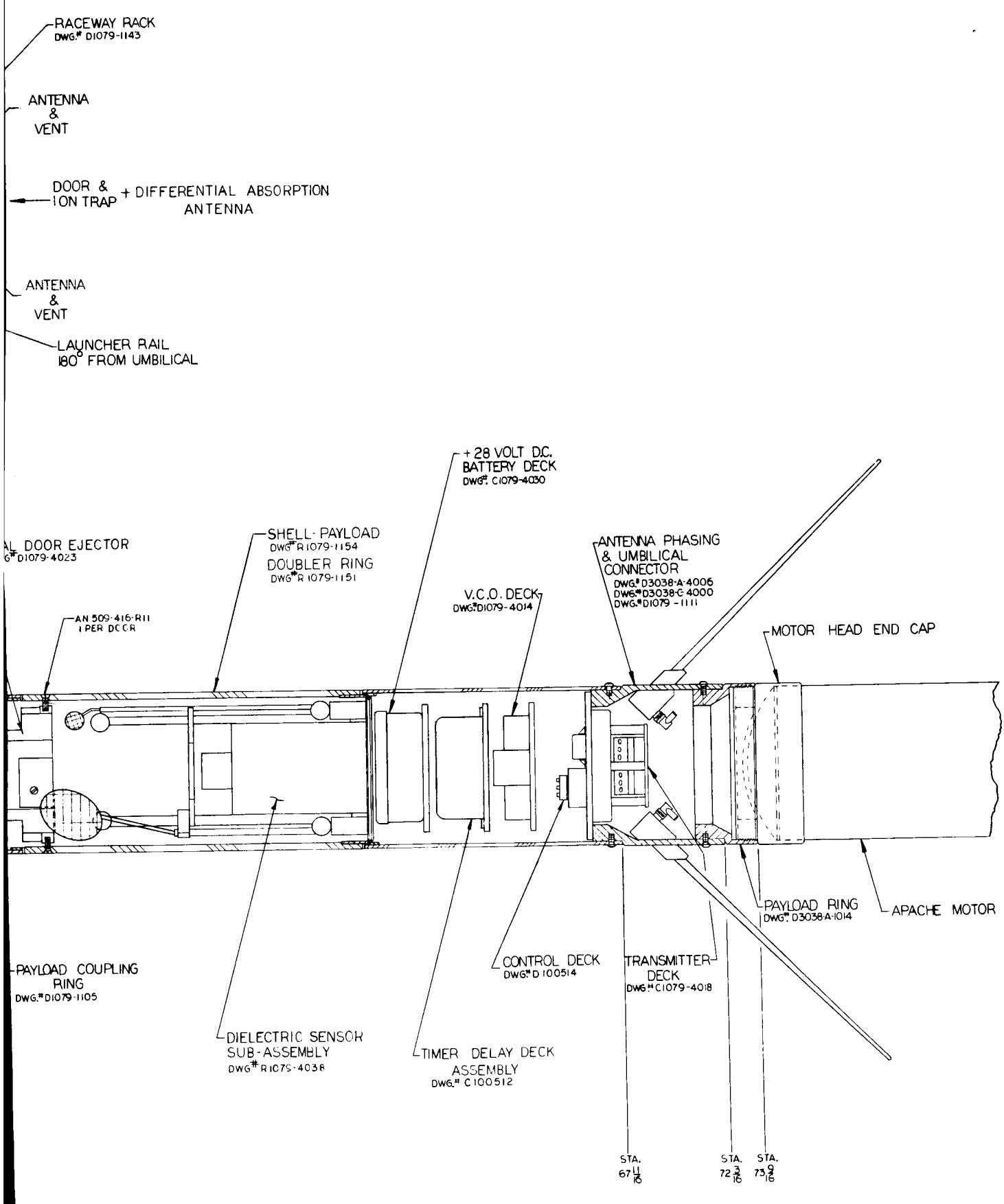
RACEWAY RACK
DWG.# D1079-1143
ANTENNA & VENT
DOOR & ION TRAP
+ DIFFERENTIAL ABSORPTION ANTENNA
ANTENNA & VENT
LAUNCHER RAIL 180° FROM UMBILICAL
+ 28 VOLT D.C. BATTERY DECK
DWG.# C1079-4030
AL DOOR EJECTOR
G.# D1079-4023
SHELL-PAYLOAD
DWG.# R1079-1154
DOUBLER RING
DWG.# R 1079-1151
V.C.O. DECK
DWG.# D1079-4014
ANTENNA PHASING & UMBILICAL CONNECTOR
DWG.# D3038-A-4006
DWG.# D3038-C-4000
DWG.# D1079-1111
AN 509-416-R11
1 PER DCCR
MOTOR HEAD END CAP
PAYLOAD RING
DWG.# D3038-A-1014
APACHE MOTOR
PAYLOAD COUPLING RING
DWG.# D1079-1105
CONTROL DECK
DWG.# D 100514
TRANSMITTER DECK
DWG.# C1079-4018
DIELECTRIC SENSOR SUB-ASSEMBLY
DWG.# R1079-4038
TIMER DELAY DECK ASSEMBLY
DWG.# C100512
STA. 67 11/16
STA. 72 3/16
STA. 73 9/16

84-2

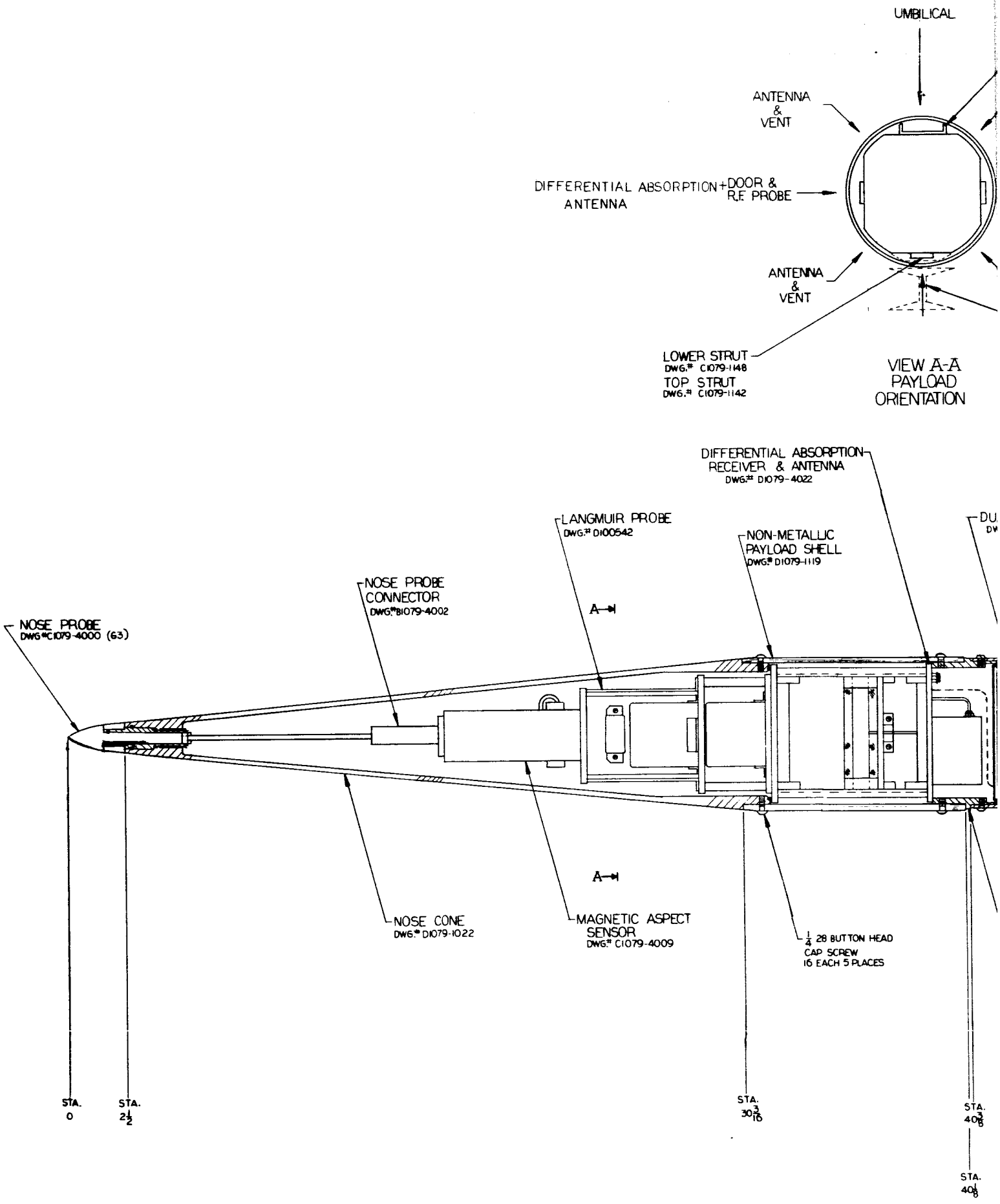

Figure B-2. Type B payload assembly.

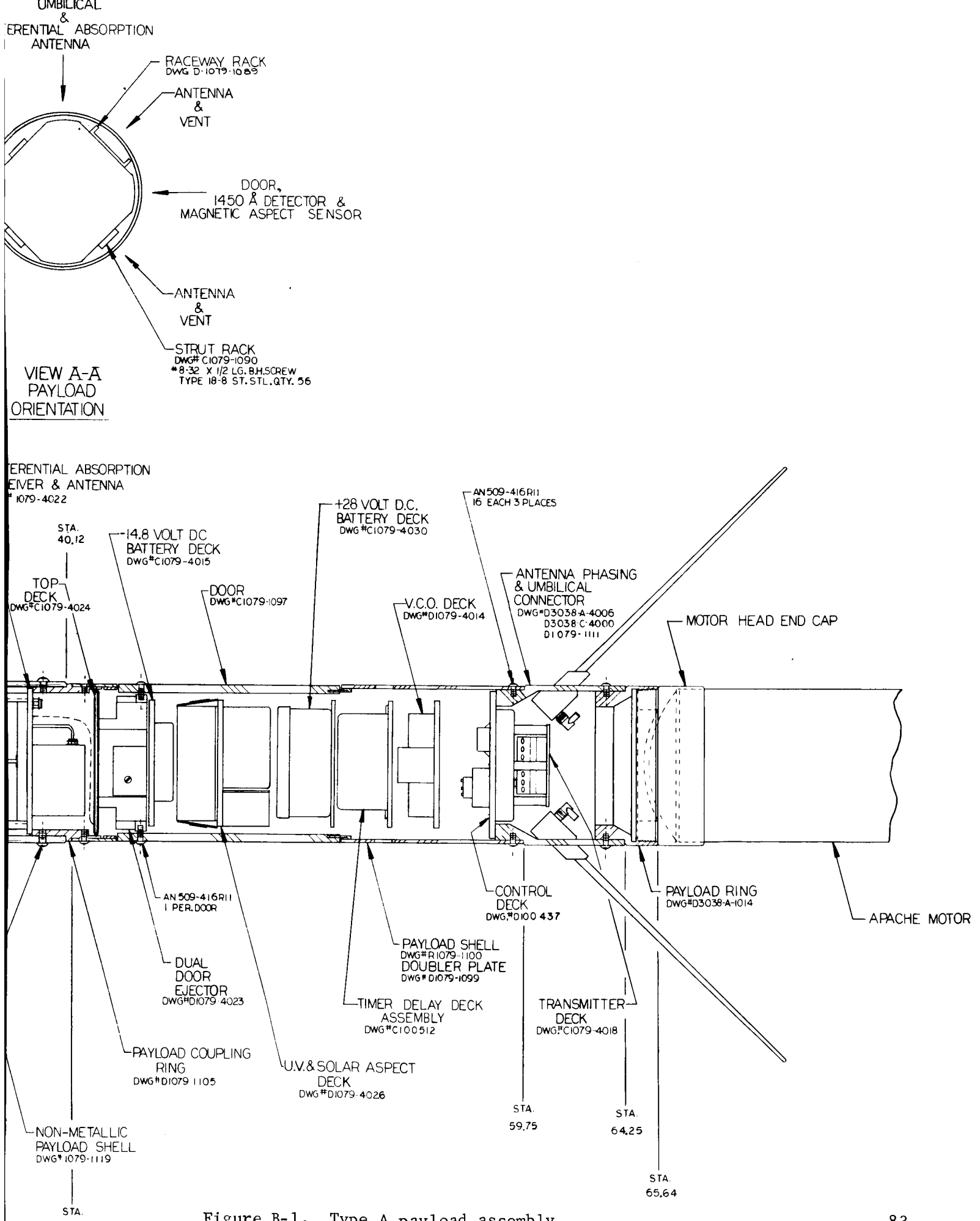

Figure B-1. Type A payload assembly.

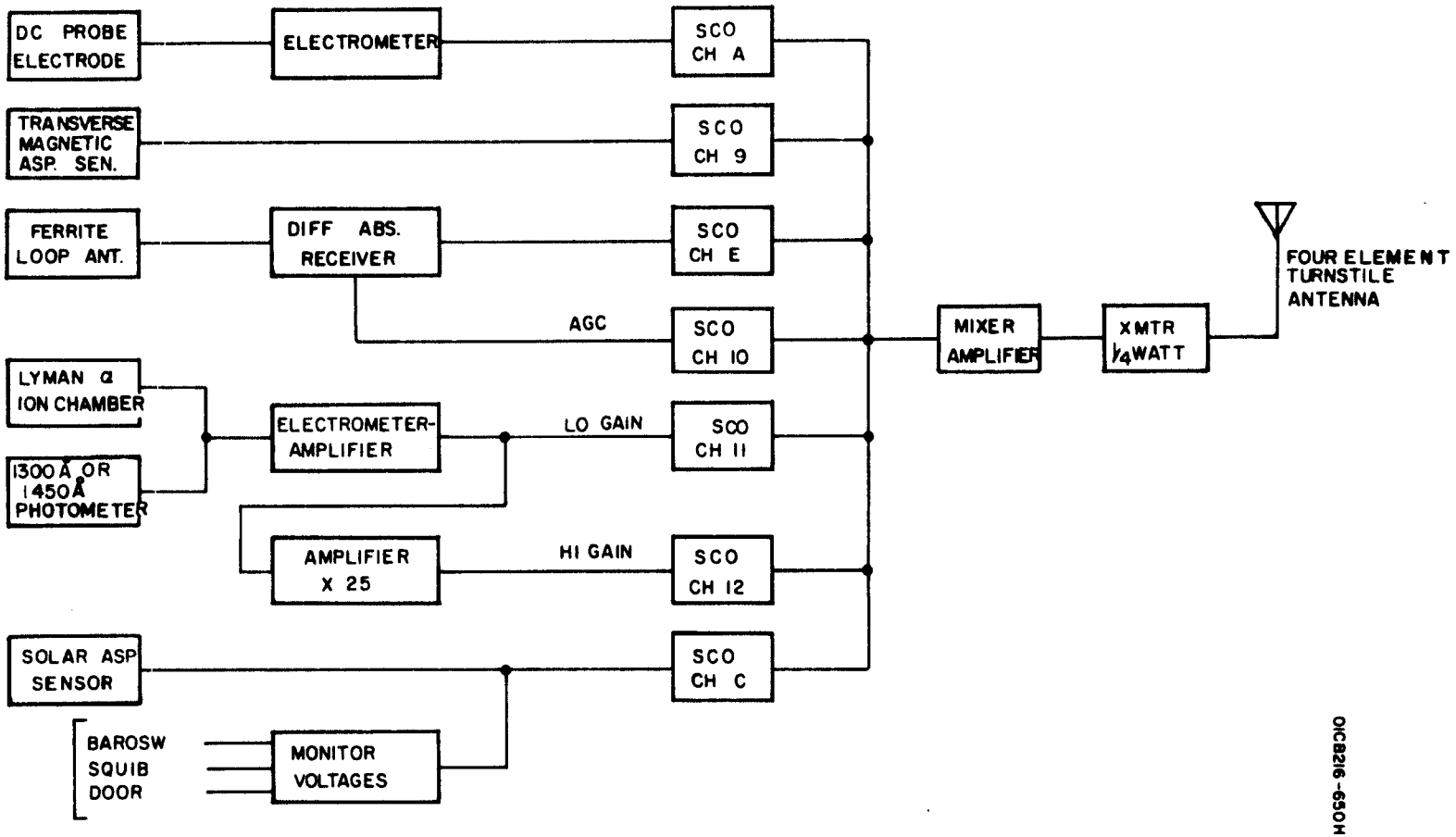

Figure B-3. Diagram of Type A payload.

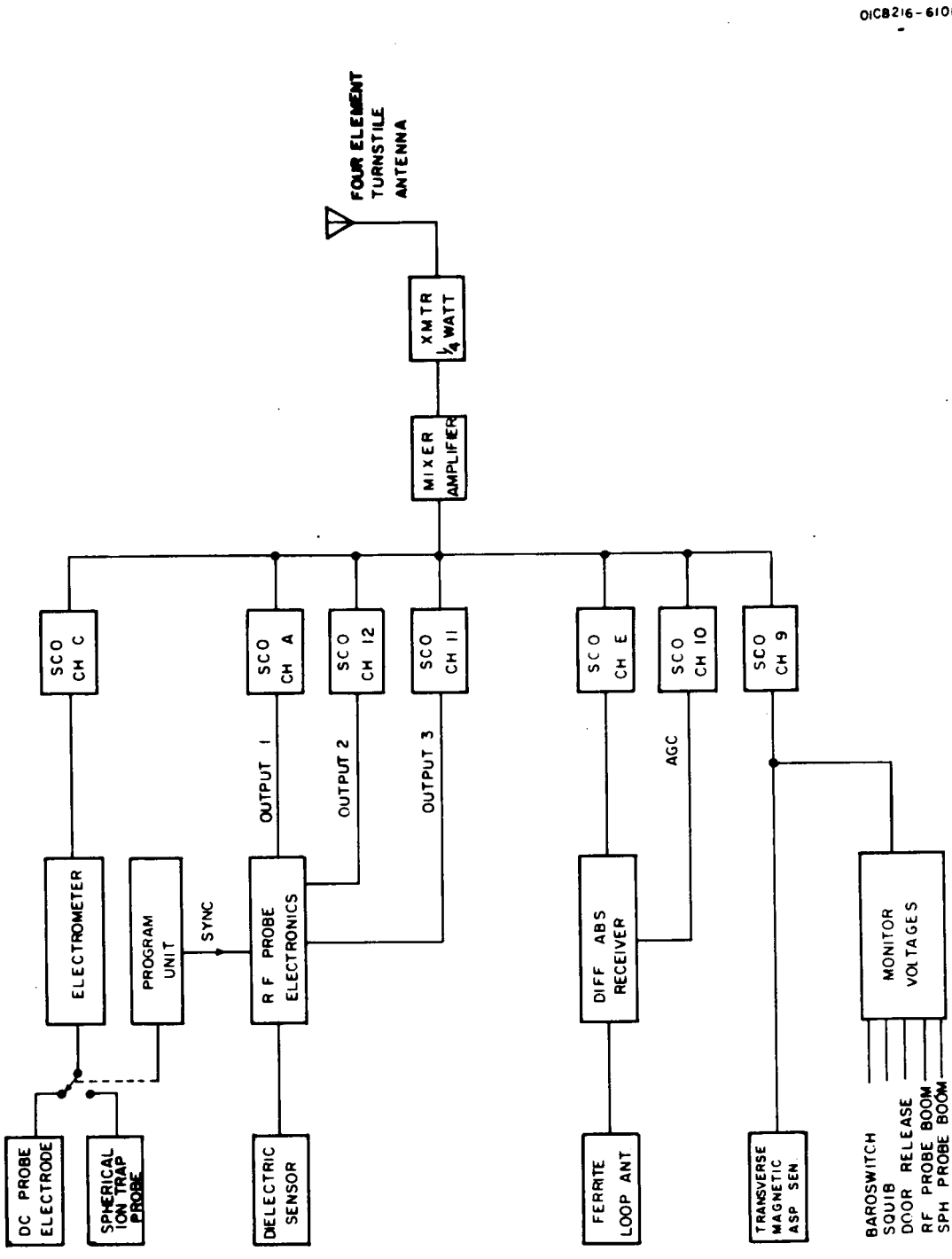

Figure B-4. Diagram of Type B payload.

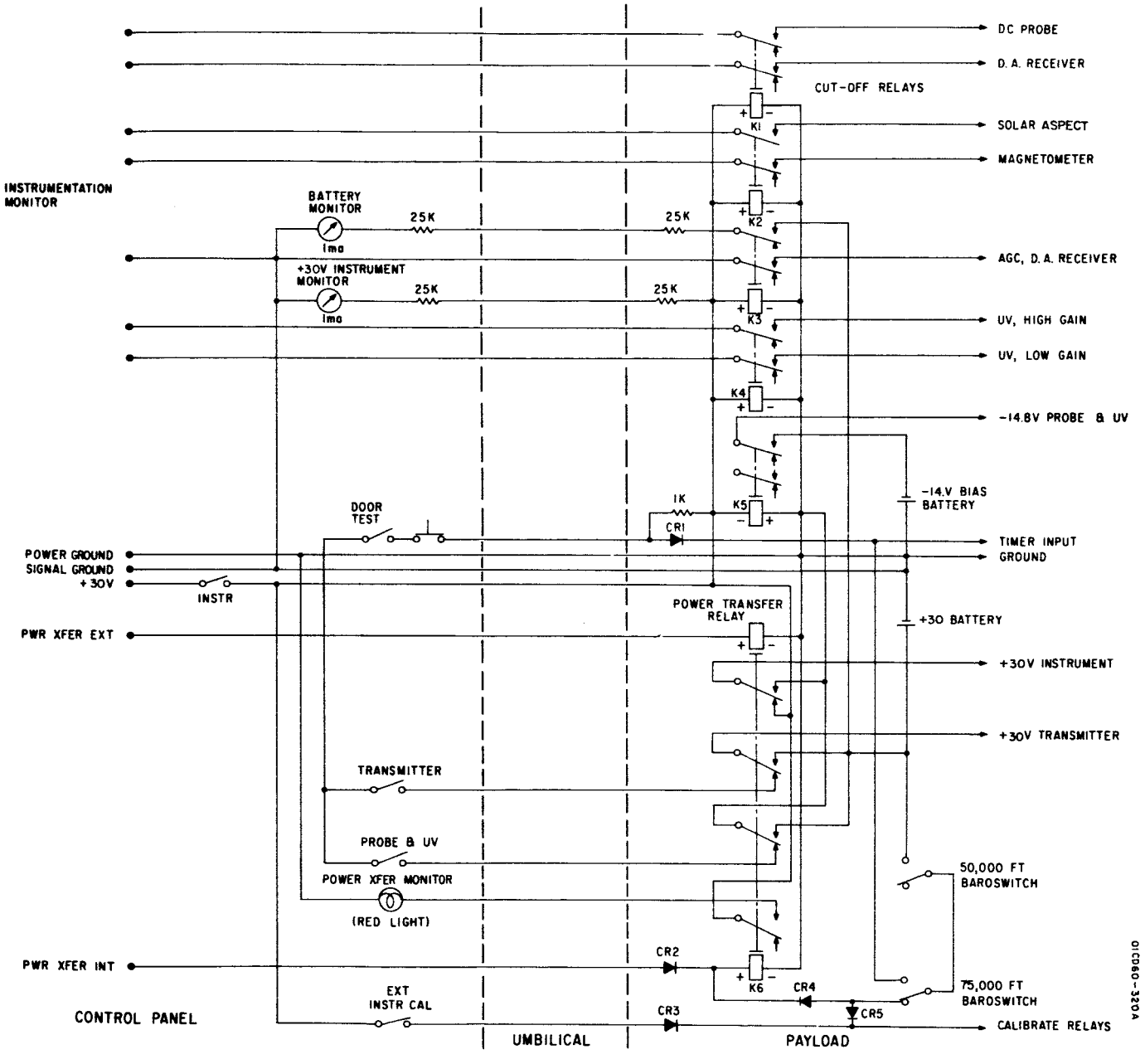

Figure B-5. Payload control, monitors, and electrical interface.

from cone to ogive) and by reduction is mass of the aluminum nose cone which is now made by spinning rather than casting. The arrangement used previously consisted of an internal insulator made of glass-silicone-glass and an external insulator of ceramic (95 percent pure alumina) as shown in Figure B-6. This assembly also included an ogive-shaped nose tip. The leakage path from nose tip electrode to ground (nose cone) is indicated as the surface between the two insulators. Figure B-7 shows the arrangement used on Nike Apaches 14.247 and 14.248. The insulator is fabricated entirely from ceramic, which is not affected by temperatures encountered during flight, and is a single piece combining what was formerly the inner and outer insulators. This eliminated the humidity problem since there is no surface in the new design on which humidity can be trapped.

Modification of the sweep circuit now provides a momentary (approximately 0.1 second) zero-check of the probe electrometer at the start of each sweep. Full details and circuit diagrams are given in reference B-2.

CW Propagation Experiment

Circularly polarized receiving antennas were installed in Nike Apache payloads 14.228 and 14.229, which were flown at the magnetic equator. Figure B-8 shows this assembly [B-3]. Two ferrite loop antennas are fixed at right angles to each other. The circularly polarized pattern is obtained by coupling the outputs of each antenna to the receiver by a hybrid junction circuit and tuning one above and the other below resonance. The linearly polarized antenna assembly is shown in Figure B-9.

Table B-2 lists the radio frequencies and polarization of rocket-borne receiving antennas used during this program.

TABLE B-2

RADIO FREQUENCIES AND ANTENNA POLARIZATION CW PROPAGATION EXPERIMENT

Nike Apache	Receiving Antenna Polarization	Frequency (MHz)
14.228	Circular	3.385
14.229	Circular	2.225
14.230	Linear	3.385
14.231	Linear	3.385
14.232	Linear	3.385
14.244	Linear	3.385
14.245	Linear	3.385
14.246	Linear	3.385
14.247	Linear	3.385
14.248	Linear	3.385

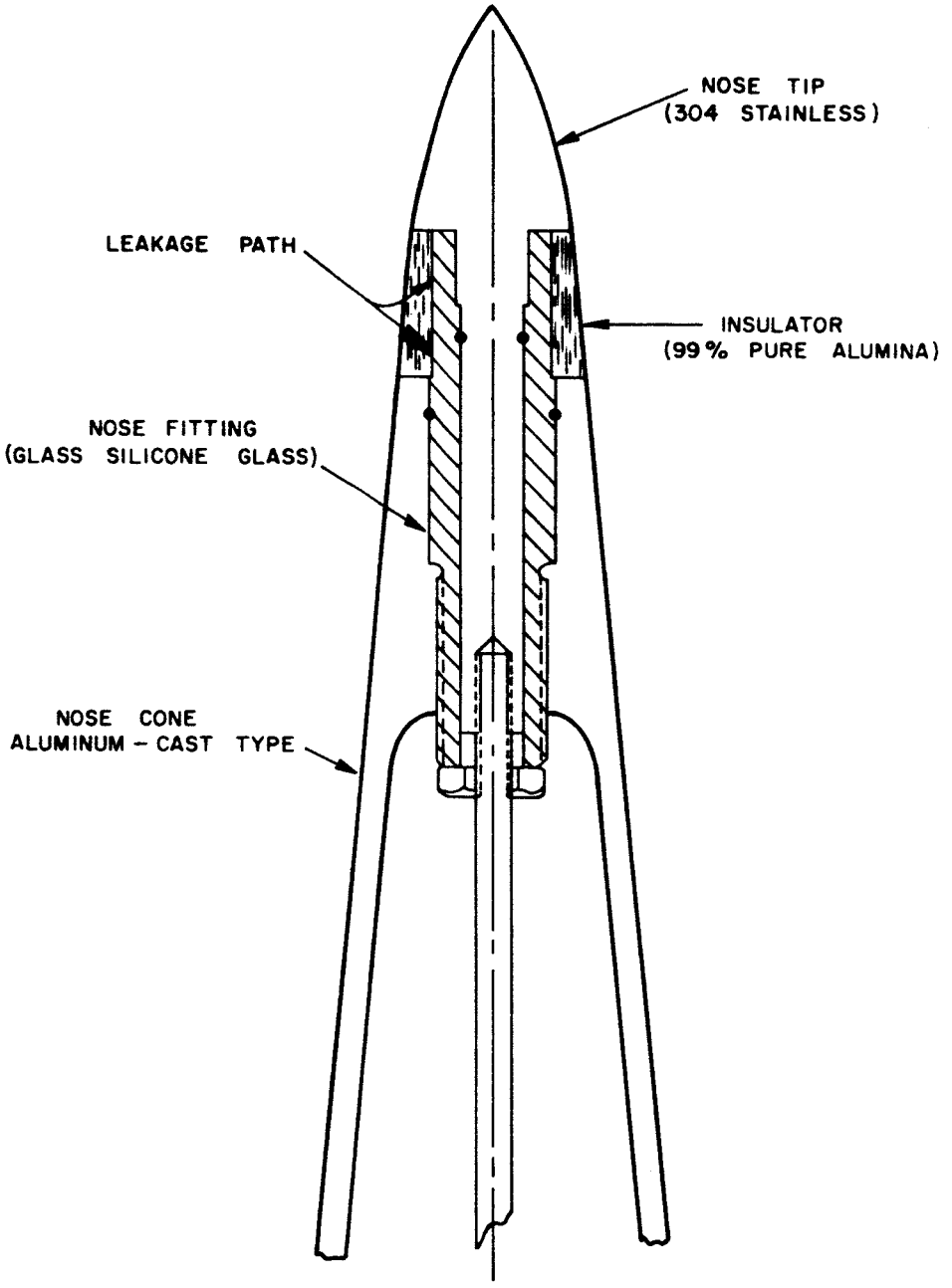

Figure B-6. Earlier nose probe assembly.

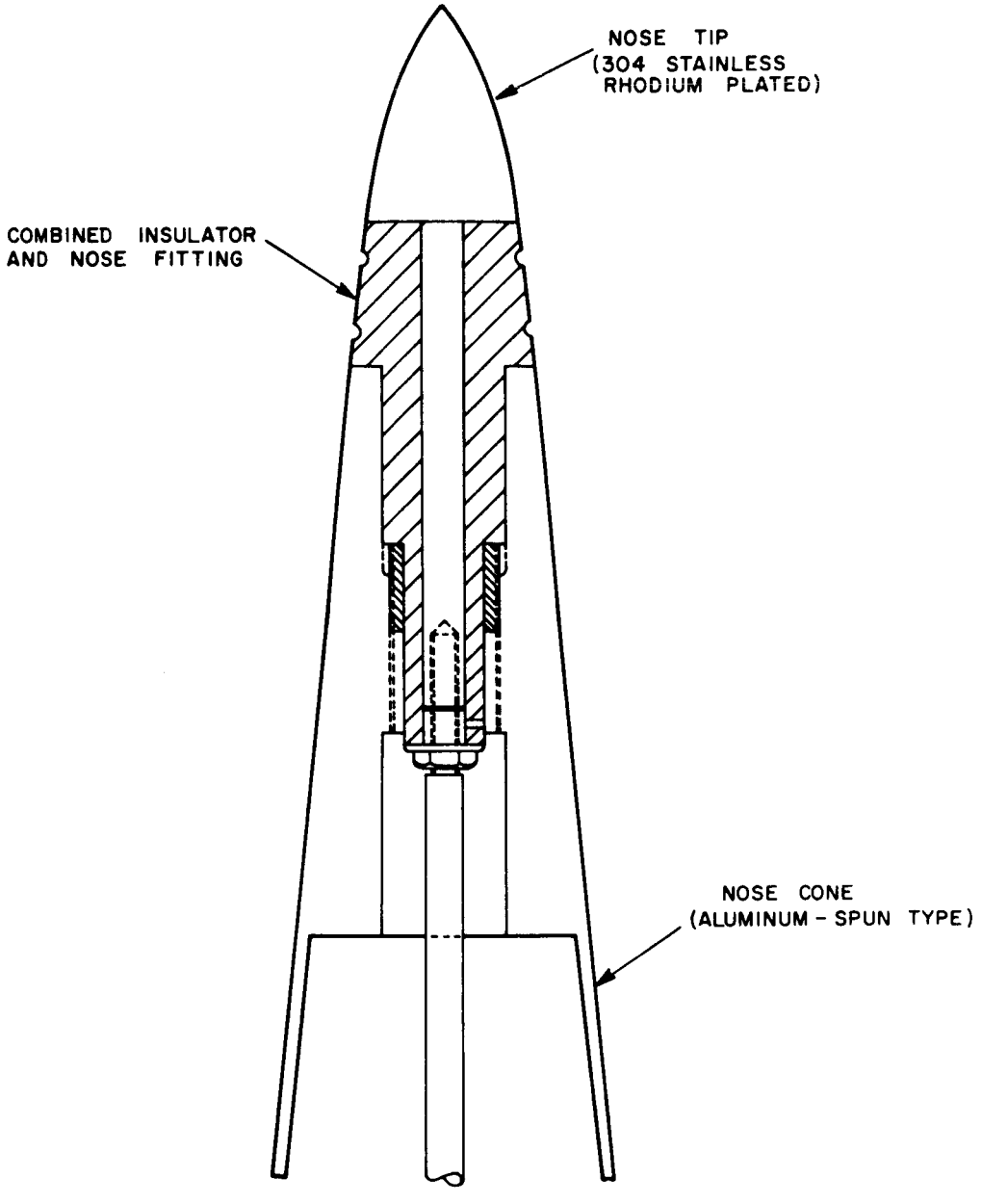

Figure B-7. New nose probe assembly.

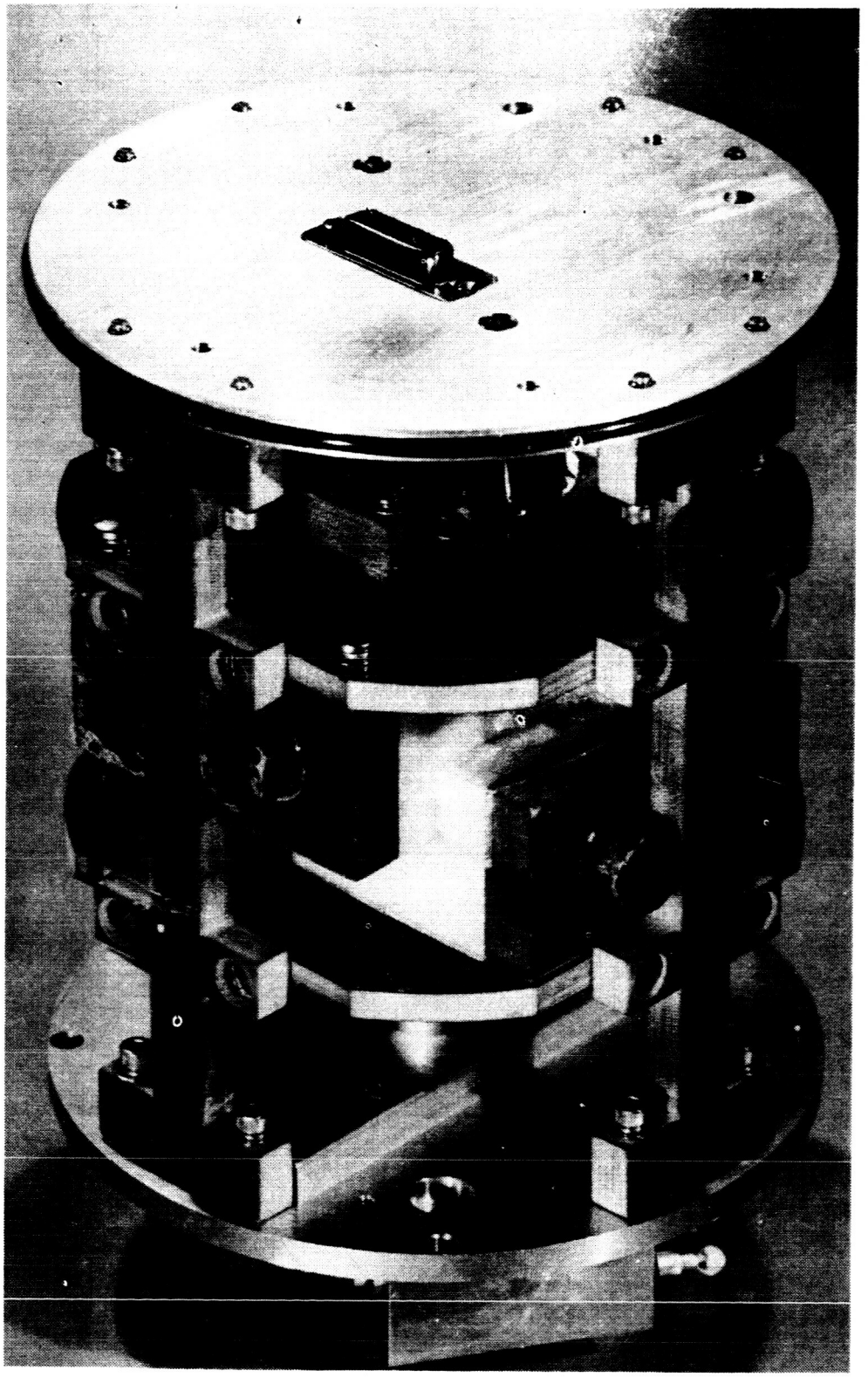

Figure B-8. CW propagation experiment assembly with circularly polarized antenna.

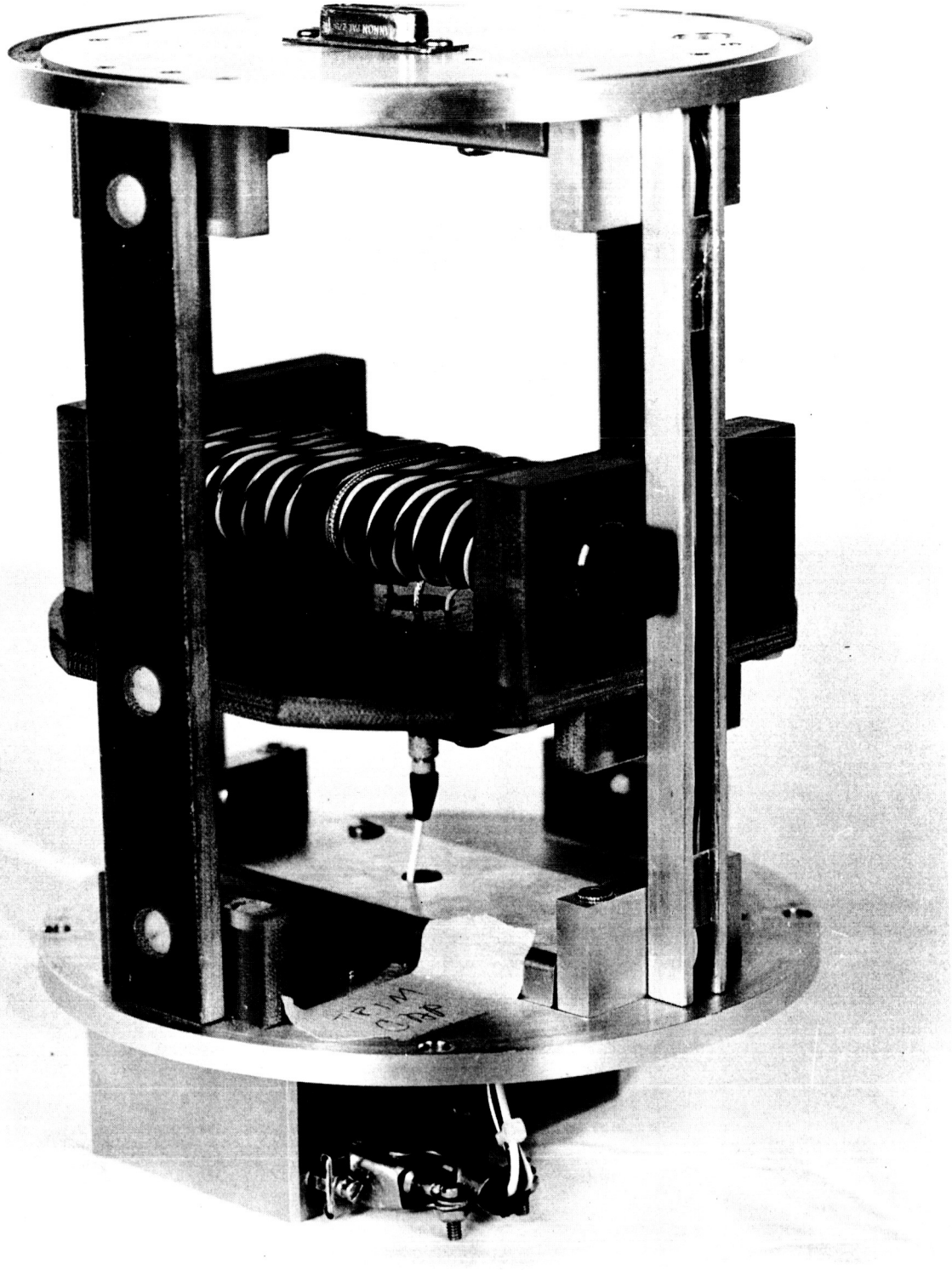

Figure B-9. CW propagation experiment assembly with linear polarized receiver antenna.

UV Detectors

Modification of the circuit for the uv experiment now allows a direct calibration at the input to the electrometer, as shown in Figure B-10. During calibration the low gain output is at full scale. A 5 volt reference signal is applied directly to the VCO to calibrate only the telemetry channel of the high gain output.

The variation of sensitivity of the individual ion chambers forced the use of three different values of feedback resistor in the uv electrometer. The resistor values and the current which produces full scale signal on the low and high gain channels are given in Table B-3.

TABLE B-3

UV ELECTROMETER AND AMPLIFIER SENSITIVITIES

Nike Apache	Feedback* Resistor	Low-Gain Full Scale (A)	High-Gain** Full Scale (A)
14.228	3×10^{9} ohm	1.7×10^{-9}	6.7×10^{-11}
14.230	5×10^{8}	1×10^{-8}	4×10^{-10}
14.231	1×10^{9}	5×10^{-9}	2×10^{-10}
14.232	5×10^{8}	1×10^{-8}	4×10^{-10}
14.244	1×10^{9}	5×10^{-9}	2×10^{-10}
14.245	1×10^{9}	5×10^{-9}	2×10^{-10}
14.246	1×10^{9}	5×10^{-9}	2×10^{-10}
14.247	1×10^{9}	5×10^{-9}	2×10^{-10}
14.248	1×10^{9}	5×10^{-9}	2×10^{-10}

* Calibration resistor has same value
** Amplifier gain x 25

The gas gain mode of operation was employed for the 1450Å photometer in later flights to increase the sensitivity. The result of a typical laboratory measurement of the gain versus voltage is shown in Figure B-11. It was found that 650 volts could be safely applied to the detectors before the degrading effects of breakdown (corona) occurred. The modifications are shown in Figure B-12. Encapsulation of the high voltage connections prevents voltage breakdown external to the photometer during ascent and descent. The output of the high voltage power supply is fed to the ion chamber through a low pass filter. This minimizes the effect of breakdown within the ion chamber and prevents complete loss of data. If the output of the power supply should exceed the voltage

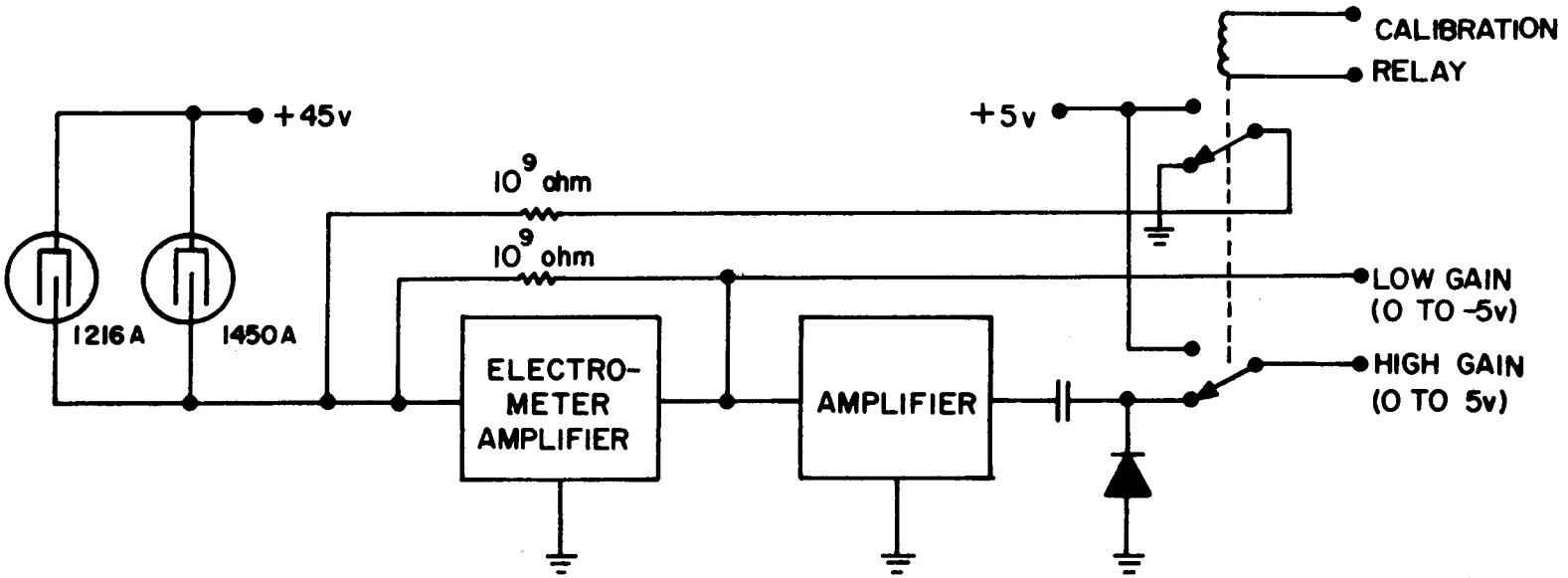

Figure B-10. Schematic of circuit of uv experiment.

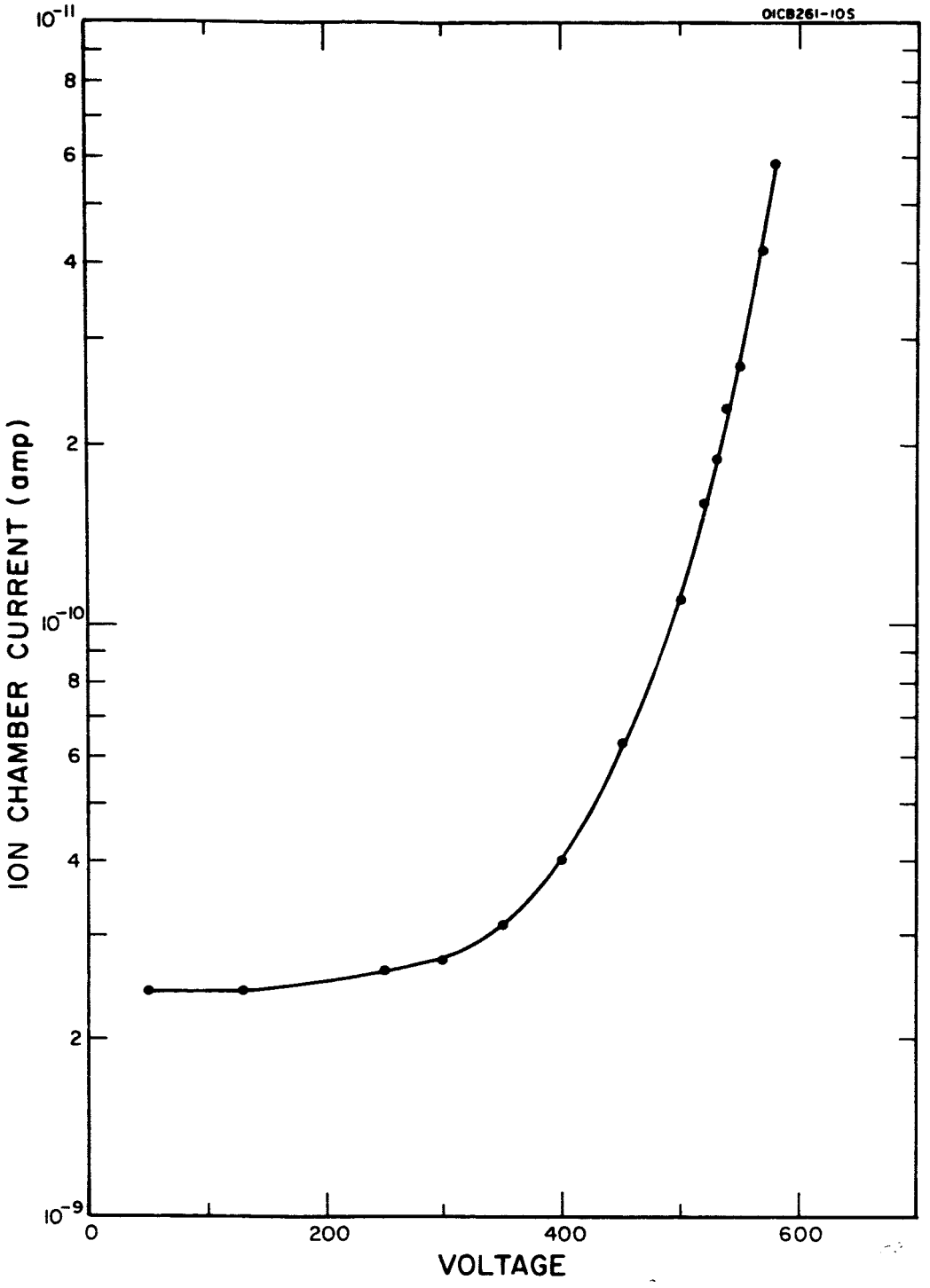

Figure B-11 Typical gas gain characteristics for 1450Å photometer.

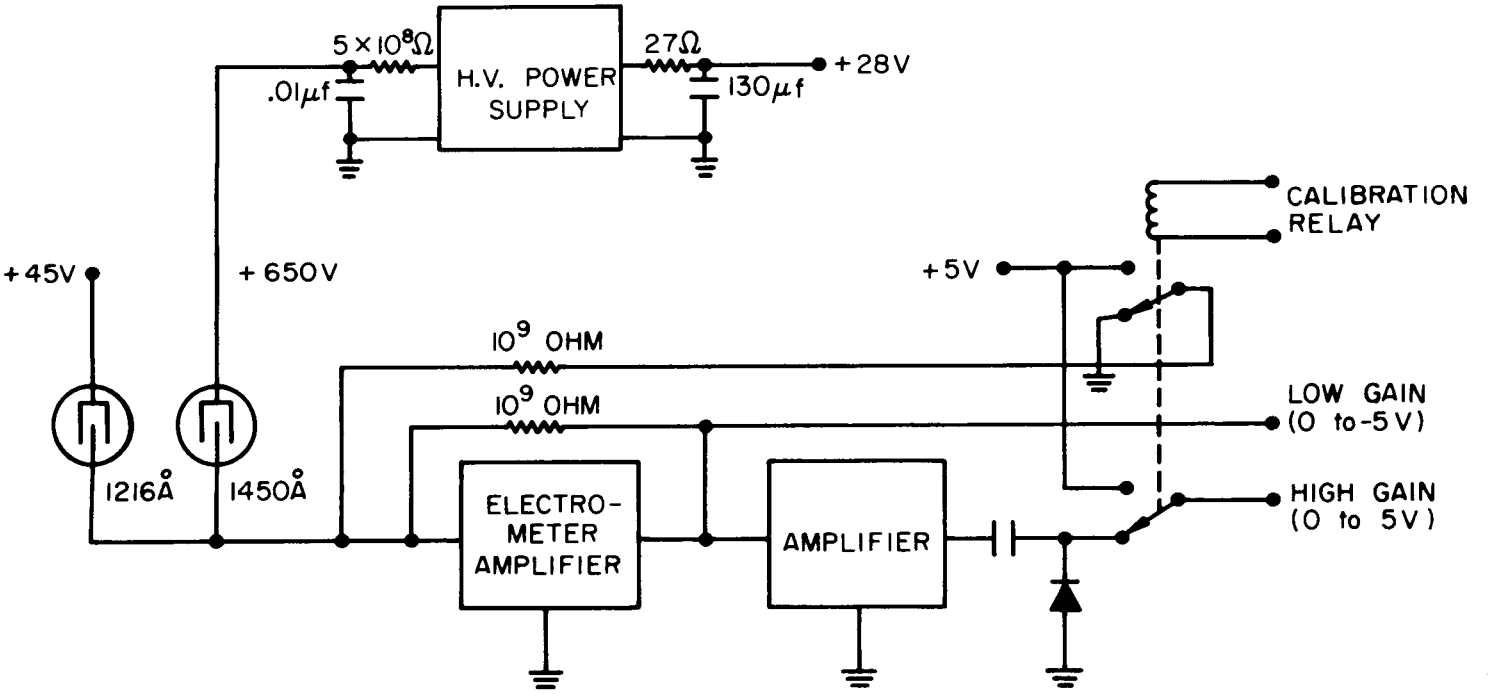

01CB265-10F

Figure B-12. Schematic of uv experiment with gas gain.

required to cause breakdown for the fixed geometry and pressure conditions internal to the ion chamber, the capacitor discharges to ground through the low impedance path of the breakdown. The breakdown will cease with reduced voltage. The long time constant of the filter (5 seconds) reduces the breakdown repetition rate, and thereby increases the time for data acquisition. The ripple voltage, which is capacitively coupled from the output to the input of the power supply, is filtered from the main +28 volt line. Figure B-13 shows the first Type A payload, Nike Apache 14.244, to carry gas-gain instrumentation. The high voltage power supply (not yet encapsulated) is mounted on the uv deck as indicated. Results of the inclusion of the gas gain technique are discussed in another section of the report.

Boom Mounted Probes

The RF probe and the spherical ion trap are shown mounted on the extended booms in Figure B-14.

It had been determined from the data of the previous Type B payload flight (Nike Apache 14.149) that the exposed surface area of the RF probe electrode was too great. When the probe scanned toward the positive end of the sweep, the return area on the rocket was insufficient to offset the electron current collected by the probe. For positive sweep voltages, this effect would drive the rocket "ground" negatively such that the probe would barely reach plasma potential. Coating the lower half of the fork rods and the fork box with a high temperature synthetic resin reduced the exposed area of the probe and eliminated the effect of driving the rocket ground negatively. In addition, the maximum positive potential which the sweep reaches was increased from 5 volts to 7 volts. The number of outputs was reduced from four to three and the lowest sensitivity channel was omitted.

The Spherical Ion Trap is the same as that in Nike Apache 14.149. It time shares a common electrometer with the DC probe. Figure B-15 shows the voltage program and telemetry sequence of the DC probe, the RF probe, and the Spherical Ion Trap. Since this program synchronizes the probes a maximum amount of data can be obtained and interference from variation of vehicle potential is eliminated.

Baroswitches

Two baroswitches (CHI Model 6617, Modified, 50,000 ft and 75,000 ft) installed on the control deck serve four purposes: (1) to provide altitude reference for trajectory determination in the absence of radar data, (2) to relatch the power transfer relay should it unlatch during the launch phase, (3) to arm the electronic timer in the door release circuit, and (4) to control the instrumentation calibration cycles. The door release and calibration circuits are shown in Figure B-16. An electronic time-delay circuit is initiated by a baroswitch at 75,000 ft. A second baroswitch set for 50,000 ft arms the

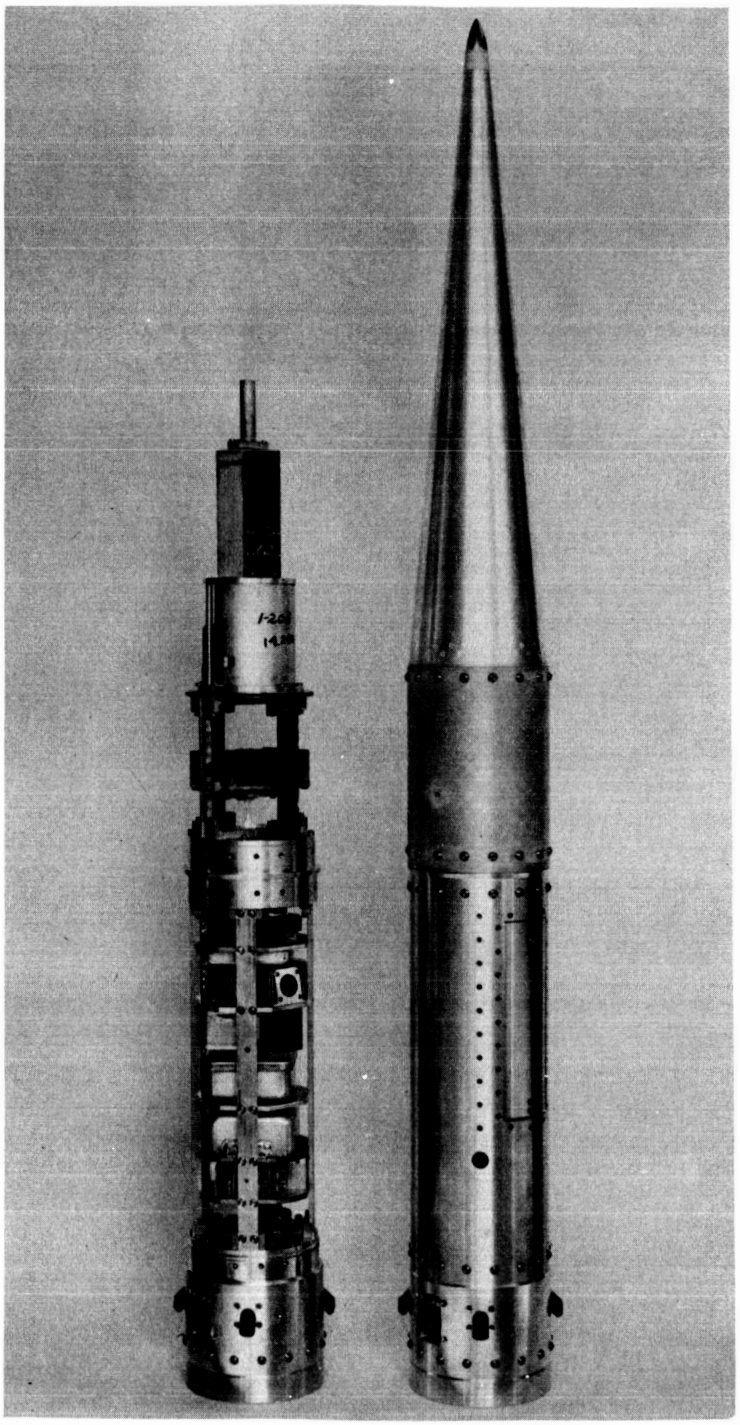

Figure B-13. Type A payload with gas gain instrumentation.

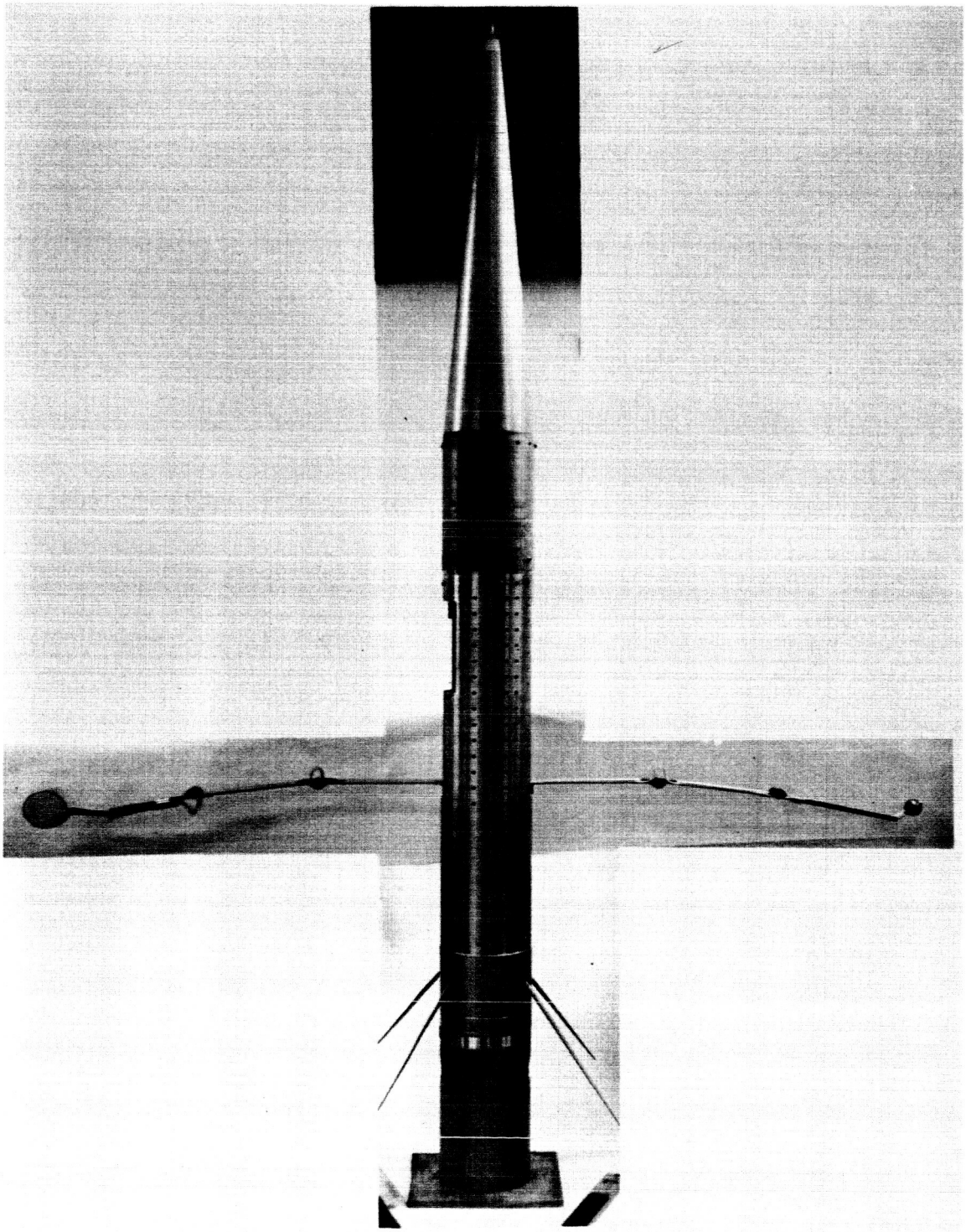

Figure B-14. Type B payload, booms extended.

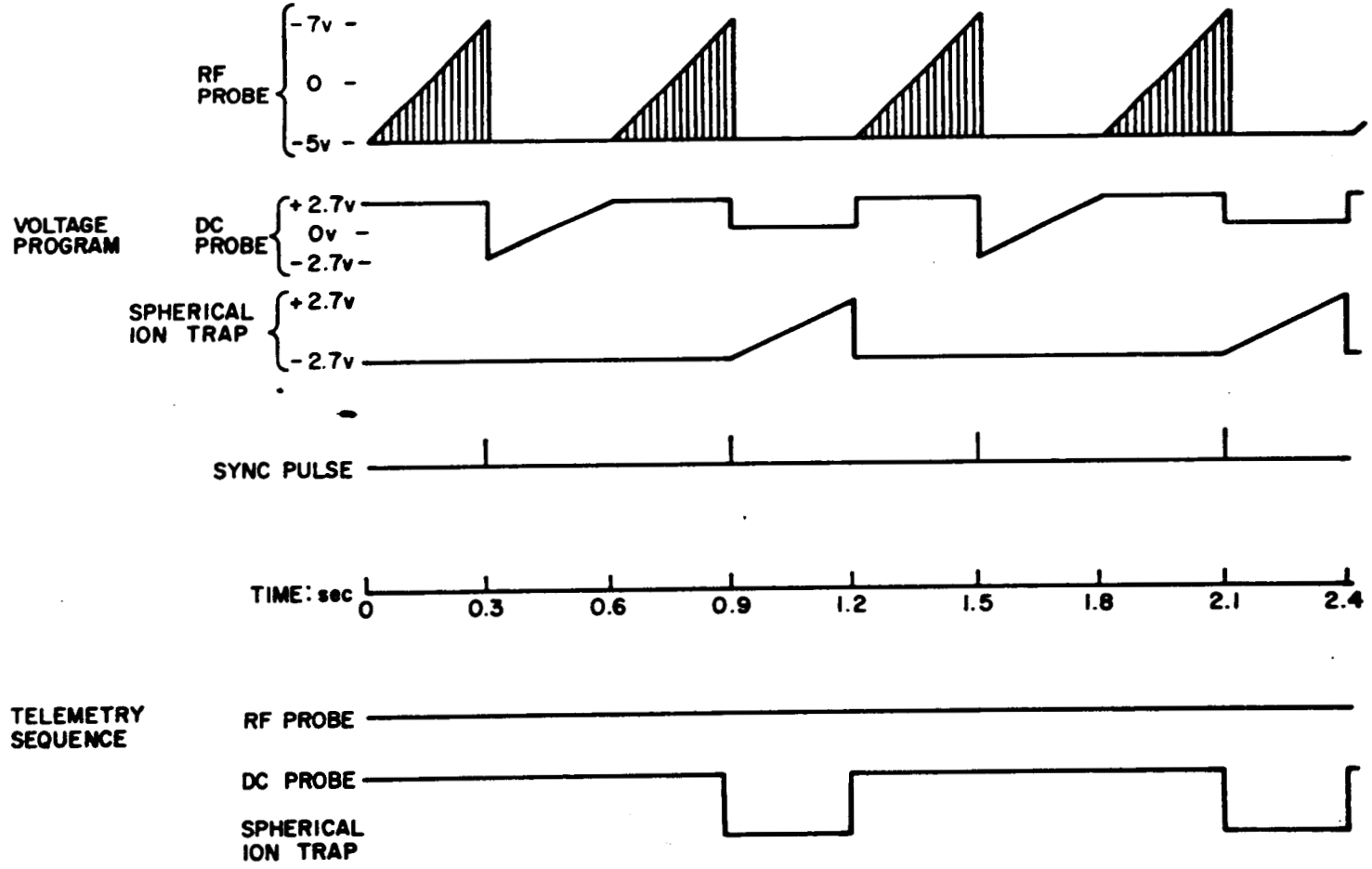

Figure B-15. Probe voltage and telemetry sequence for Nike Apache 14.229 (Type B Payload).

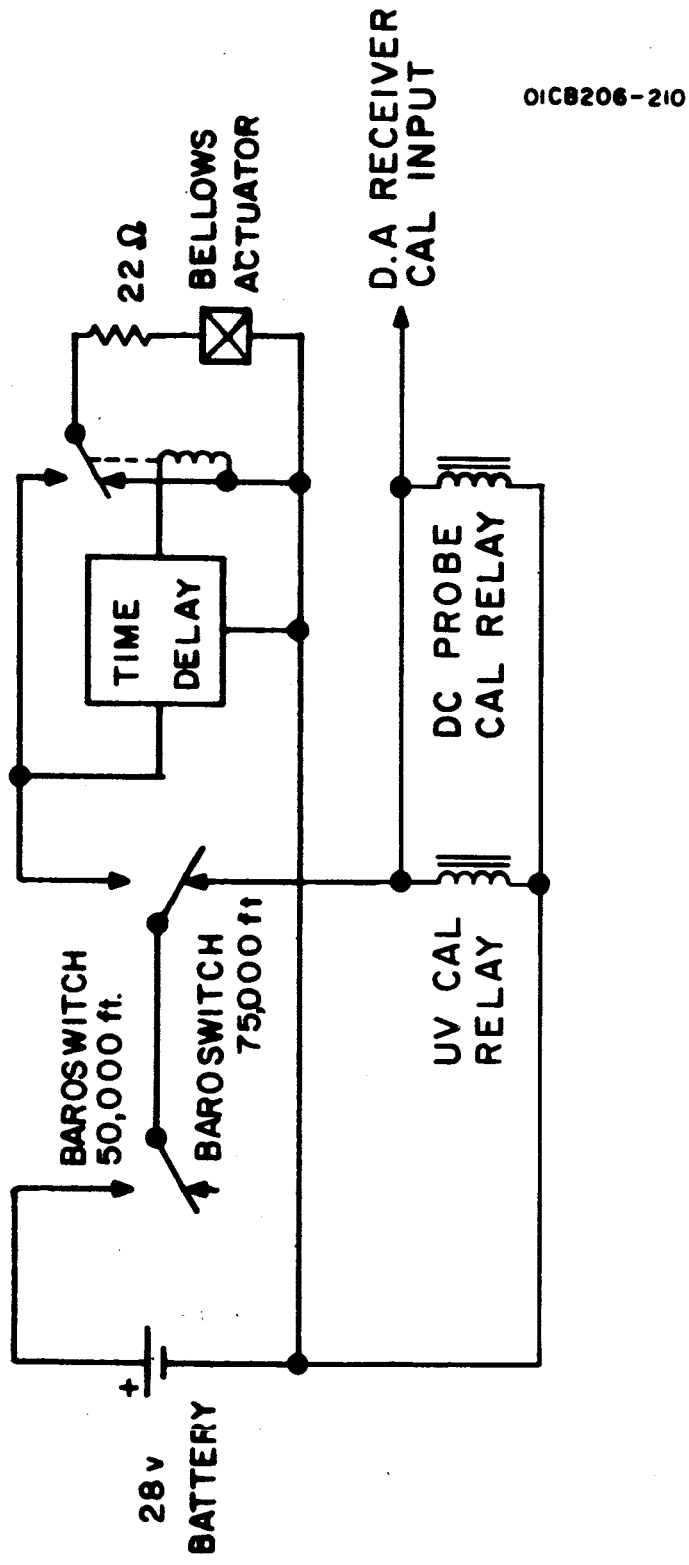

Figure B-16. Door release and calibration circuits.

circuit. During the interval between the two switchings the instrumentation is calibrated. On ascent, the calibration period is about 5 seconds beginning at T + 25 seconds; on descent, it is about 5 seconds starting about 22 seconds before impact.

Telemetry System

The telemetry system consists of a 250 milliwatt solid-state transmitter (Vector Model TRPT-250), a mixer amplifier (Vector Model TA-48), sub-carrier oscillators (Vector Model TS-41), and a four-element turnstile antenna. Table B-4 lists the channel assignments for Type A and B payloads.

TABLE B-4

TELEMETRY CHANNEL ASSIGNMENTS

IRIG Channel	Center Frequency, KHz	Percentage Deviation	Information Bandwidth	Signal	
				Type A Payload	Type B Payload
9	3.9	±7.5	60	Magnetic Aspect Sensor	Magnetic Aspect Sensor and Monitor Voltages
10	5.4	±7.5	81	AGC, Propagation Receiver	Same as A
11	7.35	±7.5	110	UV Detectors (180° opposed) Low Gain	RF Probe Output 3
12	10.5	±7.5	160	UV Detectors (180° opposed) High Gain	RF Probe Output 2
A	22.0	±15	660	DC Probe	RF Probe, Output 1
C	40.0	±15	1200	Solar Aspect Sensor	DC Probe
E	70.0	±15	2100	Output, Propagation Receiver	Same as A

Electronic Timer

The mechanical timer has been replaced by an electronic time delay circuit shown in Figure B-17. When voltage is applied at 75,000 ft, altitude the silicon controlled rectifier acts as a high impedance when its gate is near ground

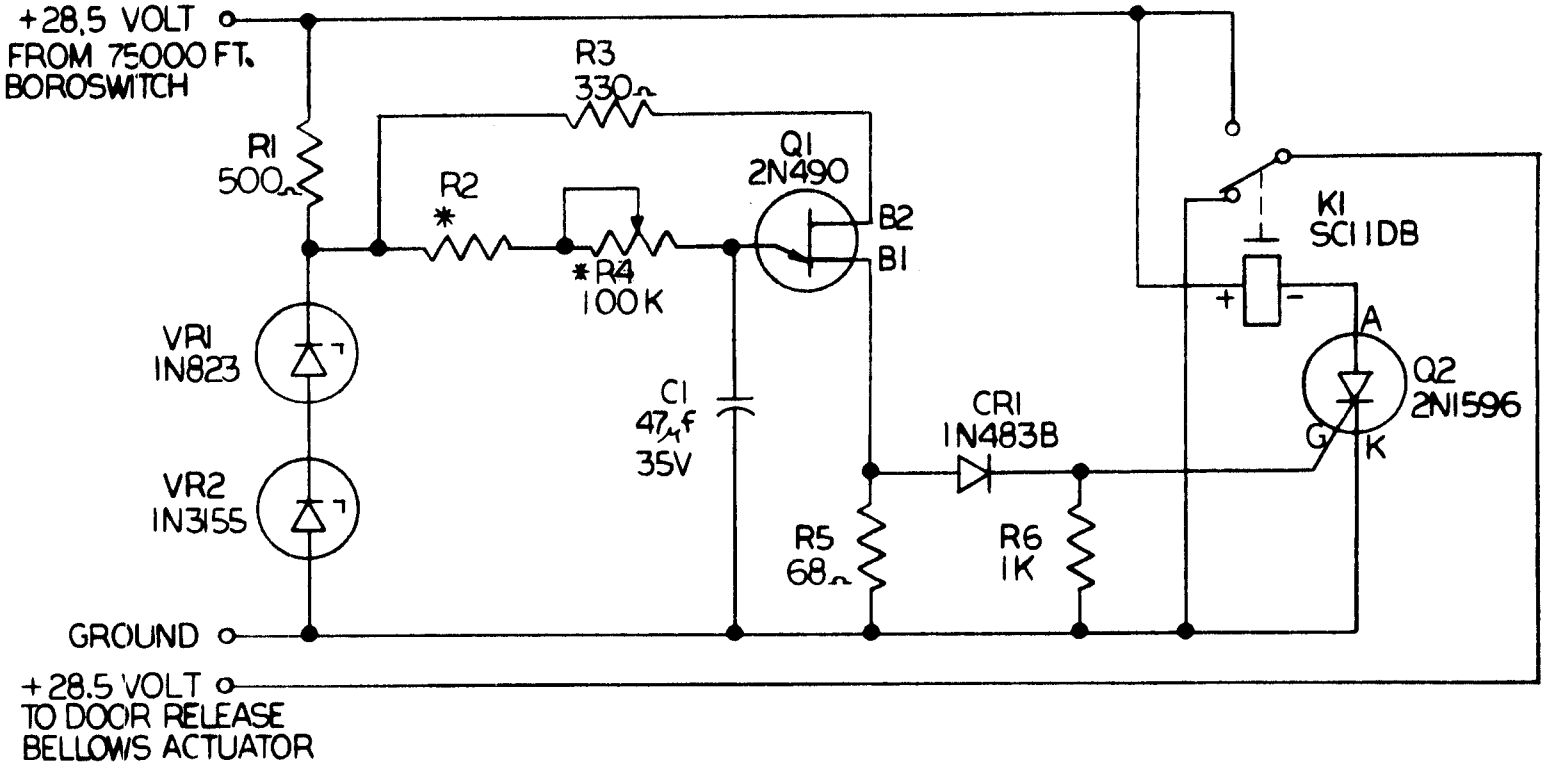

* RESISTORS R2 & R4 SELECTED FOR 12 SECOND DELAY (TYPE A) OR 22 SECOND DELAY (TYPE B).

Figure B-17. Electronic timer.

potential. The applied voltage when dropped across the anode-to-cathode of the SCR prevents closure of the relay. The unijunction transistor (2N490) is connected as a typical relaxation oscillator configuration to produce a pulse at the gate of the SCR. The time constant is approximately RC. For a fixed value (47 μf) of C, R is selected to provide a 12-sec time delay for the Type A payload and a 22-second time delay for the Type B payload. When the SCR is triggered, the relay will be turned on to apply power to the door release circuit. The property of the SCR that renders it useful for this application is that once triggered, it will continue to conduct until power is removed by the 75,000 ft baroswitch on descent.

Power Supply

The main power supply voltage is +28.5 volts. The battery pack consisting of 19 rechargeable cells (Yardney HR-05) is capable of delivering 200 mA for 60 minutes. The Type A payload requires approximately 500 mA and the Type B, 610 mA. Flight time is about 7 minutes; hence, a sufficient margin of safety is provided for pre-flight checkout.

Separate bias supplies (Mallory mercury batteries) are included for low current applications.

APPENDIX B

REFERENCES

B-1. Smith, L.G., Weeks, L. H., and McKinnon, P. J.: "Investigation of the D and E Regions of the Ionosphere During the International Quiet Sun Year," GCA Corporation, Technical Report No. 65-21-N (1965), NASA CR-391 (1966).

B-2. Smith, L. G., and Weeks, L. H.: "Molecular Oxygen Densities from Rocket Measurements of Lyman-α Absorption Profiles," GCA Corporation, Technical Report No. 65-10-N (1965), NASA CR-392 (1966).

B-3. Knoebel, H., Skaperdas, D., Gooch, G., Kirkwood, B., and Krone, H.: "High Resolution Radio Frequency Measurements of Faraday Rotation and Differential Absorption with Rocket Probes," Ed. D. Skaperdas, Report R-273, NASA Frant NsG504 (December 1965).

APPENDIX C

COMPUTER PROGRAM IN FORTRAN LANGUAGE

A computer program in FORTRAN language is presented for the calculation of the zenith and azimuth angles of the sun from a rocket and the minimum ray height. This program is useful for making these calculations for any object of known ephemerides from any position on or near the earth.

The correspondence between the labels on Figure 19 and the FORTRAN symbols can be determined from the following chart:

Figure	FORTRAN Symbol
χ	ZEN
R	R
z	ALT
h	HGHT
s	DIST
R′	RP

The input is entered in card form in the order shown below:

Number of Cards	Parameters
1	N1, N2, N3
N2	output heading cards
1	SIDM, PAR
1	RA, DRA1, DRA0
1	DE, DDE1, DDE0
N1	GMT, FLAT, FLONG, ALT

See the glossary at the end of this appendix for the meanings of the parameters and the program listing for the format of the cards. The units of the parameters are: hours - SIDM, RA, GMT, FLONG; degrees - DE, FLAT; seconds - PAR, DRA1, DRA0, DDE1, DDE0, kilometers - ALT.

Most of the time it will be desirable to have the computer calculate the exact values of right ascension and declination. This is done in statements 15 + 1 and 15 + 2. These equations represent Stirling's interpolation formula to second order [where TT = u, DRA1 = Δy_{-1}, DRA0 = Δy_0, RA = y_0, etc.] with appropriate conversion factors.* The terms DRA1, DRA0, DDE1, and DDE0 are to be omitted if the exact values of the right ascension and declination are to be entered.

With the input to the zenith and azimuth equations available, the hour angle is calculated. The angles are converted to radians for computer use. An adjustment for parallax is available if desired.

---

*Notation taken from Numerical Mathematical Analysis, by J. B. Scarborough, Fourth Edition, the John Hopkins Press, Baltimore, Maryland, p.74, 1958.

The zenith and azimuth angles are now computed using standard formulas. These formulas involve no approximations and therefore are good to seven digits, corresponding to at least 0.036 seconds of arc. Therefore the accuracy of the zenith and azimuth angles is essentially limited only by the accuracy of the input data.

If the zenith angle is greater than 90°, the shadow height is calculated. The radius of the earth needed for this calculation is obtained by using Hayford's spheroid as a model of the earth. The quantities HGHT and DIST are not meaningful unless the observer is above the surface of the earth, so if the zenith angle is greater than 90° and ALT $\neq$ 0, these quantities are calculated. Because the subrocket latitude will differ from that at HGHT, the earth radius is calculated at both positions which results in a small adjustment to the shadow height and HGHT. The latitude and longitude at HGHT, LT and LNG, are calculated assuming a spherical earth whose radius is that at the subrocket position.

The output is in the form of punched cards in the order shown below:

(Heading Cards)

SIDL, RA , DE , PAR
GMT , LAT , LONG, ALT
ZEN , AZIM, SHDW
HGHT, DIST, LT , LNG

A brief glossary is followed by a listing of the program.

GLOSSARY

N1	number of observer input coordinates per set of ephemeris input, $1 \leq N1 \leq 99$
N2	number of output heading cards, $0 \leq N2 \leq 99$
N3	if not zero, types out ZEN, AZIM
RE	earth radius at the equator
F2	$(1 - 1/f)^2$, where f is the flattening constant
SIDM	sidereal time at zero hours GMT
PAR	horizontal parallax
RA	right ascension at zero hours GMT
DRA1	upper difference of right ascension
DRA0	lower difference of right ascension
DE	declination at zero hours GMT
DDE1	upper difference of declination
DDE0	lower difference of declination
GMT	Greenwich mean time
FLAT	latitude of rocket
FLONG	longitude of rocket
ALT	altitude of rocket
ALPHA	right ascension at specified GMT
DELTA	declination at specified GMT
SIDG	sidereal time of the Greenwich meridian
SIDL	local sidereal time
HA	hour angle
CZ	cosine of zenith angle

SZ	sine of zenith angle
CA	cosine of azimuth angle
SA	sine of azimuth angle
ZEN	solar zenith angle
AZIM	solar azimuth angle
R	earth radius at the subrocket position
RP	earth radius at HGHT
SHDW	shadow height = z-h csc χ
HGHT	h(see Figure 19)
DIST	s(see Figure 19)
FLT	latitude at HGHT
FLNG	longitude at HGHT

```
C       ZENITH AND AZIMUTH COMPUTATIONS
C       PROGRAMMED BY RV SILLARS
        PI=3.1415927
        SX=60.0
        RE=6378.388
        F2=(296.0/297.0)**2
    1   READ 91,N1,N2,N3
        PUNCH 93
        PUNCH 94
        PUNCH 95
        PUNCH 96
        DO 24 I=1,3
   24   PUNCH 90
        IF(N2)10,5,10
   10   DO3K=1,N2
        READ99
    3   PUNCH99
    5   PUNCH 90
        READ 92,X,Y,Z,PAR
        SIDM=X+Y/SX+Z/(SX**2)
        READ 92,X,Y,Z,DRA1,DRA0
        RA=X+Y/SX+Z/(SX**2)
        READ 92,X,Y,Z,DDE1,DDE0
        DE=X+Y/SX+Z/(SX**2)
        DO2I=1,N1
        READ 92,GMT,FLAT,FLONG,ALT
        IF(DRA0)15,13,15
   13   ALPHA=RA
        DELTA=DE
        SIDG=SIDM
        GOTO16
   15   TT=GMT/24.0
        ALPHA=RA+(DRA0+DRA1+(DRA0-DRA1)*TT)*TT/7200.0
        DELTA=DE+(DDE0+DDE1+(DDE0-DDE1)*TT)*TT/7200.0
        SIDG=SIDM+GMT*0.0027379
   16   SIDL=SIDG-FLONG+GMT
        HR=SIDL-ALPHA
        HA=HR*0.26179939
        SHA=SIN(HA)
        CHA=COS(HA)
        PHI=FLAT*0.017453293
        SPHI=SIN(PHI)
        CPHI=COS(PHI)
        DEL=DELTA*0.017453293
        SDEL=SIN(DEL)
        CDEL=COS(DEL)
        PARR=4.8481368E-06*PAR
        SPARR=SIN(PARR)
        C=SQRT(1.0/(CPHI**2+F2*(SPHI**2)))
        S=F2*C
        PSPHI=(S+0.15677940E-03*ALT)*SPHI
        PCPHI=(C+0.15677940E-03*ALT)*CPHI
        AA=CDEL*SHA
        BB=CDEL*CHA-PCPHI*SPARR
        CC=SDEL-PSPHI*SPARR
        AB=SQRT(AA*AA+BB*BB)
        ABC=SQRT(AA*AA+BB*BB+CC*CC)
        SHA=AA/AB
        CHA=BB/AB
        SDEL=CC/ABC
```

```
      CPHI=AR/ABC
      CZ=CPHI*SPHI+CPHI*CDEL*CHA
      SZ=SQRT(1.0-CZ*CZ)
      CA=(SDEL*CPHI-CDEL*SPHI*CHA)/SZ
      SA=-CDEL*SHA/SZ
      ZENR=ATAN(SZ/CZ)
      AZMR=ATAN(SA/CA)
      IF(CA)31,32,32
   32 IF(SA)33,34,34
   31 AZMR=AZMR+PI
      GOTO34
   33 AZMR=AZMR+2.0*PI
      GOTO34
   34 AZIM=AZMR*57.29578
      IF(CZ)37,38,38
   37 ZENR=PI+ZENR
   38 ZEN=ZENR*57.295780
      IF(N3) 17,16,17
   17 PRINT 98,ZEN,AZIM
   18 PUNCH 97,SIDS,ALPHA,DELTA,PAR
      PUNCH 97,GMT,FLAT,FLONG,ALT
      IF(CZ)11,19,19
   19 PUNCH 97,ZEN,AZIM
      GO TO 2
   11 R=RE*SQRT((CPHI**2+(F2*SPHI)**2)/(CPHI**2+F2*SPHI**2))
      SPP=SPHI*SZ-CPHI*CZ*CA
      CPP2=(1.0-SPP**2)
      RP=RE*SQRT((CPP2+(F2*SPP)**2)/(CPP2+F2*SPP**2))
      SHDW=RP/SZ-R
      PUNCH 97,ZEN,AZIM,SHDW
      IF(ALT) 6,2,6
    6 HGHT=(ALT-SHDW)*SZ
      DIST=-(R+ALT)*CZ
      PPR=ATAN(SPP/SQRT(CPP2))
      FLT=PPR*57.295780
      SDLR=SA*SQRT(CZ*CZ/CPP2)
      DLR=ATAN(SDLR/SQRT(1.0-SDLR**2))
      FLNG=FLONG-DLR*3.819718
      PUNCH 97,HGHT,DIST,FLT,FLNG
    2 PUNCH90
      PUNCH91
      GOTO1
   90 FORMAT(1H )
   91 FORMAT(5I2)
   92 FORMAT(5F10.0)
   93 FORMAT(6X10HSIDL (HRS),5X10HRA   (HRS),5X10HDEL   (DEG),5X9HPAR (SEC))
   94 FORMAT(6X10HGMT  (HRS),5X10HLAT  (DEG),5X10HLONG (HRS),5X8HALT (KM))
   95 FORMAT(6X10HZEN  (DEG),5X10HAZIM (DEG),5X9HSHDW (KM))
   96 FORMAT(6X9HHGHT (KM),6X9HDIST (KM),6X10HLT   (DEG),5X9HLNG (HRS))
   97 FORMAT(4F15.6)
   98 FORMAT(2F10.5)
   99 FORMAT(40H
     140H
      END
```